

Identify Metamorphic and Primary Multiple Sulfur Isotopic Signatures in the 2.7 Ga Pyrite Nodules from the Southwestern Superior Province (Minnesota, USA)

by

Jianghanyang Li

A thesis submitted in partial fulfillment of the requirements for the degree of

Master of Science

Department of Earth and Atmospheric Sciences
University of Alberta

© Jianghanyang Li, 2016

Abstract

Sulfur isotopes of some Archean rocks show unique mass independent fractionation (S-MIF) signatures, which are generally considered to have been produced by UV radiolysis on volcanic SO₂ in the oxygen-free Archean atmosphere. Based on the distinct S-MIF signals of different sulfur sources (i.e., atmospheric and non-atmospheric) in the Archean ocean and ³⁴S fractionation associated with biological processes, the multiple sulfur isotope system has been widely used to infer the energy sources of biological activities and the pathways of sulfur cycling from the atmosphere to the ocean, and further to sediments in the Archean. The premise of such applications is that the sulfur isotopic compositions of sulfur-bearing minerals in the samples are not affected by post-depositional processes. However, all the Archean rocks discovered to date have experienced at least greenschist-facies metamorphism. Although most previous studies employing multiple sulfur isotopes to infer Archean atmospheric, oceanic or lacustrine conditions have cautiously targeted the least metamorphosed samples (e.g., lower greenschist- to greenschist-facies), quantitative assessment of metamorphism and fluid alteration on the sulfur isotopic compositions of minerals (e.g., pyrite) is lacking.

In this study, we employed a Secondary Ion Mass spectrometry (SIMS) and an electron microprobe analyzer (EPMA) instruments to carry out *in-situ* multiple sulfur isotope and element analysis (Fe, S, Ni and Cu) on three types of pyrite grains in the 2.7 Ga shale samples from the Deer Lake Greenstone Belt, Superior Province: (1) large diagenetic pyrite nodules, (2) metamorphic fluid related subhedral pyrite grains disseminated in quartz veins surrounding the pyrite nodules; and (3) a thin lamina of

pyrite parallel to quartz veins. The purpose of this thesis work is to (1) quantitatively assess the metamorphic effect on sulfur isotopic compositions of pyrite, and (2) infer the photochemical and biological processes involved in the sulfur cycle in 2.7 Ga from the unaltered pyrite. Our new data are expected to contribute to a better understanding of the microbial activities related to sulfur cycling in the 2.7 Ga ocean.

Our results show that the subhedral pyrite grains contain lower Cu, more variable Ni concentrations and higher $\delta^{34}\text{S}$ ($>3.2\text{‰}$) and $\Delta^{33}\text{S}$ ($>4.1\text{‰}$) values than the adjacent pyrite nodules. Measurements on the pyrite grains in the lamina yield two groups of data. One group shows high Cu concentrations, low Ni concentrations, low $\delta^{34}\text{S}$ (-2.7‰ to -1.1‰) and $\Delta^{33}\text{S}$ (2.5‰ to 2.9‰) values, all of which are identical to those of the pyrite nodule rims; the other group displays undetectable Cu concentrations, high Ni concentrations, and high $\delta^{34}\text{S}$ ($>2.5\text{‰}$) and $\Delta^{33}\text{S}$ ($>3.6\text{‰}$) values, close to those of the subhedral pyrite grains, implying (metamorphic) hydrothermal origin, which was characterized by little Cu but very high Ni concentrations and high $\delta^{34}\text{S}$ (15.2‰) and $\Delta^{33}\text{S}$ (5.9‰) values.

Three diagenetic pyrite nodules examined in this study show trace element and sulfur isotope compositions similar to each other, suggesting a common growth history. All nodules show cross-grain variations in both $\delta^{34}\text{S}$ (-2.9‰ to $+2.0\text{‰}$) and $\Delta^{33}\text{S}$ ($+0.3\text{‰}$ to $+2.5\text{‰}$) values, with decrease in $\delta^{34}\text{S}$ and increase in $\Delta^{33}\text{S}$ from cores to rims. This correlation, together with the obvious isotopic and elemental difference between the subhedral pyrite grains and nearby nodule rim, suggests that the isotopic compositions of pyrite nodules were not shifted by metamorphic fluid.

The negative correlation between $\delta^{34}\text{S}$ and $\Delta^{33}\text{S}$ values observed in the three

diagenetic pyrite nodules can be explained by a mixing between two sulfur sources: one is sulfate with positive $\delta^{34}\text{S}$ and negative $\Delta^{33}\text{S}$ values; the other has negative $\delta^{34}\text{S}$ and positive $\Delta^{33}\text{S}$ values, pointing to elemental sulfur. The negative correlation between $\delta^{34}\text{S}$ and $\Delta^{33}\text{S}$ observed in this study is close to the “felsic volcanic array” and the 193 nm photolytic array except our data sit slightly above these arrays and show a gentler slope. This distribution pattern can be best explained by a mixing between elemental sulfur on these arrays with sulfate shifted from these arrays to slightly higher $\delta^{34}\text{S}$ values by low-extent removal of the sulfate via bacterial sulfate reduction. Our results support the hypothesis that the photochemical reactions during intensive volcanic periods could be different and result in a specific distribution pattern as the “felsic volcanic array” or the 193 nm experimental photolytic array.

Preface

Samples in this study were provided by Drs. Holly Stern and Gang Yang at Colorado State University. I was responsible for sample selection, preparation and data collection for this study. Sample preparation includes petrography observation, polishing, EPMA analysis and SIMS analysis.

In-situ multiple sulfur isotope analysis was carried out (with help from Dr. Richard Stern, Dr. Long Li and Siwen Wei) in the Canadian Center for Isotopic Microanalysis at the University of Alberta.

In-situ elemental analysis was carried out in the Electron Microprobe Laboratory at University of Alberta, with the help from Dr. Andrew Locock.

Acknowledgement

Firstly, I would like to express my deepest appreciation to my supervisor, Dr. Long Li, for giving me the precious opportunity to undertake this study, for his valuable guidance during this study, for his inculcation throughout the last two years, for his preparation of this research project and beyond.

Secondly, I would like to thank the following people, for their crucial contributions to my research in the form of explaining analytical techniques, completing lab work and giving advice on my thesis: from University of Alberta, Dr. Richard Stern (Managing Director, Canadian Centre for Isotopic Microanalysis), Dr. Andrew Locock (Electron Probe Micro Analyzer Lab Manager), Dr. Karlis Muehlenbachs, Olga Lenver (technician, Stable Isotope Laboratory) and Dr. Jingao Liu; from University of Science and Technology of China, Dr. Fang Huang, Jinting Kang (Research Assistant), Yuhan Qi (Research Assistant) and Jingya Hu (Research Assistant).

Thirdly, I would like to thank Dr. Robert A. Creaser at the University of Alberta and Gang Yang at the Colorado State University for their generosity in providing the priceless samples.

Fourthly, I would like to thank my examining committee: Dr. Tom Chacko, Dr. Kurt Konhauser, Dr. Long Li and Dr. Sarah Gleeson for their constructive reviews, which greatly improved quality of my thesis.

Additionally, I would like to thank Dr. Graham Pearson, Dr. Robert A. Creaser, Dr. Karlis Muehlenbachs, Dr. Long Li, Dr. Daniel Alessi, for their inspiring instruction in the courses I have taken.

Last but not least, I would like to thank my family: my parents, my grandmother and my late grandfather, for their patience and support throughout the years I have dedicated to this research.

This research is generously funded by: Natural Sciences and Engineering Research Council-Discovery Grant to Long Li.

Table of content

Abstract	ii
Preface	v
Acknowledgement	vi
1. Introduction	1
1.1 Sulfur isotope mass independent fractionation in the Archean.....	1
1.2 Pyrite formation.....	6
1.3. Metamorphic effect on sulfur isotopic compositions of pyrite.....	9
1.4. High-resolution in-situ analysis on single pyrite grains to uncover primary signals.....	10
2. Geological setting	13
3. Sample description	18
3.1 Hand-specimen observation.....	18
3.2 SEM observation.....	21
4. Method	29
4.1. Element concentration analysis using EPMA.....	29
4.2. Multiple sulfur isotope analysis using SIMS.....	30
5. Results	31
5.1. Element concentrations in pyrite.....	31
5.1.1. Pyrite nodules.....	31
5.1.2. Subhedral pyrite grains along nodule margins.....	32
5.1.3. Lamina pyrite.....	33
5.2. Multiple sulfur isotopic compositions of pyrite.....	39
5.2.1. Pyrite nodules.....	39
5.2.2. Subhedral pyrite grains in quartz veins.....	39
5.2.3. Lamina pyrite.....	40
6. Discussion	49
6.1. Pyrite morphology, trace elements and zonation patterns of pyrite nodules.....	49
6.2. Elemental and sulfur isotopic signatures of metamorphic fluids and metamorphic effects on pyrite nodules.....	51
6.3. The 2.7Ga sulfur cycle recorded in pyrite nodules.....	56
7. Conclusion	62
Bibliography	63
Appendices	72

List of Tables

Table 1 In-situ multiple sulfur data of pyrite from shale in Deer Lake Greenstone belt, Minnesota, USA.....	72
Table 2 In-situ element concentrations data of pyrite from shale in Deer Lake Greenstone belt, Minnesota, USA	89

List of Figures

Figure 1. Variation of $\Delta^{33}\text{S}$ values of pyrite along time.	2
Figure 2. Sketch of sulfur isotopic fractionation and potential endmembers for Archean sedimentary sulfide.	5
Figure 3. Geological map of southern Superior Province.....	13
Figure 4. Geological map of Joy Lake Sequence	15
Figure 5. Geological maps of drill core location	17
Figure 6. Photo of black shale sample ORG-44.	20
Figure 7. Photo of black shale sample ORG-45	21
Figure 8. BSE image of Nodule 1.....	24
Figure 9. BSE image of lamina pyrite and its location on ORG-45.	25
Figure 10. BSE image of Nodule 2.....	26
Figure 11. BSE image of Nodule 3.....	27
Figure 12. BSE image showing subhedral grains	28
Figure 13. Cross-section variations of total element concentrations and trace element concentrations	34
Figure 14. Trace element concentrations of subhedral pyrite grains and adjacent comparison points.....	35
Figure 15. Cu and Ni diagram of subhedral pyrite grains and comparison spots.....	36
Figure 16. <i>In-situ</i> Cu and Ni concentrations of lamina pyrite.	37
Figure 17. Cu and Ni diagram of the two groups of pyrite in the lamina.....	38
Figure 18. Cross-section Sulfur isotopic data for Nodule 1.....	41
Figure 19. Cross-section Sulfur isotopic data for Nodule 2.....	42
Figure 20. Cross-section Sulfur isotopic data for Nodule 3.....	43
Figure 21. $\Delta^{33}\text{S}-\delta^{34}\text{S}$ of three pyrite nodules	44
Figure 22. Sulfur isotopic data of subhedral pyrite grains and comparison spots	45
Figure 23. $\Delta^{33}\text{S}-\delta^{34}\text{S}$ diagram of subhedral pyrite grains and comparison spots.....	46
Figure 24. <i>In-situ</i> sulfur isotopic data of lamina pyrite.	47
Figure 25. $\Delta^{33}\text{S}-\delta^{34}\text{S}$ diagram of pyrite grains in the lamina.	48
Figure 26. Sulfur isotopic data and trace element data of subhedral pyrite, comparison spots and lamina pyrite.	53
Figure 27. Sulfur isotopic fractionation and potential endmembers for Archean sedimentary sulfide.	59

1. Introduction

1.1. Sulfur isotope mass independent fractionation in the Archean

Sulfur has four stable isotopes, ^{32}S , ^{33}S , ^{34}S and ^{36}S , which can give three isotopic ratios ($\delta^{3x}\text{S} = [({}^{3x}\text{S}/{}^{32}\text{S})_{\text{sample}}/({}^{3x}\text{S}/{}^{32}\text{S})_{\text{standard}} - 1] * 1000\text{‰}$; $x = 3, 4$ or 6 ; the standard is Vienna-Canyon Diablo Troilite or VCDT). In most geological and biological processes, stable sulfur isotopic fractionation follows the mass dependent rule:

$$\delta^{3x}\text{S} = 1000 * [(1 + \delta^{34}\text{S}/1000)^{\lambda_{3x}} - 1] \quad (1)$$

in which $x = 3$ or 6 ; $\lambda_{33} = 0.515$; $\lambda_{36} = 1.90$. However, in some sedimentary rocks older than 2.45 Ga, measured $\delta^{33}\text{S}$ and $\delta^{36}\text{S}$ values deviate from the mass dependent fractionation line defined by Equation 1. This phenomenon is referred as sulfur isotope mass independent fractionation (S-MIF; Farquhar et al., 2000; Johnston, 2011 and references therein) and the magnitudes of the deviations from mass dependent fractionation in $\delta^{33}\text{S}$ and $\delta^{36}\text{S}$ values are expressed as $\Delta^{33}\text{S}$ and $\Delta^{36}\text{S}$, which are defined as:

$$\Delta^{3x}\text{S} = \delta^{3x}\text{S} - 1000 * [(1 + \delta^{34}\text{S}/1000)^{\lambda_{3x}} - 1] \quad (2)$$

in which again $x = 3$ or 6 ; $\lambda_{33} = 0.515$; $\lambda_{36} = 1.90$. A compilation of $\Delta^{33}\text{S}$ values of pyrite samples over the last 4 billion years is shown in Figure 1. Besides the non-zero $\Delta^{33}\text{S}$ and $\Delta^{36}\text{S}$ values, Archean S-MIF signatures are also characterized by co-variation in $\Delta^{33}\text{S}$ and $\Delta^{36}\text{S}$ with the $\Delta^{36}\text{S}/\Delta^{33}\text{S}$ ratio around -1 (e.g., Farquhar et al., 2000).

The mechanism responsible for the Archean S-MIF signal is still under debate. Watanabe et al. (2009) used laboratory experiments to demonstrate that thermochemical sulfate reduction (TSR) could produce non-zero $\Delta^{33}\text{S}$ values in the sulfite products. These

authors thus proposed that TSR process could explain the Archean S-MIF record. However, ^{36}S of the sulfite product was not significantly shifted as ^{33}S was in the experiments and thus the results do not resemble the Archean S-MIF signature. The TSR results observed by Watanabe et al. (2009) were reproduced by Oduro et al. (2011) and re-interpreted as a magnetic isotope effect on ^{33}S . To date, the prevailing explanation for S-MIF observed in the Archean geological record is a photolytic effect associated with UV-induced disproportionation of volcanic SO_2 (hereafter referred as SO_2 photolysis) in anoxic atmosphere, which was first proposed by Farquhar et al. (2000). Modeling by Pavlov and Kasting (2002) further indicated that the O_2 concentration in the Archean atmosphere had to be less than 10^{-5} present atmospheric level in order to produce and preserve the S-MIF signal.

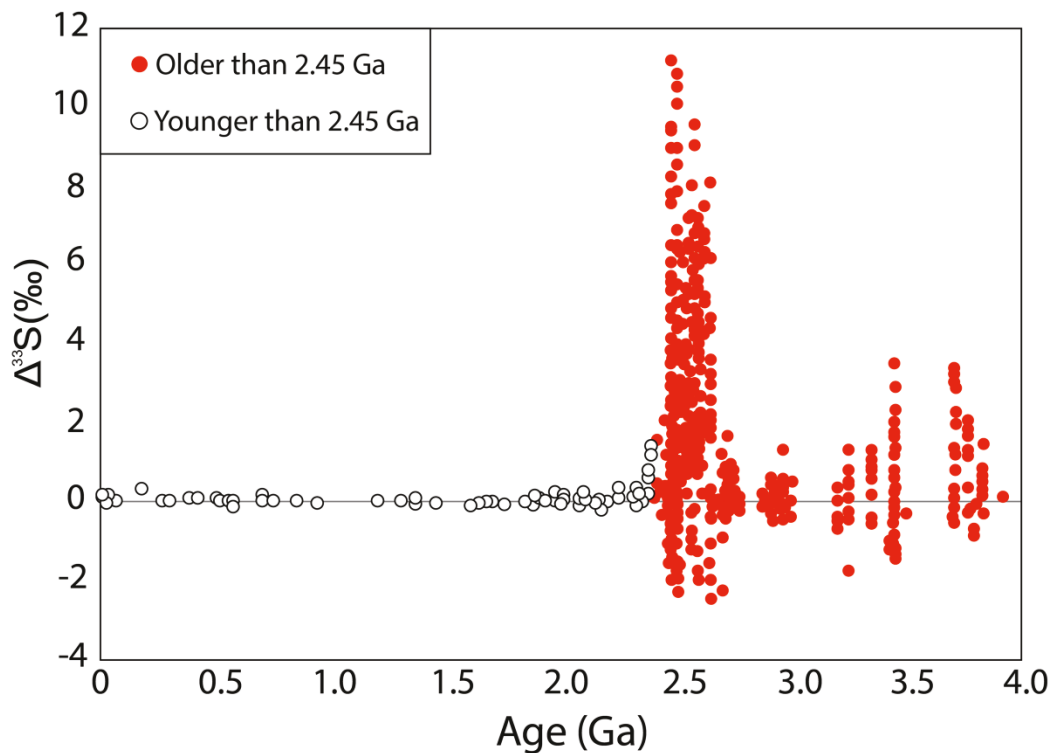


Figure 1. Variation of $\Delta^{33}\text{S}$ values of pyrite over time showing that S-MIF signal was ubiquitous in Archean but disappeared after 2.45 Ga (modified from Johnston, 2011).

The photolytic mechanism is supported by laboratory SO₂ photolysis experiments (e.g., Farquhar et al., 2001; Farquhar and Wing, 2003, 2005). The laboratory SO₂ photolysis experiments by Farquhar and colleagues commonly yielded two major products: sulfate and elemental sulfur. Particularly, the reactions using UV with wavelengths of both ~193 nm and >220 nm gave negative $\Delta^{33}\text{S}$ values for sulfate product, positive $\Delta^{33}\text{S}$ values for elemental sulfur product, and $\Delta^{36}\text{S}/\Delta^{33}\text{S}$ ratios around -1 from the linear fitting of sulfate and elemental sulfur data (Farquhar et al., 2001). These are consistent with the observations in the Archean rocks, in which sulfate in evaporates all have negative $\Delta^{33}\text{S}$ values while pyrite samples have more variable $\Delta^{33}\text{S}$ values from negative to positive values likely as a result of different ratios of mixing between sulfate and elemental sulfur sources (Farquhar et al., 2000). Following these experimental results, it is assumed that sulfate and elemental sulfur were the two major products from the photochemical reactions in the Archean atmosphere and eventually washed down into the ocean to provide two additional sulfur sources to the prevailing hydrothermal vent sulfur source for further formation of S-bearing minerals (mainly pyrite and minor gypsum in evaporites; e.g., Kamineni 1983; Farquhar et al., 2000).

However, the SO₂ photolysis experiments at 193 nm and >220 nm UV bands yielded very different $\delta^{34}\text{S}$ values for the elemental sulfur and sulfate products: the >220 nm photolysis produced positive $\delta^{34}\text{S}$ values for elemental sulfur product and negative $\delta^{34}\text{S}$ values for sulfate product, which all together gave a positive trend on the $\Delta^{33}\text{S}$ - $\delta^{34}\text{S}$ diagram with a $\Delta^{33}\text{S}/\delta^{34}\text{S}$ slope of ~0.13; whereas the 193 nm photolysis produced negative $\delta^{34}\text{S}$ values for elemental sulfur product and positive $\delta^{34}\text{S}$ values for sulfate, which all together gave a negative trend on the $\Delta^{33}\text{S}$ - $\delta^{34}\text{S}$ diagram with a $\Delta^{33}\text{S}/\delta^{34}\text{S}$ slope

of ~ -0.8 (Farquhar et al., 2001; also see Figure 2). Whereas a compilation of multiple sulfur isotopic data of the relatively well-preserved Archean minerals (mainly pyrite) shows that most of the data distribute along a linear trend on the $\Delta^{33}\text{S}-\delta^{34}\text{S}$ diagram with slopes varying between 0.56 and 0.98, which is referred as ‘Archean reference array’ (ARA; e.g., Kaufman et al., 2007; Thomassot et al., 2015; also see Figure 2). The ARA shares the positive trend with the >220 nm photolytic results but has much higher slopes. Toward a more thorough explanation of the complete dataset (including some scattered data points) of the Archean samples, Ono et al. (2003) proposed a conceptual mixing model between elemental sulfur and sulfate-derived sulfide with variable $\delta^{34}\text{S}$ values as a result of different extent of microbial sulfate reduction (Figure 2). This model can explain most of the Archean data to date (Ono et al., 2003).

One exception to Ono’s model is the multiple sulfur isotope results from the volcanic ash layers in the 3.2 Ga Mapepe Formation in South Africa, which show a negative slope of -0.5 on the $\Delta^{33}\text{S}-\delta^{34}\text{S}$ diagram (Philippot et al., 2012; also shown in Figure 2). This slope is very close to the 193 nm photolysis results. However, Philippot et al. (2012) did not simply explain the trend as a result of the 193 nm photolysis mainly based on the difference in $\Delta^{33}\text{S}/\delta^{34}\text{S}$ slopes. Instead, these authors attributed the observed negative $\Delta^{33}\text{S}-\delta^{34}\text{S}$ trend to some unique photochemical effects (but without detailed explanation in the paper) associated with intensive SO_2 input into the atmosphere by violent volcanic activities in a short time period and therefore named it as “felsic volcanic array” (Phillipott et al., 2012). If this is true, one would expect to observe the “felsic volcanic array” in samples from around 2.7 Ga, which is the peak time of crust growth in the Archean (Condie, 1998). Studies on a few 2.7 Ga sedimentary rocks from the

Kaapvaal Craton, South Africa (Domagal-Goldman et al., 2008), the Abitibi Greenstone Belt, Canada (Jamieson et al., 2013; Kurzweil et al., 2013), and the Bubi Greenstone Belt, Zimbabwe (Marin-Carbonne et al., 2014) have not reported any similar trend so far.

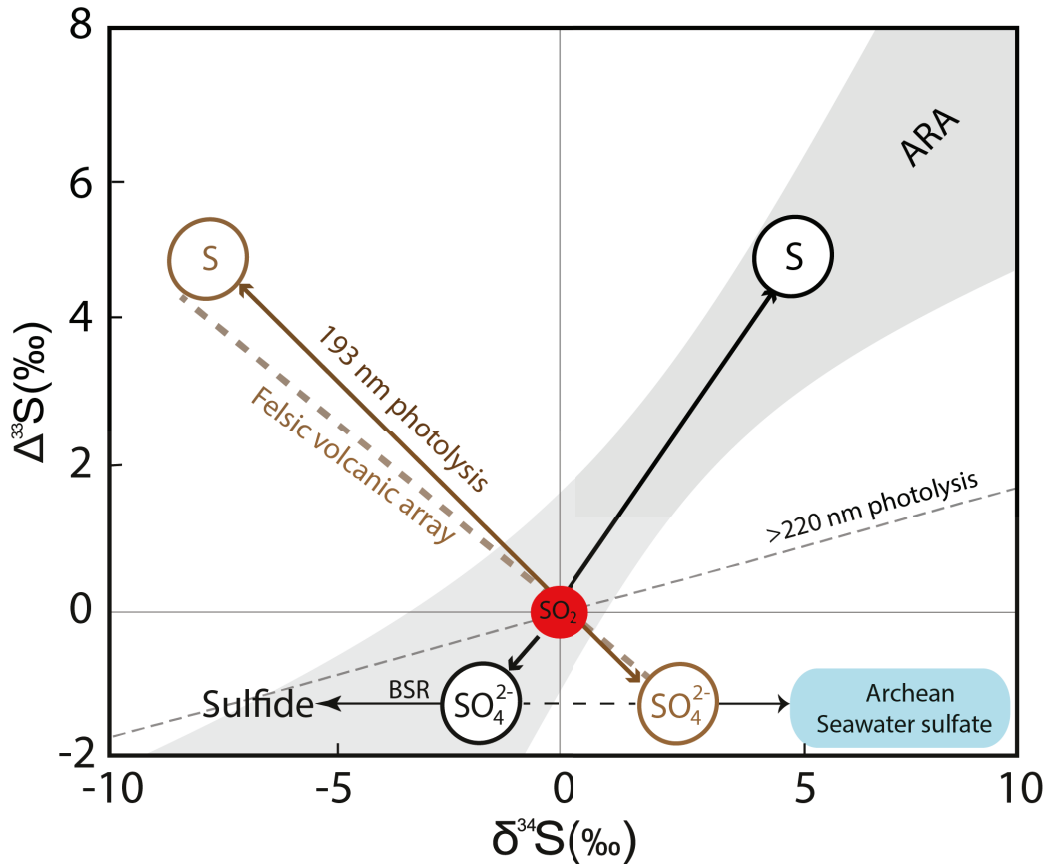


Figure 2. $\Delta^{33}\text{S}$ vs. $\delta^{34}\text{S}$ diagram illustrates the two very different trends (Archean reference array vs felsic volcanic array) observed in the Archean sulfide and sulfate minerals. The trends produced by SO_2 photolysis experiments by UV of 193 nm and >220 nm are also shown for comparison. To explain the Archean data, Ono et al. (2003) proposed a conceptual mixing model between the elemental sulfur endmember and sulfur derived from sulfate with variable $\delta^{34}\text{S}$ controlled by microbial sulfate reduction.

1.2. Pyrite formation

Following the discovery of S-MIF in the Archean rocks (Farquhar et al., 2000) and the mixing model proposed by Ono et al. (2003), the multiple sulfur isotopic compositions of sedimentary sulfides (mainly pyrite) have been widely used to trace the Archean sulfur cycling, particularly the geological and biological processes associated with pyrite formation (e.g., Farquhar et al., 2000, 2007, 2013; Mojzsis et al., 2003; Ono et al., 2003, 2006, 2009a, b; Anbar et al., 2007; Bao et al., 2007; Kamber and Whitehouse, 2007; Philippot et al., 2007; Ueno et al., 2008; Guo et al., 2009; Shen et al., 2009; Thomazo et al., 2009a,b, 2011, 2013; Wacey et al., 2010, 2015; Philippot et al., 2012; Bontognali et al., 2012; Roerdink et al., 2012; Grosch and McLoughlin, 2013; Fischer et al., 2014; Marin-Carbonne et al., 2014; van Zuilen et al., 2014; Zhelezinskaia et al., 2014; Gregory et al., 2015). In sedimentary settings, pyrite is commonly formed during early diagenesis (namely diagenetic pyrite). In some rare cases, pyrite can be formed before diagenesis, in places such as slightly below the sediment-water interface under euxinic environment (Raiswell and Berner, 1985; Suits and Wilkins, 1998; Wilkin and Barnes, 1997) or even in the water column (e.g., modern Black Sea; Lyons, 1997).

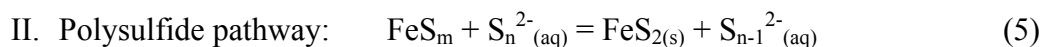
The formation of diagenetic pyrite mainly depends on the chemistry of the pore water and associated biological activities (Canfield and Raiswell, 1991; Raiswell, 1997). Many studies (Berner, 1970; Wilkin and Barnes, 1997; Benning et al., 2000) suggest the formation of pyrite requires the existence of a precursor FeS (e.g., mackinawite; traditionally denoted as FeS_m), which can be formed by the reaction below:



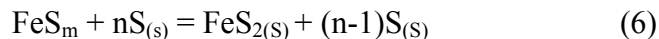
There are four possible ways to produce sulfide from sulfate or elemental sulfur in

water column and diagenetic environments: (1) bacterial sulfate reduction (BSR), during which the sulfide product can be depleted in ^{34}S by up to 70‰ (Canfield et al., 2001; Sim et al., 2011), resulting in shifts in $\delta^{34}\text{S}$ towards negative values for sulfide and positive values for remaining sulfate (Figure 2); (2) bacterial elemental sulfur reduction, which is not associated with significant isotopic fractionation (Canfield and Raiswell, 1999, Canfield, 2001); (3) bacterial elemental sulfur disproportionation (BESD), which can result in ^{34}S - depletion by ~8‰ in the sulfide product (Canfield et al., 1998, Canfield, 2001); and (4) abiotic elemental sulfur disproportionation, which can produce sulfide depleted in ^{34}S by less than 3‰ (Smith, 2000). All these processes are considered to be mass dependent, thus the sulfide product should inherit the $\Delta^{33}\text{S}$ signature from the sulfur sources (i.e., negative values if from Archean sulfate or positive values if from Archean elemental sulfur). In the Archean pyrite S-MIF record, most of the data show positive $\Delta^{33}\text{S}$ values (Figure 1), implying that significant amounts of elemental sulfur have been involved during the pyrite formation.

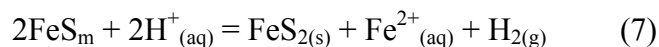
The formation of pyrite from FeS_m is more complicated, probably involving mobilization of multiple species including Fe(II), elemental sulfur, and/or sulfide (Rickard, 2012). Four major pathways have been proposed for the formation of pyrite from its precursor (Berner, 1970; Rickard, 1975, 1997; Rickard and Luther III, 1997; Sweeney and Kaplan, 1973; Luther III, 1991; Schoonen and Barnes, 1991; Wilkin and Barnes, 1996; Benning et al., 2000; Butler et al., 2004), which can be described by reactions below:



III. Solid-state reaction between FeS and S⁰:



IV. Oxidative Fe-loss pathway:



In the sulfide pathway, the sulfur isotopic composition of pyrite is the mean of those of FeS and H₂S reservoirs; both could originate from sulfate and/or elemental sulfur (Butler et al., 2004).

In the polysulfide pathway, S_n²⁻ is formed by the reaction between elemental sulfur and sulfide:



In this scenario, the mixing between one sulfide ion and multiple sulfur atoms in elemental sulfur would result in positive Δ³³S values of polysulfide (Farquhar et al., 2013). It is suggested that sulfur isotopic compositions of pyrite via the polysulfide pathway reflect the source polysulfide pool (Butler et al., 2004; Farquhar et al., 2013).

The solid-state mechanism may apply when FeS_m and elemental sulfur coexist, but require relatively high temperature (>125 °C). When the temperature is below 125 °C, the synthesis of pyrite in an elemental sulfur-rich environment proceeds more likely via the polysulfide pathway rather than the solid-state pathway (Rickard, 1975; Schoonen and Barnes, 1991).

The oxidative Fe-loss pathway (Benning et al., 2000; Wilkin and Barnes, 1996) does not involve any gain or loss of sulfur, thus the pyrite product should inherit the sulfur isotopic composition of the precursor FeS_m (Wilkin and Barnes, 1996), which reflects the isotopic composition of pore water sulfide (Farquhar et al., 2013; Ono et al., 2009a). However, the oxidative Fe-loss pathway is less likely in the Archean because this

pathway occurs in oxic environments (Benning et al., 2000), which has been rarely observed in 2.7 Ga.

Based on pore water chemistry and diagenetic environment, the diagenetic pyrite can display various sizes and shapes (e.g. Passier et al., 1997, Wilkin et al., 1996). The two most common types of morphologies are large nodules (framboidal pyrite) and small euhedral crystals (Love and Amstutz, 1966; Sweeney and Kaplan, 1973; Raiswell, 1982; Passier et al., 1997). Pyrite nodules are generally formed when pore water is oversaturated with respect to both FeS_m and pyrite (Sweeney and Kaplan, 1973; Morse et al., 1987, Roberts and Turner, 1993). In contrast, euhedral pyrite grains would precipitate if pore water is undersaturated with respect to FeS_m , but oversaturated with respect to pyrite (Goldhaber and Kaplan, 1974; Raiswell, 1982; Wang and Morse, 1996; Rickard, 1997). In this scenario, laboratory experiments suggest that even if the system is undersaturated with respect to FeS_m , FeS_m still locally precipitates but dissolves very quickly (Rickard, 1975, 1997; Schoonen and Barnes, 1991; Luther III, 1991).

1.3. Metamorphic effect on sulfur isotopic compositions of pyrite

To date, all the studies of Archean sulfur cycle and Earth's early biological activities using the multiple sulfur isotopes have relied on a few diagenetic sulfide minerals (a majority as pyrite) and minor sulfate minerals (e.g., barite and gypsum) in the Archean supracrustal rocks in South Africa, Australia, North America, and Greenland. An important premise that enables the use of multiple sulfur isotopes to make inferences about the Archean environment and biological properties is that the Archean sulfide and sulfate minerals have preserved their pristine multiple sulfur isotopic signatures with little

secondary disturbance. However, all Archean supracrustal rocks discovered so far have gone through greenschist-facies or higher-grade metamorphism (e.g. Card, 1990). The investigations focusing on the metamorphic effect on sulfur isotopic compositions of Archean rocks are very few. A study on the greenschist-facies Kaapvaal shales by Watanabe et al. (1997) showed that these rocks contained very low sulfur contents (nearly half of which $< 0.01\%$, averaging 0.1%), which were attributed to sulfide loss by leaching of metamorphic fluid (Watanabe et al., 1997). If any significant sulfur remobilization occurred during metamorphism, such as sulfide overgrowth from metamorphic fluid or solid-state isotopic exchange between sulfide minerals and metamorphic fluid, the pristine isotopic signature of the diagenetic sulfide could be overprinted. This concern has to be clarified before one can use the isotopic signatures to infer any Archean environment and biological activities. However, traditional isotope analysis using bulk sample powder is unlikely to achieve this goal due to the difficulty in distinguishing between the primary and secondary isotopic signatures.

1.4. High-resolution *in-situ* analysis on single pyrite grains to uncover primary signals

Secondary ion mass spectrometry (SIMS) allows isotopic (e.g. C, H, O, N, S, etc.) analysis at a spatial resolution as small as $\sim 15 \mu\text{m}$ (Williams, 1985; Benninghoven et al., 1987; Vickerman et al., 1989). Early SIMS sulfur isotope studies were mainly focused on ^{34}S and ^{32}S analysis and have demonstrated strong sulfur isotope heterogeneity and zonation patterns in single pyrite grains, which were explained as the product of multiple sulfur sources (e.g., Peevler et al., 2003) or complicated ^{34}S -discriminating processes

(e.g., McKibben et al., 1994) during pyrite formation. Recent developments of SIMS have enabled measurements of less abundant sulfur isotopes of ^{33}S and ^{36}S (e.g., Farquhar et al., 2002; Mojzsis et al., 2003; Thomassot et al., 2009; Kozdon et al., 2010; Whitehouse et al., 2013). Such developments significantly advance the study of Archean sulfur cycle by analyzing μm -scale pyrite grains while still maintaining data at high precision. More recently, SIMS has been used for detailed sulfur isotopic mapping ($\delta^{34}\text{S}$ and $\Delta^{33}\text{S}$) of large Archean pyrite nodule grains, which also showed strong isotopic variation across the grains (e.g., Fischer et al., 2014; Marin-Carbonne et al., 2014). Fisher et al. (2014) further demonstrated that the strong sulfur isotopic variation could be caused by both paleoenvironment changes during the growth of the diagenetic pyrite and late alteration. To distinguish between these possibilities, some other high-resolution techniques, such as magnetic microscopy and petrography in their case, have to be integrated with SIMS analysis (Fischer et al., 2014).

Electron microprobe analysis (EPMA) is another commonly used *in-situ* analytical technique that can provide high-resolution element concentrations on μm scale. This technique has been used as a routine method to determine the major- and minor-element compositions of minerals. In pyrite, the major elements are Fe and S and the common trace elements of interest are Cu, Ni, Mn, etc. Because metamorphic fluids are generally characterized by trace element concentrations different from diagenetic pore water, comparison of trace element concentrations (e.g. Cu, Ni) between different generations of pyrite grains would be very helpful to distinguish diagenetic pyrite components from the pyrite components overprinted by metamorphic fluid (e.g. Fleet and Mumin, 1997; Deditius et al., 2008; Reich et al., 2013, Marin-Carbonne et al., 2014).

In this study, I use SIMS and EPMA techniques to investigate pyrite grains in the organic- and pyrite-rich 2.7 Ga shale samples from the Joy Lake sequence (Minnesota, USA) in the Deer lake greenstone belt of the Superior Province, which have gone through lower-greenschist-facies metamorphism (Yang et al., 2009). I identified multiple types of pyrite, including large pyrite nodules (0.3 to 1 cm in size; diagenetic origin) and small subhedral pyrite grains (tens of μm in size; related to metamorphic fluid) either disseminated in quartz veins cutting or surrounding the pyrite nodules or aligned along fractures (in lamina shape) in the rock. The purpose of this study is to obtain *in-situ* elemental and multiple sulfur isotopic data to: (1) investigate the distribution patterns of elements and sulfur isotopic ratios in the pyrite grains; (2) assess the regional metamorphic effect on elemental and sulfur isotopic signatures of diagenetic pyrite nodules; and (3) infer the photochemical and biological processes controlling the sulfur cycle in 2.7 Ga.

2. Geological setting

The Joy Lake supracrustal sequence in northern Minnesota (USA) lies in the western Wawa subprovince of the Superior Province (Figure 3). The geology in this area is poorly characterized. Most of the available information is based on very few outcrops and drill core samples (Jirsa et al., 1992; Corfu and Stott, 1998; Severson and Jirsa, 2006), which are briefly summarized below.

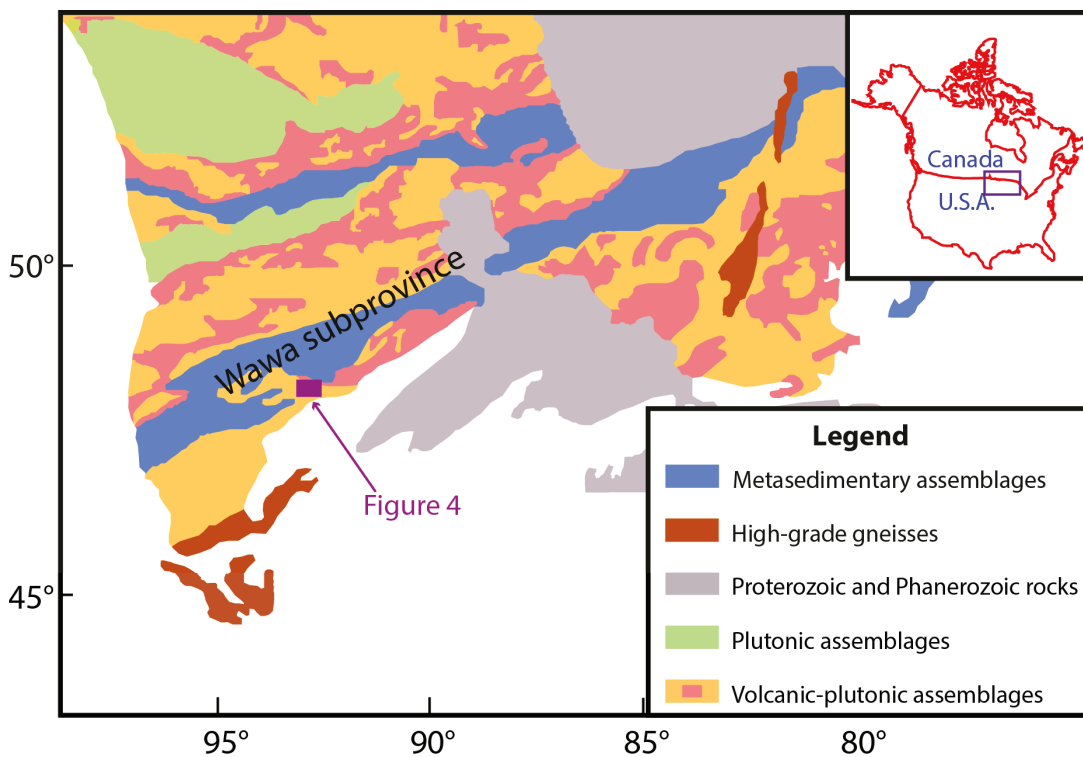


Figure 3. Geological map of southern Superior Province (summarized from Card, 1990; Percival et al., 1994; and Yang et al., 2009).

The Joy Lake sequence (see Figure 4), which is bound by poorly studied granitic rocks in the northwest and the Coon Lake plutonic syenite in the south, mainly consists of sedimentary rocks and volcanic rocks varying from basaltic to andesitic in composition (Severson and Jirsa, 2006). Owing to the scarcity of both outcrops and drill holes, most parts of the Joy Lake sequence are poorly studied except the sedimentary unit at the top of the sequence (i.e., Ajs on Figure 4). The Ajs unit sits stratigraphically on top of a volcanic unit (Ajv on Figure 4) consisting of dacite, andesite, quartz latite tuff, breccia and hornblende andesite tuff as well as some interbedded thin layers of volcanoclastic greywacke and conglomerate (Severson and Jirsa, 2006), which has been folded to the top of Ajs unit (see Figure 4). The Ajs unit is younging northwest and contains interbedded shale and greywacke layers ranging from 1 cm to 0.5 m in thickness, as well as minor organic-rich slate, chert, and felsic to mafic tuff (Severson and Jirsa, 2006). The greywacke unit in Ajs is dominated by turbidites, indicating a high-density flow environment. Based on occurrence of both organic-rich and volcanic units in Ajs, Severson and Jirsa (2006) suggested an anoxic depositional environment relatively proximal to a volcanic arc. The depositional age of Ajs is between 2720 ± 3 Ma, which is the zircon U-Pb age of the underlying volcanic rocks Ajv from the eastern Wawa subprovince (Corfu and Stott, 1998), and 2695 ± 14 Ma, which is the pyrite Re-Os age of the organic-rich slates from the upper sedimentary layer (also the samples in this study) in the Joy Lake sequence (Yang et al., 2009).

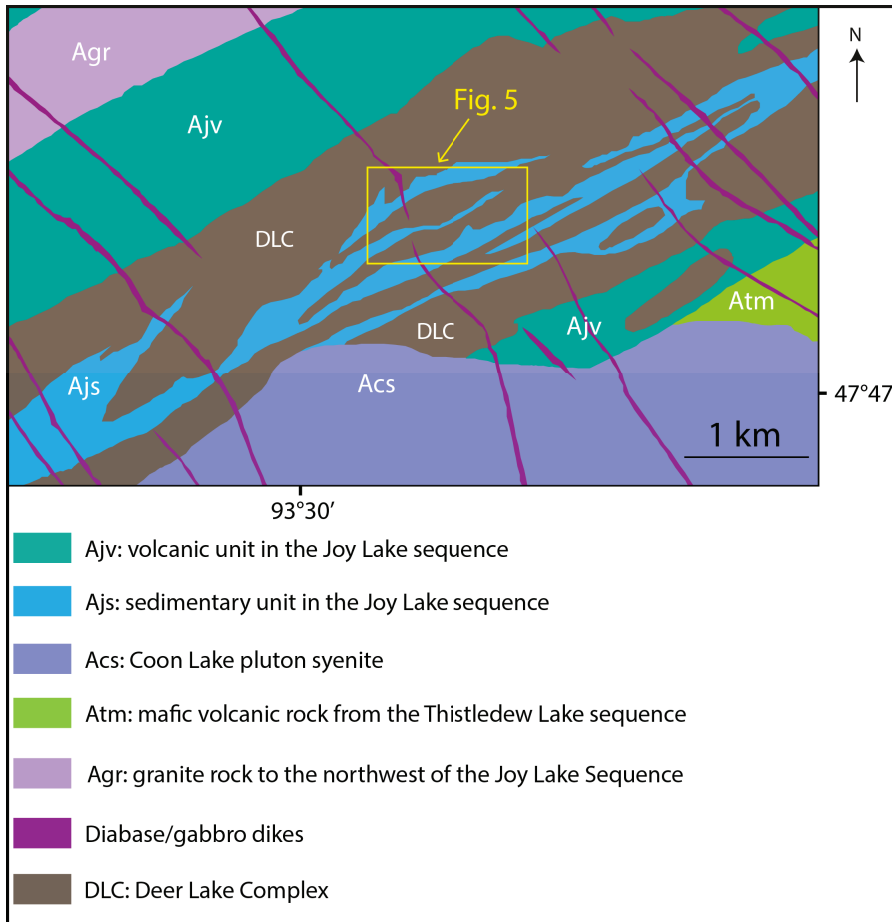


Figure 4. Geological map of Joy Lake Sequence (modified from Severson and Jirsa, 2006).

Previous studies described three generations of structures in the Ajs sedimentary rocks: (1) two early deformations (namely D0 and D1 deformations in previous studies) associated with folding that produced the nappe structures over a large area (Bauer, 1985, Jirsa et al., 1992). The exact ages of D0 and D1 are not given, but likely occurred very shortly after the sedimentary rocks were formed (Jirsa et al., 1992); (2) a slightly later northwest-directed D2 deformation overprinting earlier D0 and D1 structures corresponds to the peak regional greenschist-facies metamorphic event (Jirsa et al., 1992; Corfu and Stott, 1998; Percival et al., 2006, Yang et al., 2009). The metamorphic age, constrained

by zircon U-Pb age of the pre- to syn-D2 granodiorite in the western Wawa subprovince, is ~2680–2685 Ma (Boerboom and Zartman, 1993), very close to the sedimentary age (2695 ± 14 Ma; Yang et al., 2009). Before the peak regional metamorphism, the sedimentary sequence was intruded by the Deer Lake Complex (Figure 4), which is composed by gabbroic body, peridotite-pyroxenite-gabbro sills and ultramafic lenses (Berkley et al., 1978; Ripley, 1979, 1983; Ripley et al., 1982; Jirsa, 1990; Severson and Jirsa, 2006). The age the Deer Lake Complex has not been reported and the intrusion effect on the sedimentary unit was not well identified in previous studies. A recent Re-Os study by Yang et al. (2009) suggested that at least the Re-Os system had not been disturbed since the formation of the sedimentary rocks; and (3) the latest deformation (referred as D3 in previous studies) caused by north-south compression occurred at the waning stage of D2 deformation (Jirsa et al., 1992). D3 is characterized by a NE-trending fabric and brittle structures that can be observed in syntectonic plutonic rocks. Both D2 and D3 affected most of the southern Superior Province (Bauer, 1986, Jirsa et al., 1992). Both the sedimentary sequence and the Deer Lake Complex were intruded by the Proterozoic Kenora-Kabetogama diabase dike swarms with an age of 2076 Ma (Buchan et al., 1996; Southwick and Day, 1983). The narrow Kenora-Kabetogama diabase dikes mostly intruded in the volcanic units and are relatively rare in the sedimentary units (see Figures 4 and 5) and thus show very little influence on the sedimentary unit (Jirsa et al., 1992; Yang et al., 2009).

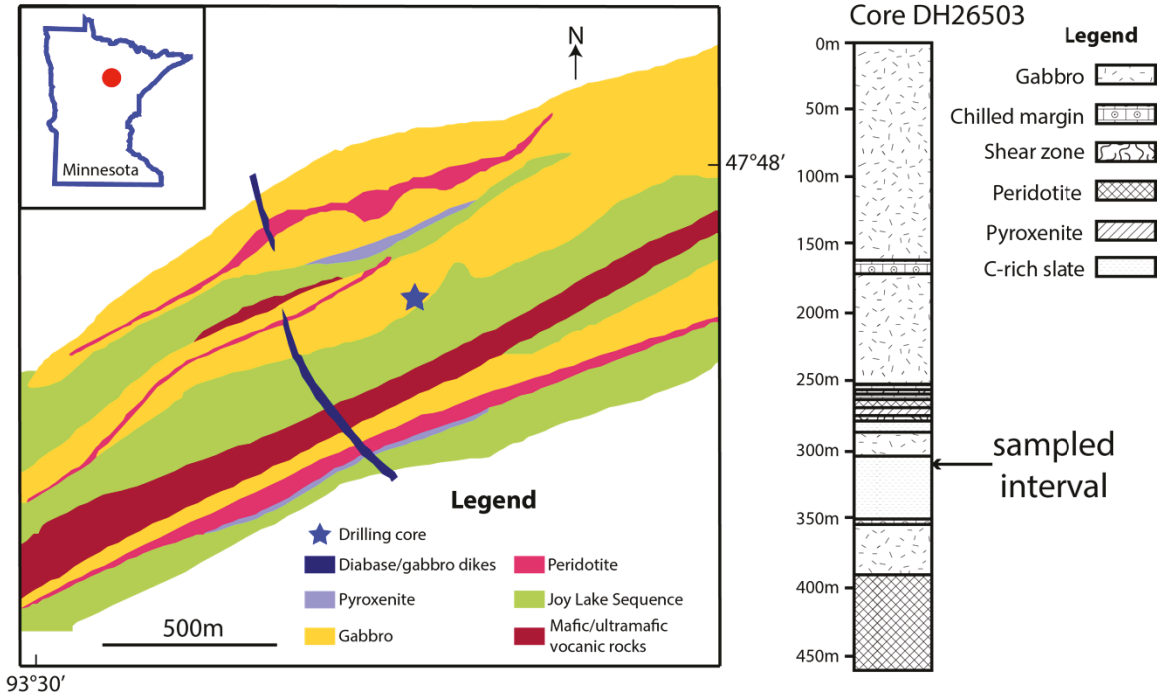


Figure 5. Geological maps of drill core location (left) and generalized drill core log for DH26503 (right; from Severson and Jirsa, 2006; Yang et al., 2009). See detailed description in text.

3. Sample description

The Joy Lake shale samples that were examined in this study, which had previously been studied for Re-Os geochronology (Yang et al., 2009) are from drill core DH26503 (Figure 5). The core intersects shale of the Ajs unit and intrusive bodies of gabbro, pyroxenite and peridotite of DLC. Two strategies were applied for sample selection for this study: (1) to avoid direct thermal influence from the very last intrusions, samples were selected as far as possible away from the intrusive contacts (Figure 5); and (2) to minimize age variations, samples were selected from a short depth interval of ~2.1 m (between 304.8 m-306.9 m; Figure 5).

All shale samples consist of massive-bedding fine-grained black matrix (>80%), quartz veins (<10%), and sulfide minerals (<10%). Pyrite is the major sulfide mineral and occurs as nodules, disseminated grains and bedding-parallel seams (Ripley and Nicol, 1981; Severson and Jirsa, 2005). Two representative samples (ORG-44 and ORG-45) were selected for detailed petrographic characterization and elemental and sulfur isotope studies. Sample characterization by hand-specimen observation and scanning electron microscope (SEM) imaging using back-scattered electrons (BSE) is described below.

3.1. Hand-specimen observation

Due to limited amounts of the available samples (less than 10 gram each), we do not have enough material to make thin sections. Thus petrographic observation is mainly based on hand specimen. Observation on pyrite grains in several shale samples from drill core DH26503 gives very similar petrographic features: (1) pyrite nodules (3 mm to 1 cm in diameter) are surrounded and sometimes truncated by quartz veins; (2) fine-grained

(usually less than 100 μm in diameter) subhedral pyrite grains disseminate in quartz veins. As examples, we show below the details of the two samples selected for elemental and sulfur isotope studies:

ORG-44 (Figure 6): from depth of 304.8-305.4 m

This sample contains two relatively large ellipsoidal pyrite nodules, both of which are surrounded by later quartz together with sparse fine subhedral pyrite grains (~ 40 to $80 \mu\text{m}$ in diameter; only observable under microscope; see BSE images in Figures 10-12). One nodule was broken into several pieces, whereas the other one remains intact. Abundant quartz veins, in which fine-grained subhedral pyrite crystals (20 - $80 \mu\text{m}$ in diameter) can also be found under microscope, occur in the matrix. Although strongly deformed, the quartz veins appear to distribute along two major directions and truncate each other (Figure 6), suggesting that the two directions of quartz veins likely infilled conjugate joint sets. The joint structure is considered to be formed during D2 (metamorphic deformation) for two reasons: (1) the late deformation of the quartz veins can be only attributed to D3 and thus the quartz vein structure has to be earlier than D3; and (2) no clear structures were identified in previous studies for the pre-metamorphic intrusion of the Deer Lake Complex, which makes D2 the only option for the development of the quartz vein structure. The close association of the fine-grained subhedral pyrite with quartz veins suggests this type of pyrite grains were formed together with quartz. This conclusion is further supported by the subhedral (instead of euhedral) shape of these pyrite grains, which suggests that these pyrites share the same evolution history with quartz veins — both were deformed by D3.

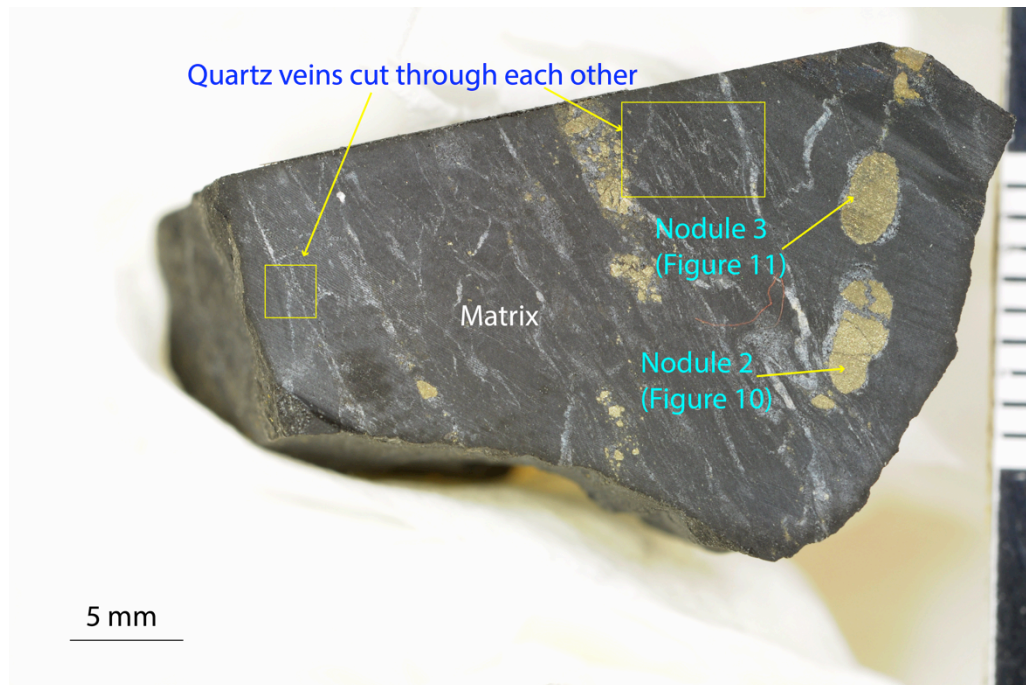


Figure 6. Photo of black shale sample ORG-44. Sample contains two nodules, ~3 mm in diameter. Both nodules were surrounded by quartz veins; one of them was broken into several pieces. Abundant quartz veins exist in the sample. Although strongly deformed, the quartz veins appear to distribute along two major directions and truncate each other (see the boxed area). Detailed BSE images of pyrite nodules and are shown in Figure 10 and Figure 11.

ORG-45 (Figure 7): from depth of 306.3 m

This sample contains one large pyrite nodule (1 cm in diameter) surrounded by a thin layer of quartz. Disseminated subhedral pyrite grains (about 40-80 μm in diameter; observable under microscope; also see Figure 8) occur in the quartz layer. The quartz veins in the dark matrix in this sample are thin and align mainly along one direction, but deformed to sigmoidal shape around the large pyrite nodule. To be consistent with sample ORG-44, we attribute the formation of these quartz veins to D2 and the deformation of the vein to D3. In addition, a thin lamina consisting of mainly subhedral to anhedral pyrite (Figure 9, hereafter referred as lamina pyrite) and minor quartz occurs in parallel to the quartz veins at 1 mm away from the nodule (Figure 7).

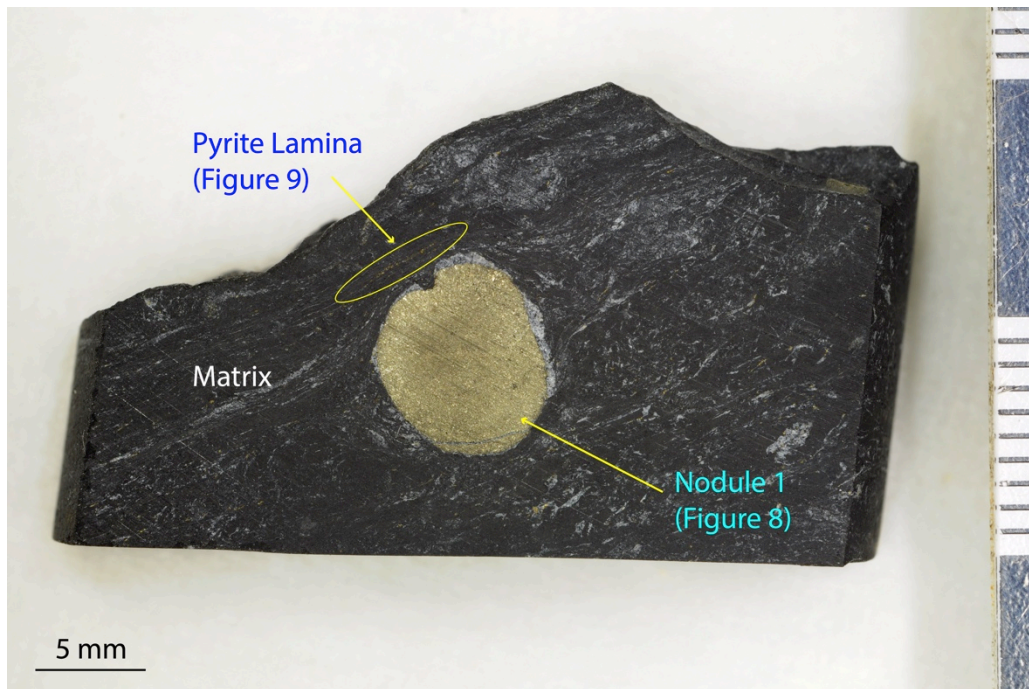


Figure 7. Photo of black shale sample ORG-45. Sample contains one large pyrite nodule, ~1 cm in diameter. The nodule is surrounded by quartz. A lamina consisting of tiny pyrite grains (tens of μm) and minor quartz grains occurs ~1 mm away from the nodule. See details in SEM pictures of pyrite nodule (Figure 8) and lamina pyrite (Figure 9).

3.2. SEM observation

To further characterize these pyrite grains, BSE imaging was carried out on (1) the 3 large pyrite nodules in ORG-44 and ORG-45, (2) subhedral pyrite grains associated with quartz in ORG-44, and (3) the lamina pyrite grains in ORG-45. The BSE images are shown in three different ways: (A) true color grey scale images (Figures 8A, 10A, 11A), in which the grey scale is a function of the BSE signal intensity; (B) colorized images (Figures 8B, 10B, 11B) by direct conversion from grey scale to color scale using the software “ImageJ” provided by National Institutes of Health; and (C) contrast-enhanced images (Figures 8C, 10C, 11C) from the colorized images (Figures 8B, 10B and 11B) by exaggerating the color difference to better illustrate the minor compositional differences

inside individual grains. Each sample is briefly described below:

ORG-45: BSE images of the large pyrite nodule (hereafter referred as Nodule 1; Figure 8) and the lamina pyrite near Nodule 1 (Figure 9) were acquired in this sample. True color images (Figures 8A and B) of Nodule 1 show only slight color difference across the entire grain, indicating that the chemical compositions do not vary greatly across the nodules. However, the contrast-enhanced images (Figure 8C) show clear zonation pattern. Based on Figure 8C, four zones can be identified in Nodule 1: Zone I, the core of the nodule, displays brighter color than the surrounding Zone II; Zone II is a thin layer displaying the darkest color in the nodule; zones III and IV are brighter than zones I and II; Zone IV shows coarser aggregation pattern and much less inclusions (as dark specks) than the other zones. The pyrite lamina consists of small pyrite grains (20-80 μm) coexisting with quartz; the shapes of pyrite grains vary from subhedral to anhedral (Figure 9).

ORG-44: Two pyrite nodules (hereafter referred as Nodule 2 and Nodule 3; Figure 10 and Figure 11) resemble Nodule 1 in their shape and texture. Comparing with Nodule 1, nodules 2 and 3 display even more vague difference in their true color images, implying smaller variations in chemical composition in these two nodule grains. Even though, a zonation pattern can be still identified in the contrast-enhanced BSE images for both nodules (Figure 10C and Figure 11C). Different from Nodule 1, which displays four distinct zones, only three zones can be identified in nodules 2 and 3. Based on the comparison of color and inclusion abundance among these three nodules, the three zones (from inside to outside) of nodules 2 and 3 can be correlated to zones I, II and III of Nodule 1. Subhedral pyrite grains (~ 40 to $80 \mu\text{m}$ in diameter; Figure 12) in the quartz

veins surrounding or cutting nodules 2 and 3 show slightly brighter color than the nodules (Figure 10C and Figure 11C).

In order to (1) examine the elemental and isotopic patterns of different zones in the pyrite nodules and (2) compare the elemental and isotopic signatures between the pyrite nodules, the lamina pyrite and the subhedral pyrite, we selected one cross-section on each nodule grain, 22 spots on lamina pyrite grains and 11 spots on subhedral pyrite grains to analyze their elemental compositions using EPMA and sulfur isotopic compositions using SIMS.

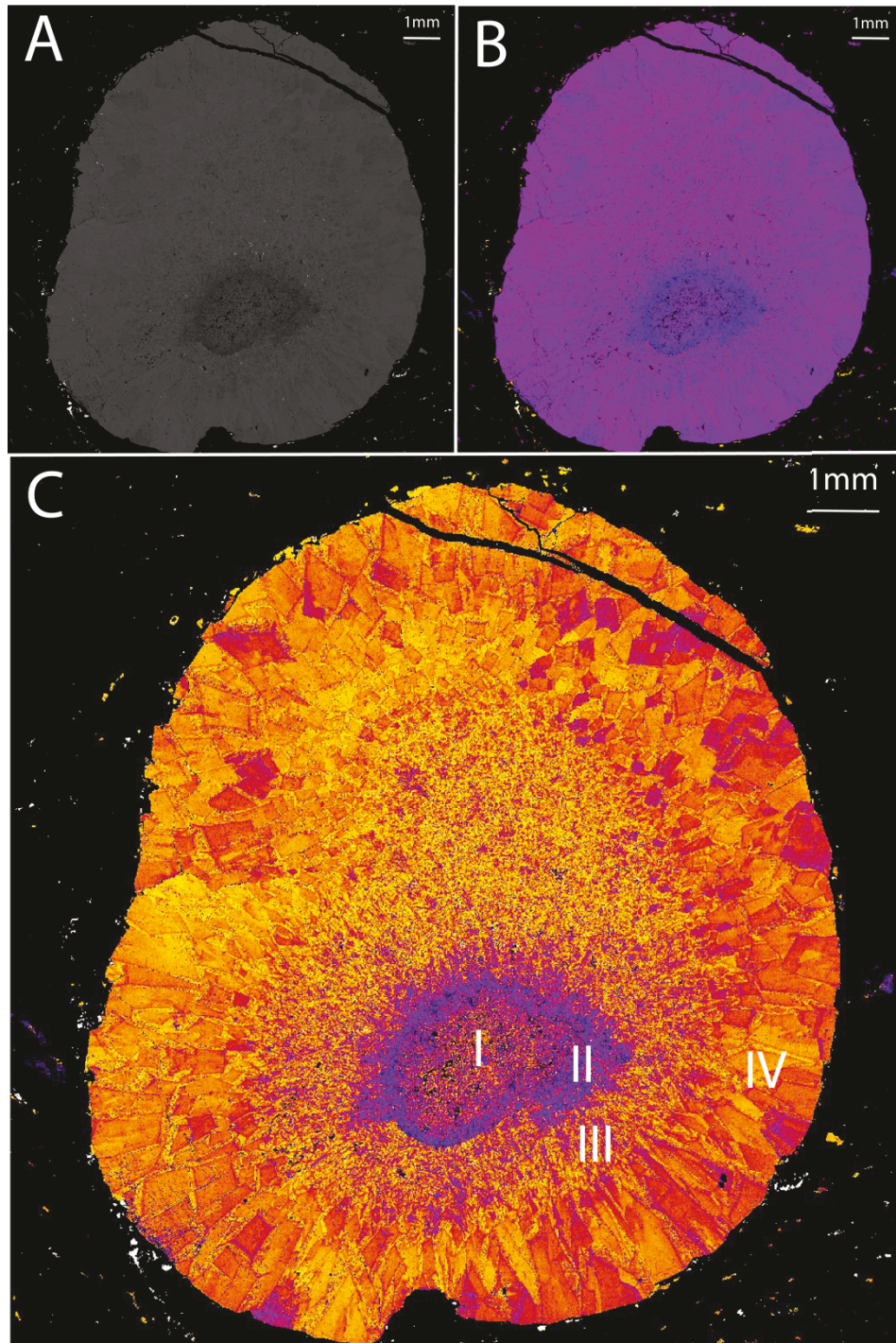


Figure 8. BSE image of pyrite Nodule 1. A: true color grey scale BSE image; B: colorized image of picture A; C: contrast-enhanced picture from B to exaggerate chemical heterogeneity in Nodule 1. A distinct zonation pattern can be observed in panel C. Small disseminated pyrite grains are also observed around the nodule.

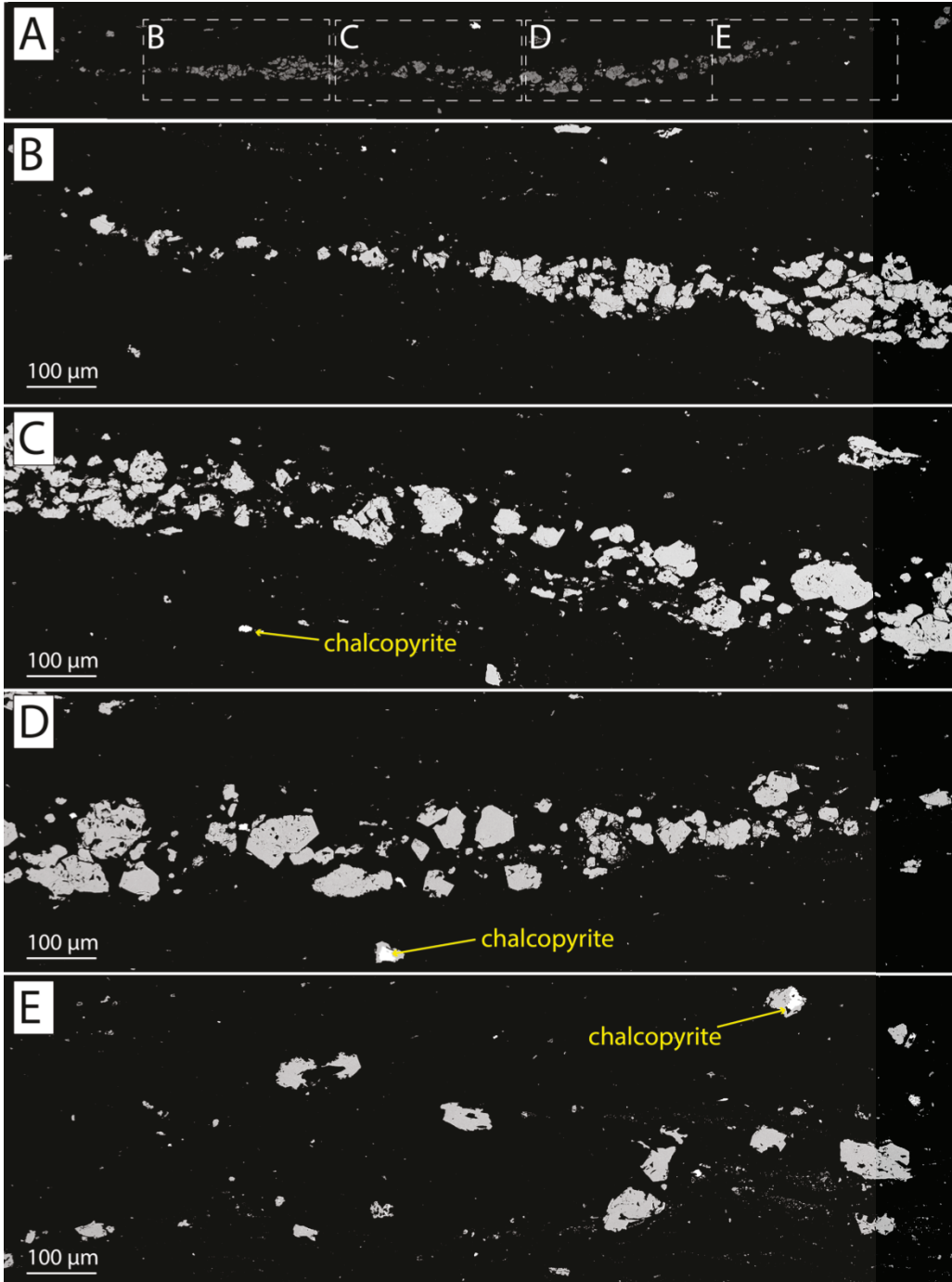


Figure 9. BSE image of lamina pyrite in ORG-45. The lamina is ~8 mm in length and ~100 μm in width. The entire view is shown in panel A, with enlarged sections being shown in B-E. In the lamina, pyrite is the major mineral, although minor chalcopyrite is observed as well. Pyrite grains are subhedral to anhedral, 20-80 μm in diameter. Some of the grains are fractured while others are not. Also existing in the lamina are some quartz minerals, which are shown as black in the image and thus cannot be seen clearly in the BSE images.

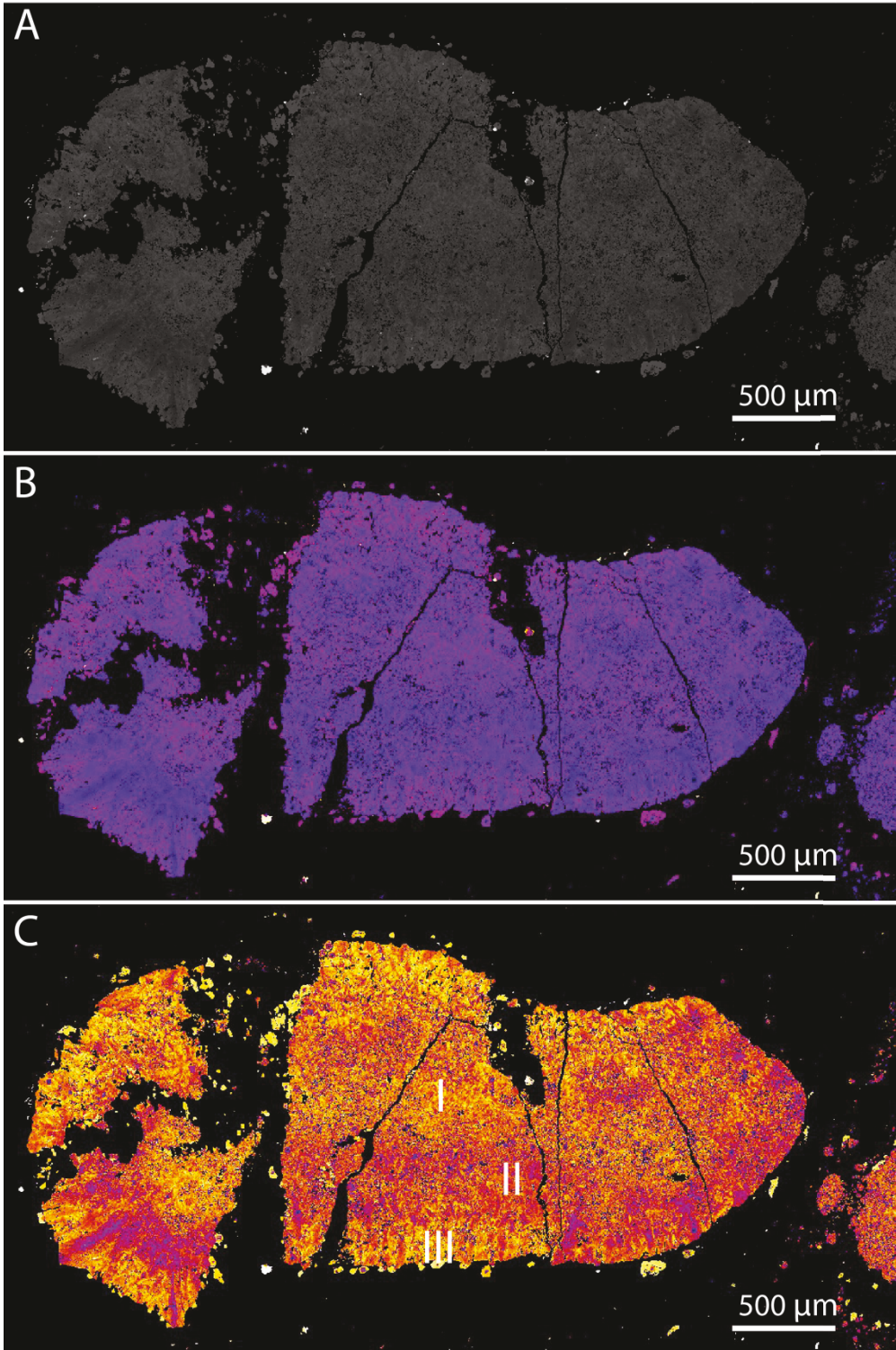


Figure 10. BSE image of Nodule 2. A: true color grey scale image; B: colorized image of picture A; C: contrast-enhanced picture from B to exaggerate chemical heterogeneity in the nodule. Nodule 2 was broken into of several pieces and fractures, indicating severe post-depositional deformation. Although not as clear as Nodule 1, this nodule also shows zonation pattern. Many subhedral grains (40 to 80 μm) are present around the nodule some of which are in direct contact, while others locate slightly away from the nodule.

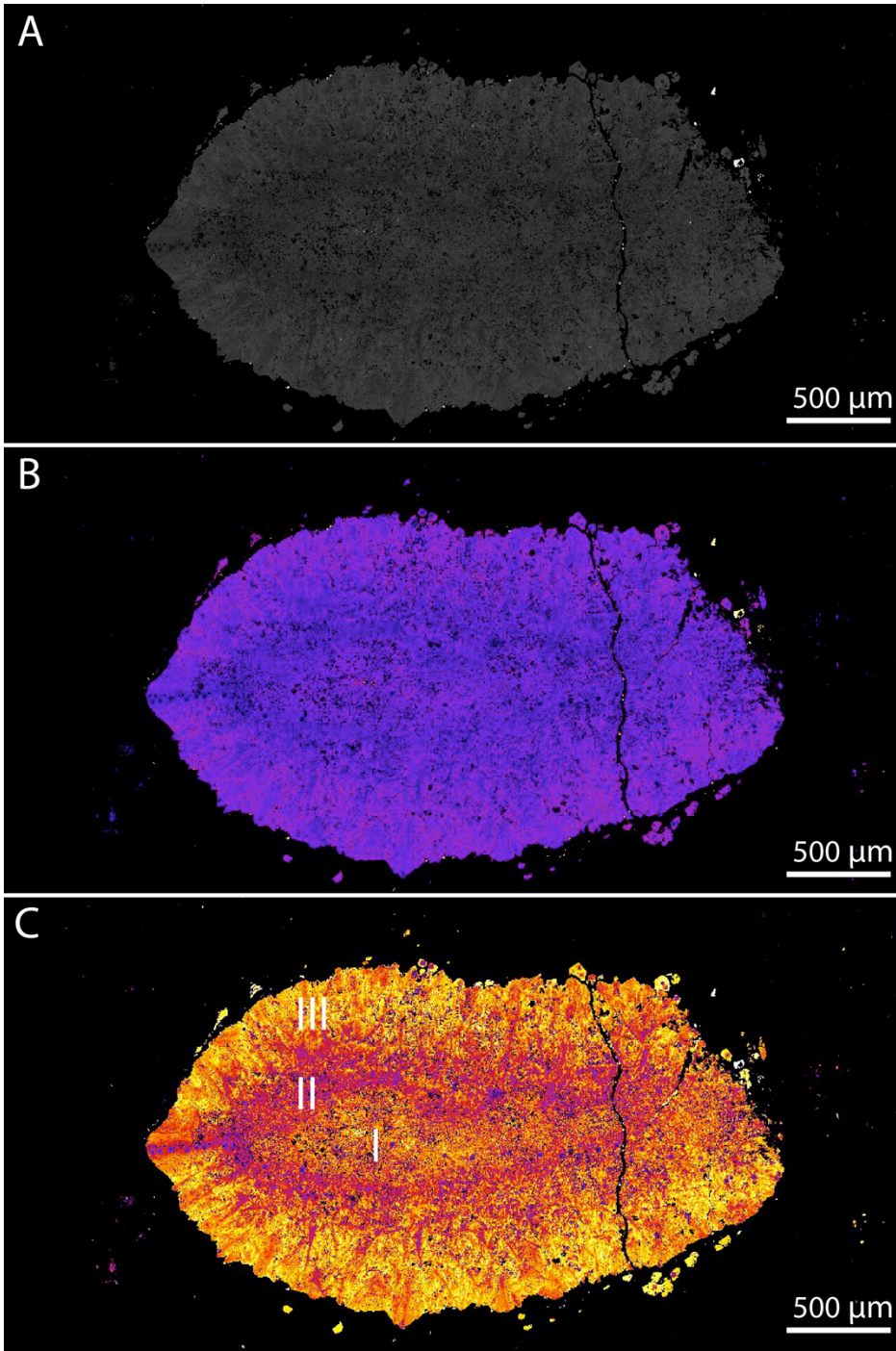


Figure 11. BSE image of Nodule 3. A: true color grey scale image; B: colorized image of picture A; C: contrast-enhanced picture from B to exaggerate chemical heterogeneity in the nodule. Nodule 3 is relatively less fractured than Nodule 2. The zonation pattern can also be observed, with a darker inner part and a lighter outer part. Subhedral grains, of similar size to those observed around Nodule 2, are found along the rim as well.

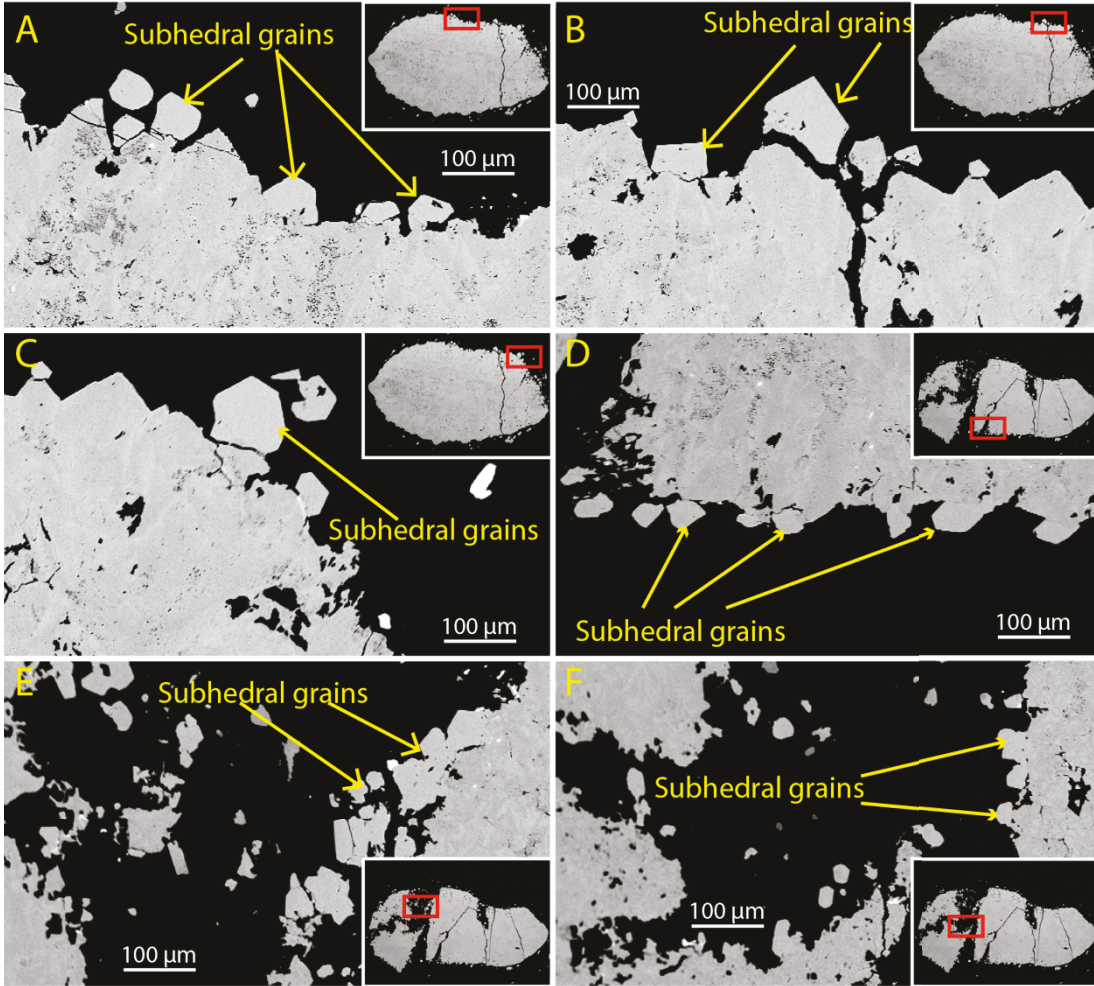


Figure 12. BSE image showing subhedral grains along rim of pyrite nodules 2 and 3. The exact position of the image relative to the pyrite nodules are shown in the inserted panel. All subhedral grains have similar size, ranging from 40 to 80 μm , but variable shapes.

4. Method

4.1. Element concentration analysis using EPMA

The pyrite samples were prepared on a standard epoxy mount (25 mm in diameter) that can be used for both EPMA and SIMS measurements. Rock fragments ranging from 3 to 10 mm wide from the two samples (ORG-44 and ORG-45) were cast in epoxy. The sample surface was polished and then coated with 25 nm of carbon. Elemental concentrations (Fe, S, Cu and Ni) of pyrite grains were analyzed using a Cameca SX 100 electron probe microanalyzer (EPMA) equipped with 5 tuneable wavelength-dispersive spectrometers in the Electron Microprobe Laboratory at the University of Alberta. This EPMA, which has a 40-degree take off angle, was operated at 15 keV accelerating voltage and 200 nA beam current. Peak and background counting times were 30 seconds and 15 seconds, respectively for all elements. To remove the background effect, a linear off-peak correction method was applied.

Two strategies were applied to measure element concentrations in our samples. For pyrite nodules, traverse lines close to the SIMS cross-section spots were selected to run EPMA analysis at ~ 20 μm intervals. For subhedral and lamina pyrite grains, measurements were carried out close (generally < 20 μm) to individual SIMS spots. All elemental results were reported in weight percentage. The standard for EPMA analysis is FeS_2 , which contains 46.55% Fe, 53.45% S, 0.000% Ni and 0.000% Cu (a total of 99.7% to 100.1%). Analytical uncertainties (2σ) based on the analysis of the standard FeS_2 over the course of this study are 0.28% for Fe, 0.12% for S, 0.003% for Ni, and 0.003% for Cu.

4.2. Multiple sulfur isotope analysis using SIMS

The mount was ground and polished using 1 μm diamond pads, cleaned, and then coated with 7 nm of Au to conduct BSE imaging. After BSE imaging, additional Au was added to the mount (to a total of 30 nm) prior to isotope analysis by SIMS. The measured spots were selected in locations void of observable inclusions.

Sulfur isotopic ratios ($^{34}\text{S}/^{32}\text{S}$, $^{33}\text{S}/^{32}\text{S}$) were determined using the IMS-1280 multi-collector ion microprobe in the Canadian Centre for Isotopic Microanalysis (CCIM) at the University of Alberta. Primary beam conditions included the use of 20 keV $^{133}\text{Cs}^+$ ions to form a probe with diameter of $\sim 15 \mu\text{m}$ and beam current of $\sim 1.5 \text{ nA}$. The internal pyrite reference material (CCIM pyrite S0302A) was analyzed after every 4 analyses of unknowns. Pyrite S0302A is from a highly metamorphosed ore in the 1.9 Ga Flin Flon belt, Manitoba, Canada. S0302A has been demonstrated by previous SIMS scans to have homogeneous $\delta^{34}\text{S}$ and $\Delta^{33}\text{S}$ values, which were recently determined by conventional SF_6 method as $-0.2 \pm 0.2\text{‰}$ and $-0.03 \pm 0.01\text{‰}$, respectively (R. Stern, unpublished data).

The isotopic compositions are reported relative to the VCDT standard. The overall analytical uncertainties (2σ), incorporating within-spot counting errors to account for the stability of the instruments, between-spot errors to account for geometric effects, and between-session error to account for long-term instrumental drift, are 0.12‰ for $\delta^{34}\text{S}$ and 0.12‰ for $\Delta^{33}\text{S}$.

5. Results

5.1. Element concentrations in pyrite

Results of *in-situ* analysis of Fe, S, Cu and Ni concentrations of different types of pyrite are listed in Table 1 in the supplementary material and briefly described below.

5.1.1. Pyrite nodules

Total element concentrations (Total% = Fe% + S% + Ni% + Cu%) and Ni and Cu concentrations across each nodule grain are shown in Figure 13 and summarized below.

All three nodules show similar range in Total% from 93% to 99% with most analyses yielding Total% between 95% and 98% (Figure 13D-F). The Fe concentrations of nodules vary from 42.3% to 45.5%, with average values of 44.7%, 44.0% and 44.3% for nodules 1, 2 and 3, respectively (Table 1), and sulfur concentrations vary from 49.3% to 53.5%, with average values of 52.4%, 51.8% and 51.7% for nodules 1, 2 and 3, respectively (Table 1). The molar S/Fe ratio calculated for each analyzed spot displays a very limited range from 2.01 to 2.08 throughout the three nodules, with average values of 2.04 ± 0.02 (2σ , $n = 340$), 2.05 ± 0.02 (2σ , $n = 152$), and 2.03 ± 0.02 (2σ , $n = 142$) for nodules 1, 2 and 3, respectively (Table 1). This further verifies the three nodules are FeS₂. Observations under reflected light microscope suggest the mineral is isotropic, indicating it is pyrite rather than marcasite. Trace element (Ni and Cu) concentrations, however, show more significant cross-section variations. Ni concentrations in the three nodules mostly lie in the range from below detection limit (<0.006%) to 0.15%, with a few spots going up to 0.30% (Figure 13G-I). In Nodule 1, a treatment of the Ni concentration data by 15-period simple moving average indicates a sharp decrease from ~0.13% in Zone I to

~0.07% in Zone II, followed by a steady increase back to ~0.12% in Zone III, and a sharp decrease to below detection limit in Zone IV (Figure 13G). However, in nodules 2 and 3, Ni concentration does not show systematic variation across Zone I to Zone III (Figure 13H, I). Cu concentration of most of the spots in the three nodules spread in the range from below detection limit (<0.006%) to 0.06%, with a few spots going up to 0.19% (Figure 13J-L). In Nodule 1, the 15-period simple moving average of Cu concentration data shows the cross-grain variation not as significant as the one of Ni except an obvious decrease in Zone IV (with quite some spots below detection limit, Figure 13J). Nodules 2 and 3 do not show much Cu variation across the grains (Figure 13K, L).

5.1.2. Subhedral pyrite grains along nodule margins

EPMA analysis was carried out on a spot less than 20 μm away from each SIMS spot in the subhedral pyrite grains. Ni and Cu concentrations are shown in Figures 14 and 15. Ni concentrations from 10 subhedral grains close to nodules 2 and 3 show large variations from 0.012% to 0.102%. In contrast, 5 comparison spots on the rim of Nodule 2 close to the measured subhedral pyrite grains display a smaller variation from 0.070% to 0.089%. Cu concentrations of the subhedral pyrite grains and comparison spots show even more distinct feature: half of the measured subhedral pyrite grains contain undetectable Cu (< 0.006%), and the other half contain small amount of Cu ranging from 0.012% to 0.029%. In contrast, the comparison spots show higher Cu concentrations and a tighter range from 0.032% to 0.046% (Figure 15). Fe and S concentrations show little variations among all the subhedral pyrite grains: from 44.2% to 45.8% (average: 44.9% \pm 1.2%; 2σ , n= 10) for Fe, 51.3% to 53.2% for S (average: 52.3% \pm 1.4%; 2σ , n= 10), and S/Fe molar ratios range from 2.01 to 2.05 (average: 2.03 \pm 0.02; 2σ , n=15; see Table 1).

5.1.3. Lamina pyrite

Fe and S concentrations in lamina pyrite again show little variations, from 44.1% to 45.7% (average: $45.1\% \pm 0.9\%$; 2σ , $n = 22$) for Fe and 51.3% to 53.4% (average: $52.8\% \pm 1.2\%$; 2σ , $n = 22$) for S, and S/Fe molar ratio from 1.96 to 2.08 (average: 2.04 ± 0.06 ; 2σ , $n=22$; Table 1). However, trace-element measurements of 22 spots on the lamina pyrite grains gave Ni concentrations from below detection limit to 0.451%, and Cu concentrations from below detection limit to 0.075% (Figures 16 and 17). The measured spots on the lamina pyrite grains can be divided into two distinct groups based on Ni and Cu concentration data (Figure 17): Group 1 consists of 10 spots, showing low Ni concentrations (from below detection limit to 0.023%) and relatively high Cu concentrations (from 0.017% to 0.075%); Group 2 include the rest 12 spots, showing relatively high Ni concentrations (from 0.101% to 0.452%) and low Cu concentrations below detection limit. The distribution of these two groups of data is highly heterogeneous and analytical spots belonging to different groups can be as closely spaced as less than 50 μm (Figure 16C).

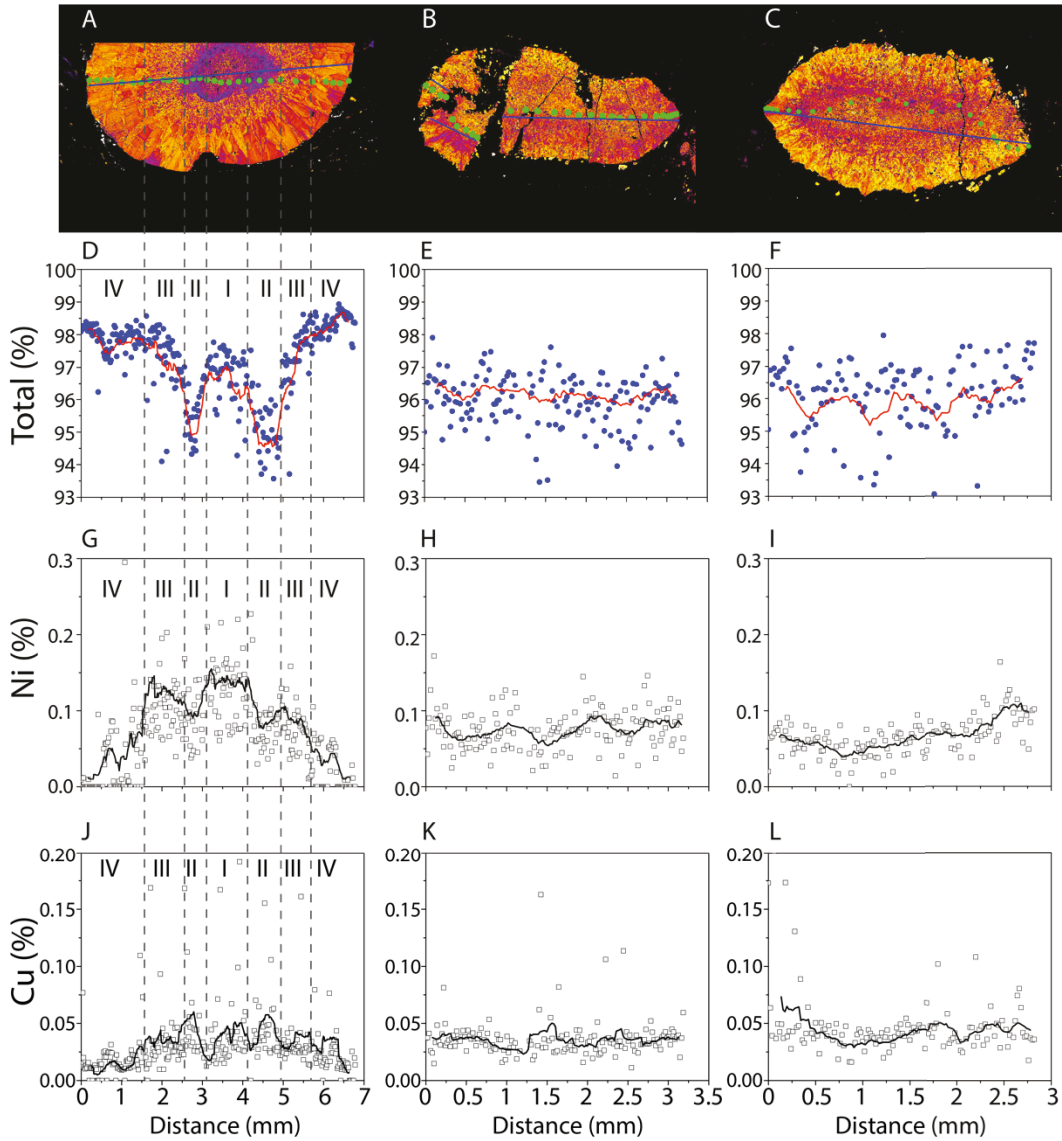


Figure 13. Cross-section variations of total element concentrations (Fe% + S% + Cu% + Ni%) and trace element concentrations (Cu% and Ni%) in three pyrite nodules. A-C: colored BSE images indicating the traverses for EPMA (blue lines) and SIMS (white dots) analyses; D-F: Total element concentrations; G-I: Ni concentrations; J-L: Cu concentrations. Data points that lie on x-axis represent concentrations below detection limit of 0.006%. Solid lines in D-L are 15-period simple moving average of Ni and Cu concentrations. All error bars are smaller than symbols.

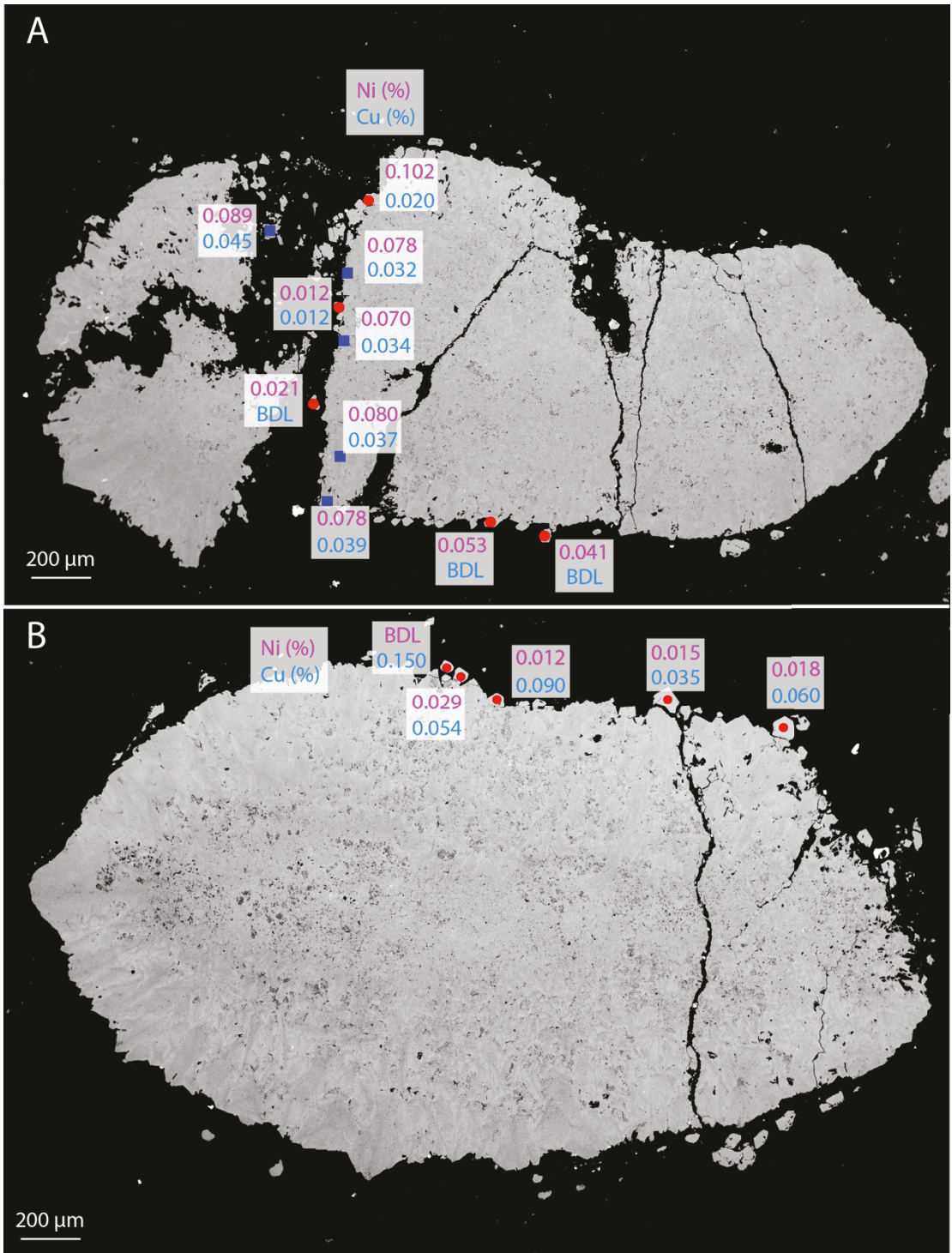


Figure 14. Trace element concentrations (Ni in pink and Cu in blue) of (A) subhedral pyrite grains (solid red circles) and adjacent comparison points (solid blue squares) in Nodule 2; and (B) subhedral pyrite grains close to Nodule 3. BDL denotes concentrations are below detection limit.

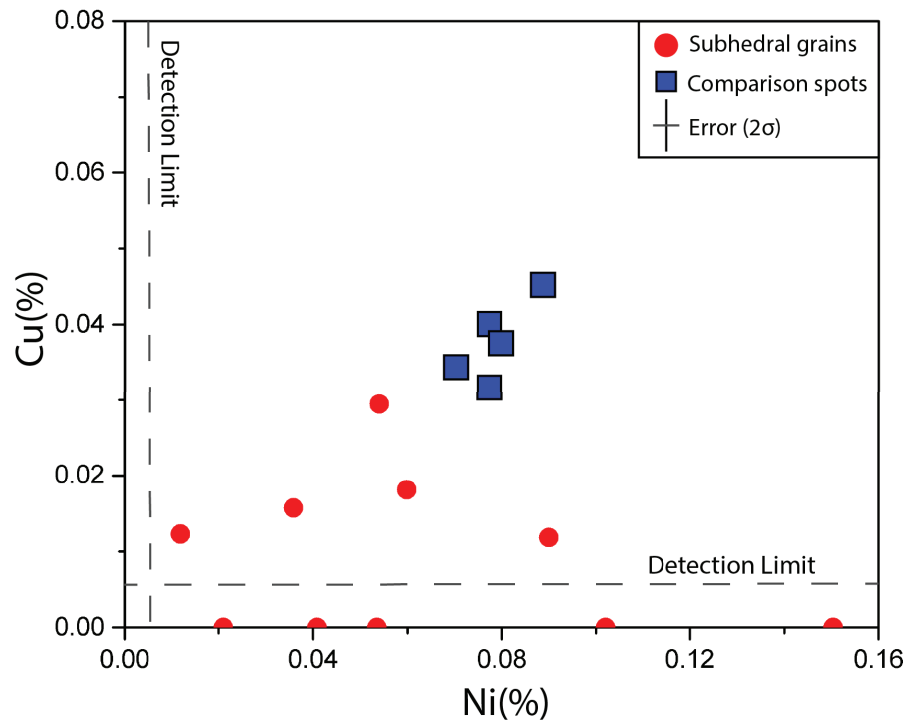


Figure 15. Cu and Ni concentrations of subhedral pyrite grains (red dots) close to nodules 2 and 3, and nearby comparison spots (blue squares) on the rim of Nodule 2. Dashed lines represent the detection limits (both 0.006%) of Ni and Cu measurements. Data points that lie under (for Cu) or on the left (for Ni) of the dashed line represent concentrations below detection limit.

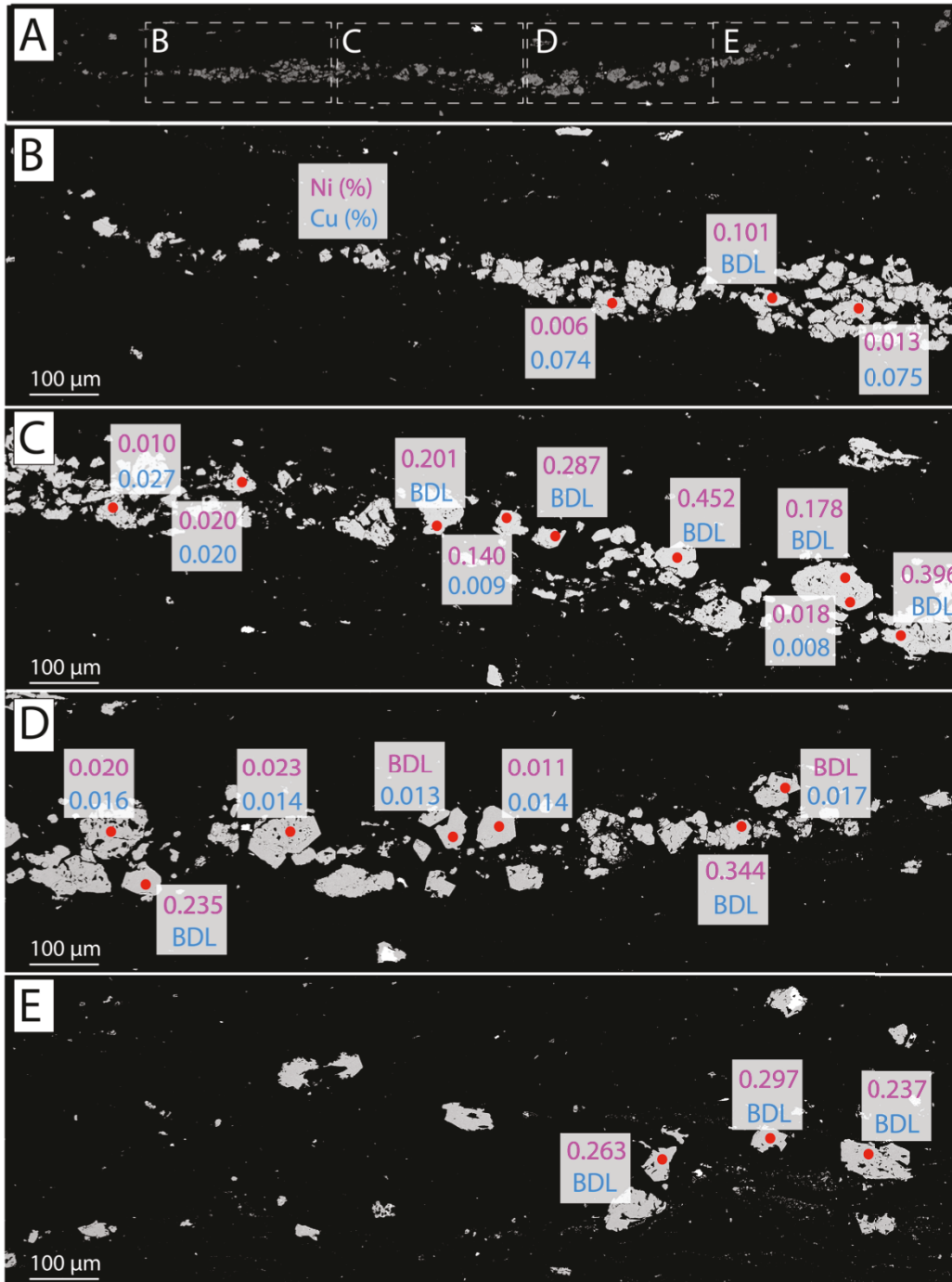


Figure 16. Cu and Ni concentrations of lamina pyrite (panel A). Analysis locations (red circles) together with their Ni% (in pink) and Cu% (in blue) are shown in enlarged pictures in panels B-E. BDL denotes concentrations are below detection limit.

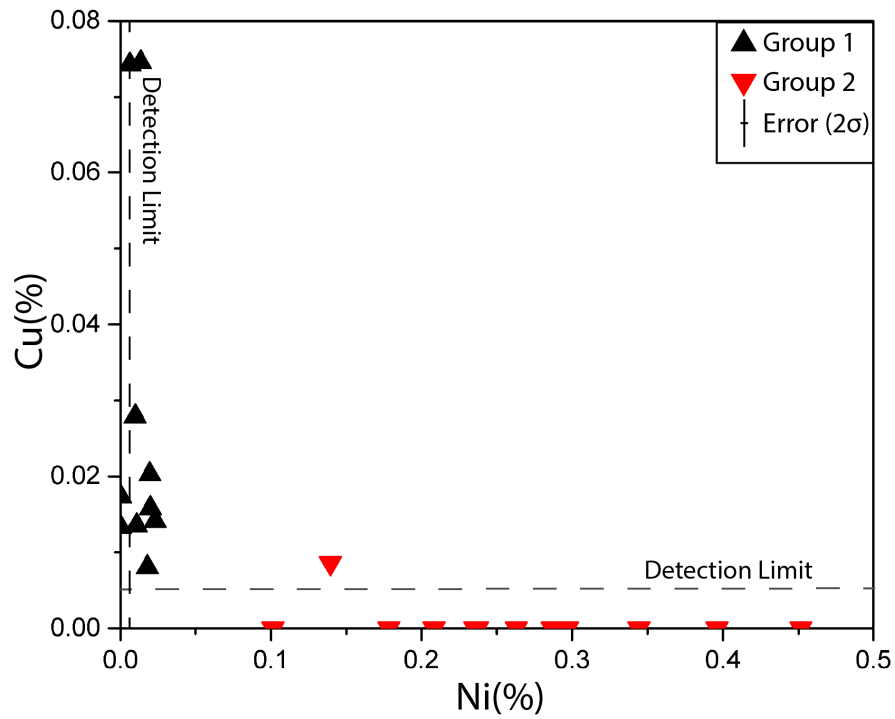


Figure 17. Cu and Ni concentrations of pyrite grains in the lamina show a bimodal distribution. Dashed lines denote the detection limits of Ni and Cu measurements; both are 0.006%. Data points that lie under (for Cu) or on the left (for Ni) of the dashed line represent concentrations below detection limit.

5.2. Multiple sulfur isotopic compositions of pyrite

Multiple sulfur isotopic compositions for all the samples are listed in Table 2 in the supplementary material. The data show an overall range from -2.9‰ to +7.7‰ in $\delta^{34}\text{S}$ value and from +0.6‰ to +4.8‰ in $\Delta^{33}\text{S}$ value. Detailed sulfur isotopic signatures of each type of pyrite are described below.

5.2.1. Pyrite nodules

Cross-section $\delta^{34}\text{S}$ and $\Delta^{33}\text{S}$ values for nodules 1, 2 and 3 are plotted in detail in Figures 18 to 20, respectively. All three pyrite nodules display prominent cross-section variations in both $\delta^{34}\text{S}$ and $\Delta^{33}\text{S}$ values (Figure 21). Nodules 1, 2 and 3 show $\delta^{34}\text{S}$ ranges from -2.9‰ to +2.0‰, -2.0‰ to +1.0‰, -2.7‰ to +0.6‰ and $\Delta^{33}\text{S}$ ranges from +0.7‰ to +2.5‰, +0.8‰ to +2.3‰, +0.6‰ to +2.3‰, respectively (Figure 21D-F). Coarse negative correlations are observed between $\delta^{34}\text{S}$ and $\Delta^{33}\text{S}$ values in all three nodules (Figure 21G-I).

5.2.2. Subhedral pyrite grains in quartz veins

Successful measurements on 9 subhedral grains in the quartz veins surrounding or cutting through nodules 2 and 3 gave a large range in $\delta^{34}\text{S}$ value from +3.2‰ to +7.7‰, but a small range in $\Delta^{33}\text{S}$ value from +4.1‰ to +4.8‰ (Figures 22 and 23). For comparison, 5 measurements made on the rim of Nodule 2 close to the subhedral pyrite grains gave distinct ranges of -2.6‰ to +0.4‰ in $\delta^{34}\text{S}$ value and +1.4‰ to +1.7‰ in $\Delta^{33}\text{S}$ value (Figures 22 and 23).

5.2.3. Lamina pyrite

The detailed isotope results of 22 measured spots on the lamina pyrite grains adjacent to Nodule 1 are shown in Figure 24. The data show an overall range from -2.7‰ to 5.1‰ in $\delta^{34}\text{S}$ value and from 2.5‰ to 4.0‰ in $\Delta^{33}\text{S}$ value. Similar to Cu and Ni concentrations, sulfur isotopic compositions in the lamina pyrite are also highly heterogeneous but cluster into two groups, matching well with the two groups defined by Cu and Ni concentrations. Group 1 (corresponding to low Ni concentrations and high Cu concentrations) has ranges of -2.7‰ to -1.1‰ in $\delta^{34}\text{S}$ value and 2.5‰ to 2.9‰ in $\Delta^{33}\text{S}$ value. Group 2 (corresponding to high Ni concentrations and low Cu concentrations) has much higher $\delta^{34}\text{S}$ (2.5‰ to 5.1‰) and $\Delta^{33}\text{S}$ (3.6‰ to 4.0‰) values (Figure 25).

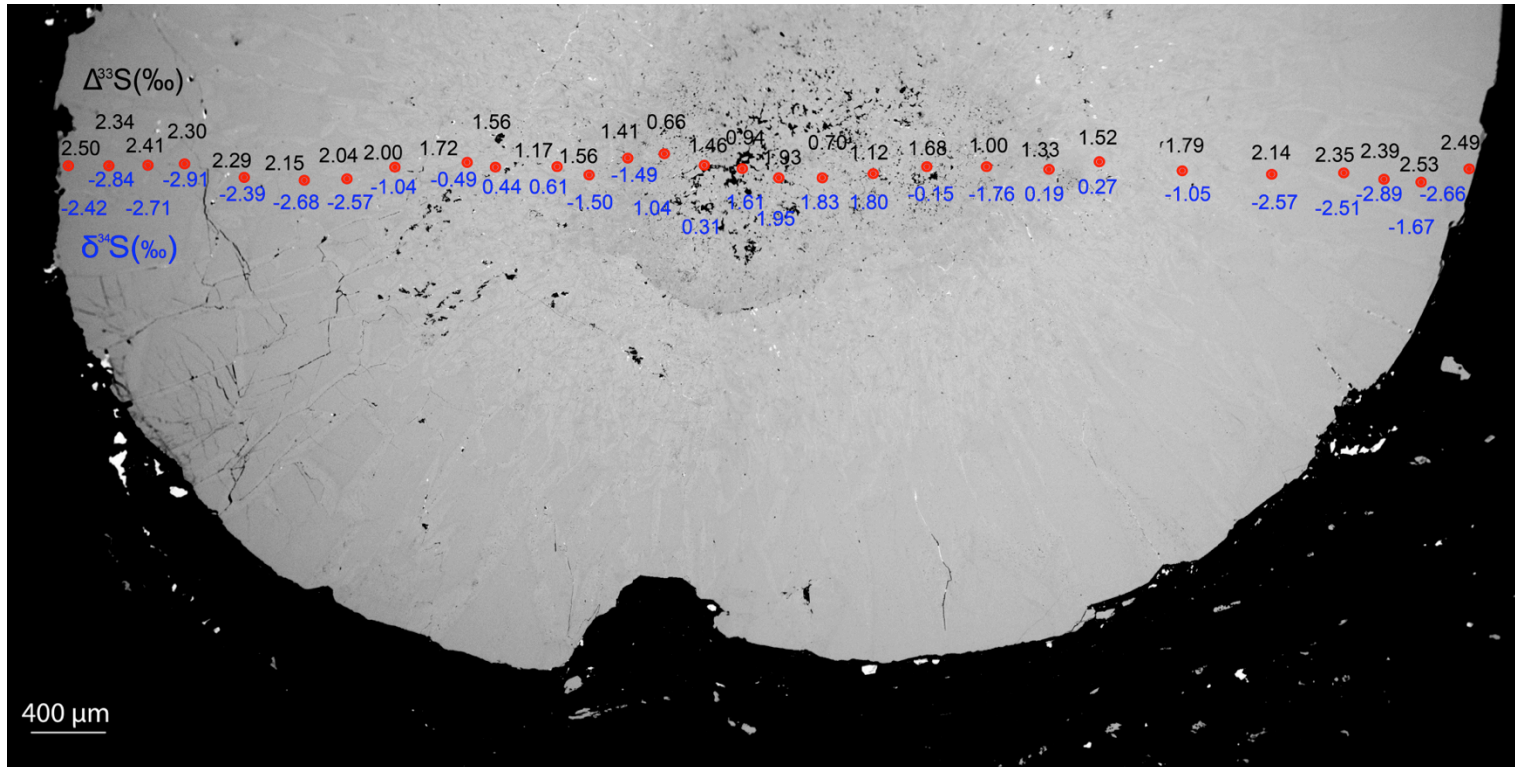


Figure 18. Cross-section sulfur isotopic compositions of Nodule 1. The analyzed spots are marked as red circles with $\Delta^{33}\text{S}$ values in black and $\delta^{34}\text{S}$ values in blue.

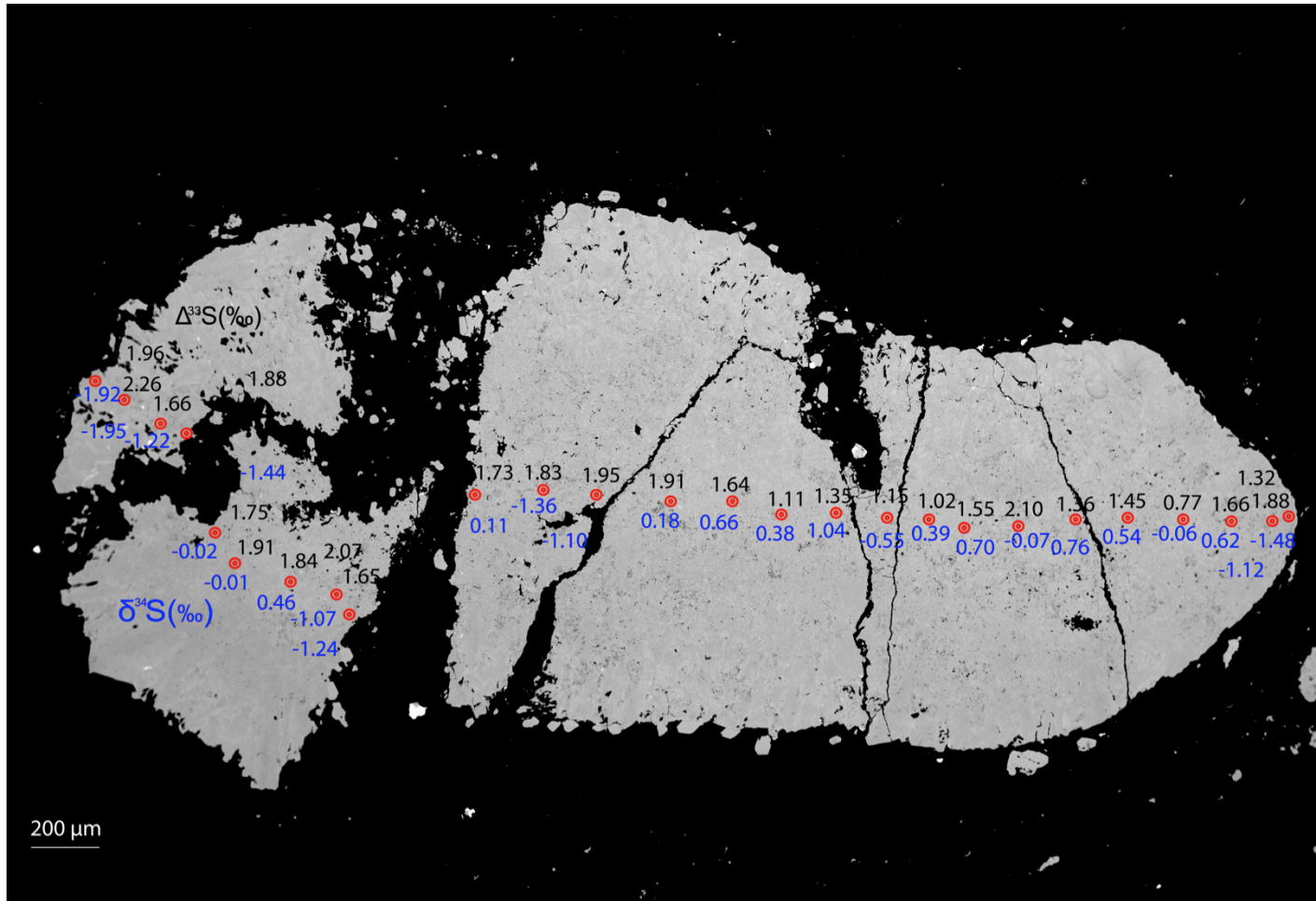


Figure 19. Cross-section sulfur isotopic compositions of Nodule 2. The analyzed spots are marked as red circles with $\Delta^{33}\text{S}$ values in black and $\delta^{34}\text{S}$ values in blue.

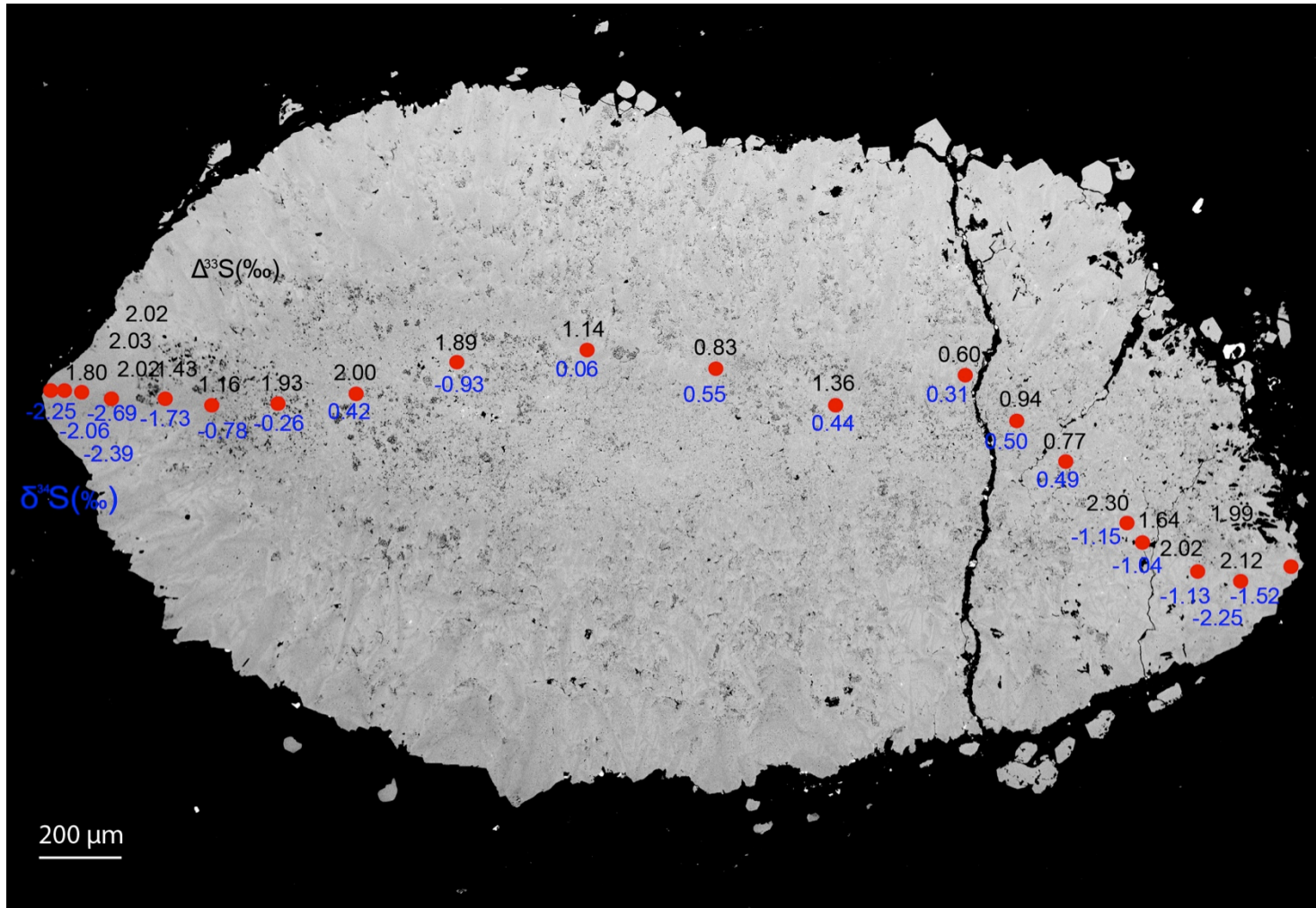


Figure 20. Cross-section sulfur isotopic compositions of Nodule 3. The analyzed spots are marked as red circles with $\Delta^{33}\text{S}$ values in black and $\delta^{34}\text{S}$ values in blue.

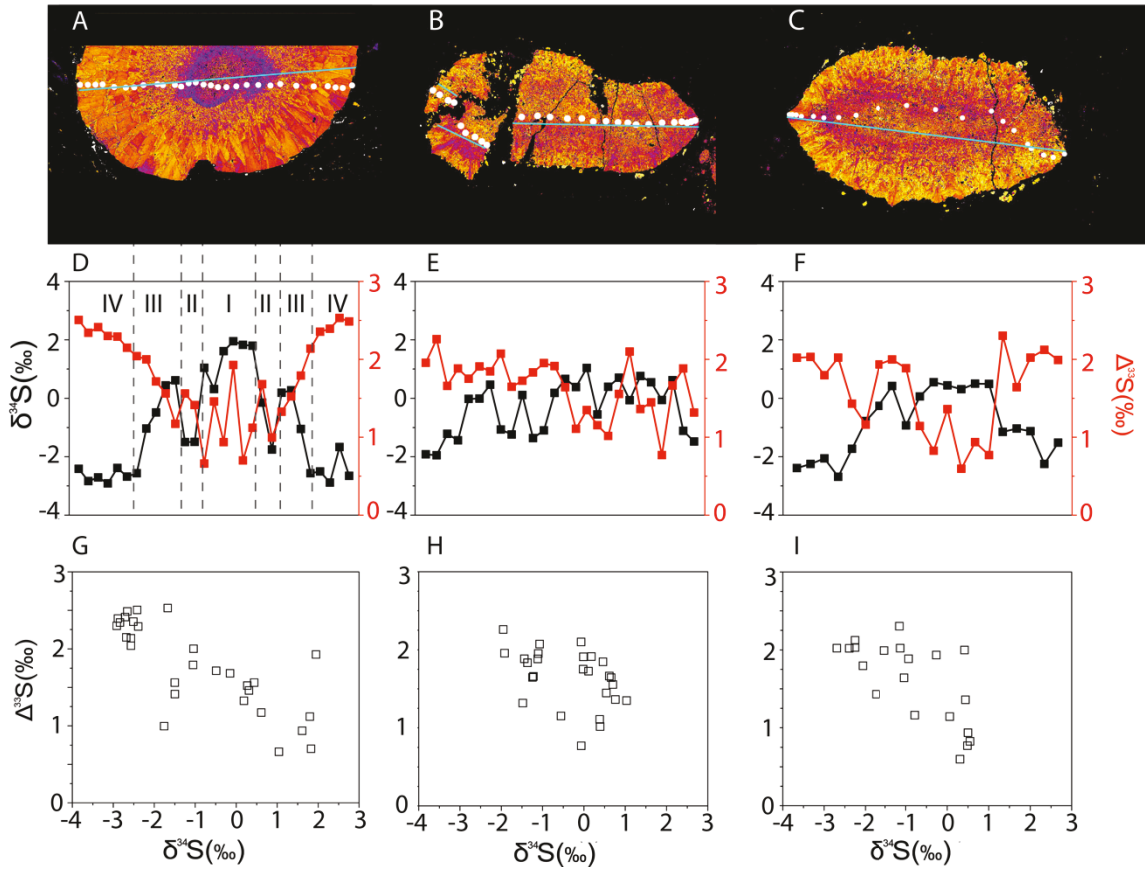


Figure 21. Pyrite nodules 1-3 (A-C) show strong cross-section heterogeneities in $\delta^{34}\text{S}$ (in black) and $\Delta^{33}\text{S}$ (in red) values (D-F) and co-variation between $\Delta^{33}\text{S}$ and $\delta^{34}\text{S}$ values (G-I). Error bars are all smaller than symbols.

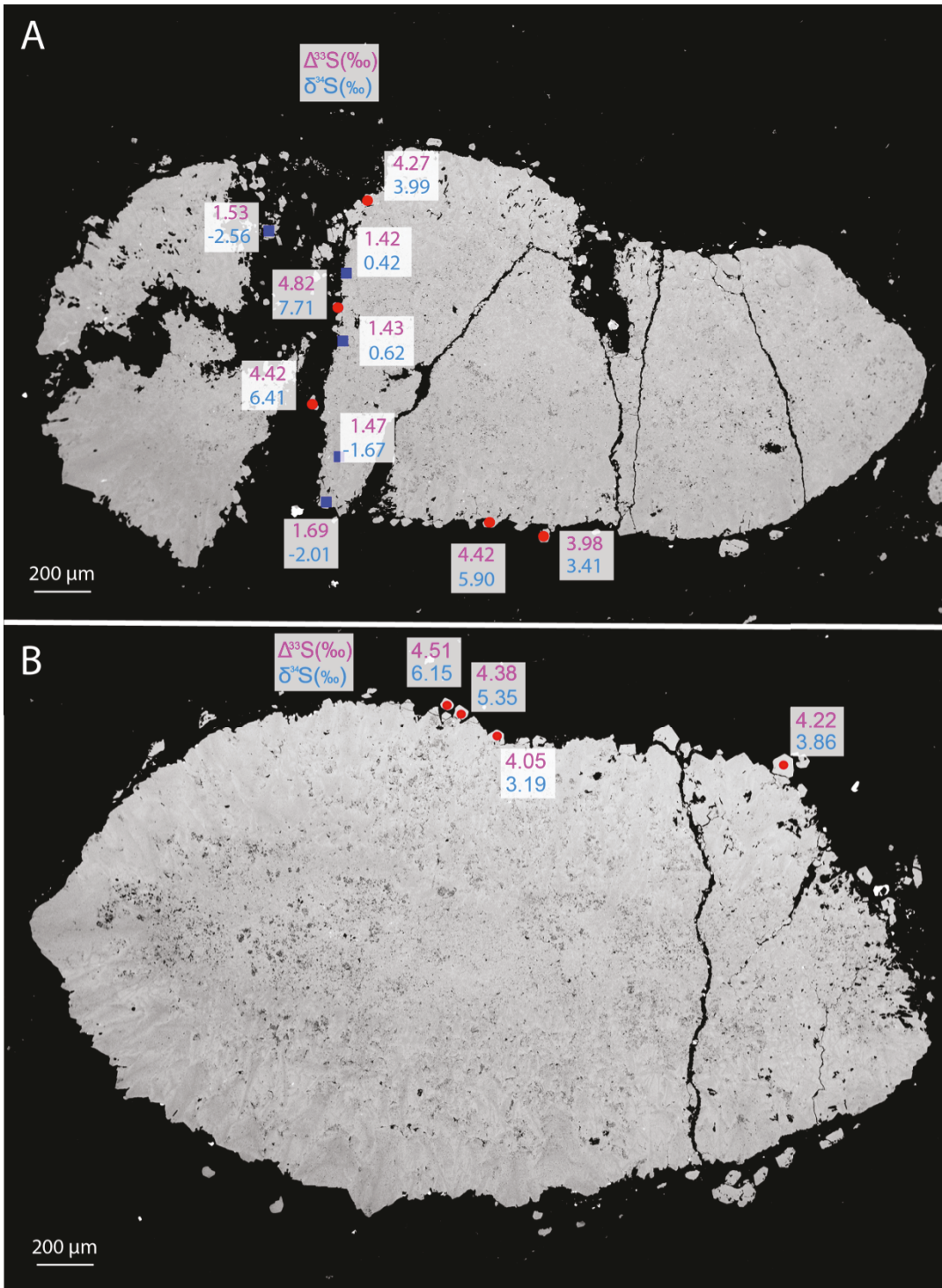


Figure 22. Sulfur isotopic data of subhedral pyrite grains (red circles) and comparison spots (blue squares) in nodules 2 (A) and 3 (B). Pink numbers are $\Delta^{33}\text{S}$ values; blue numbers are $\delta^{34}\text{S}$ values.

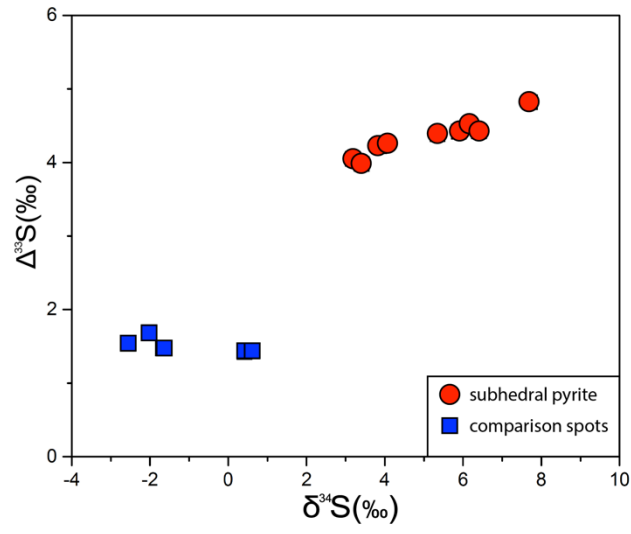


Figure 23. $\Delta^{33}\text{S}$ - $\delta^{34}\text{S}$ diagram of subhedral pyrite grains in quartz veins (red circles) along the rim of nodules 2 and 3, and comparison spots in the rim of Nodule 2 (blue squares). Error bars are all smaller than symbols. See text for detailed discussion.

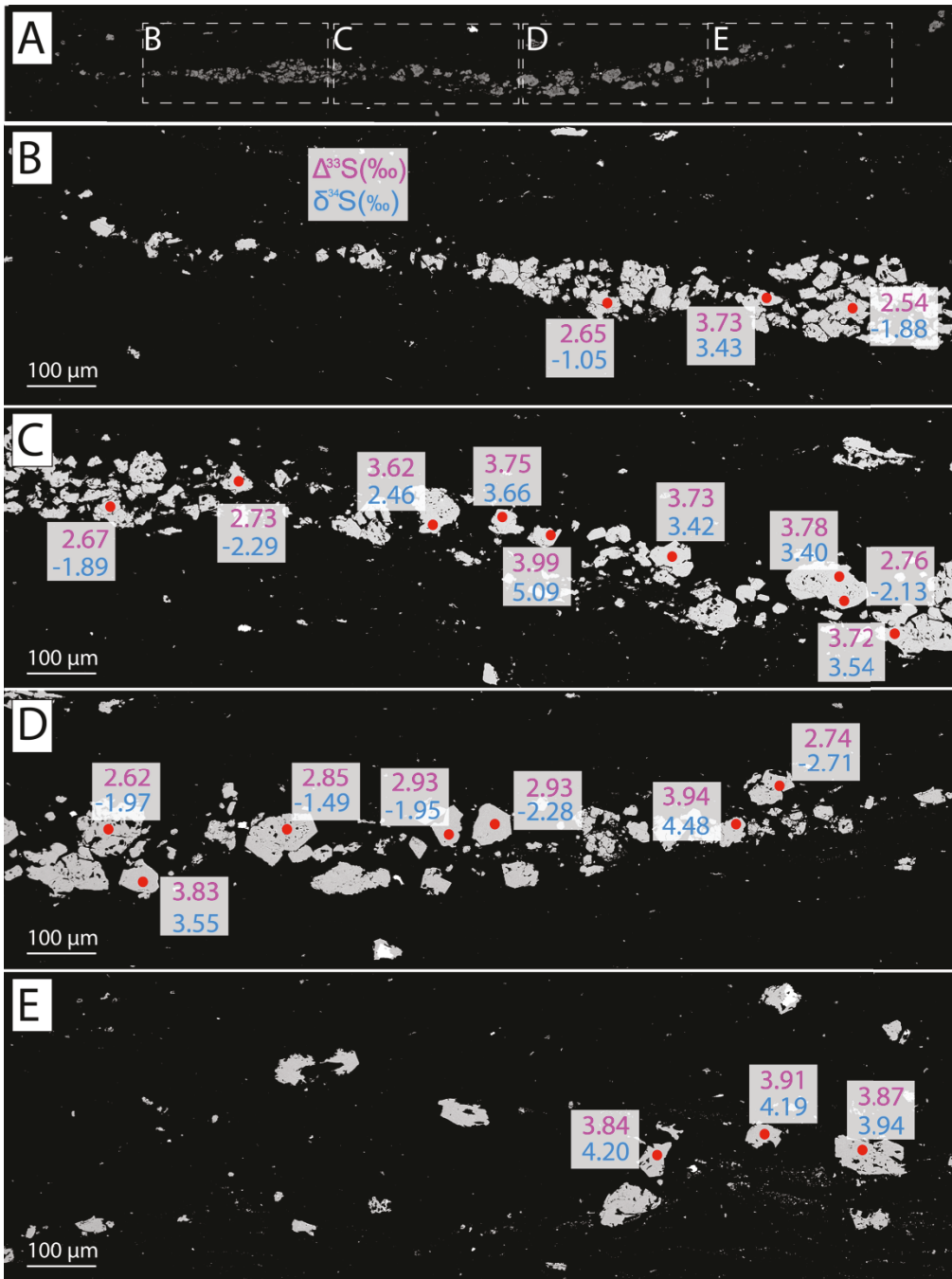


Figure 24. Sulfur isotopic data of lamina pyrite. Panels B-E are enlarged parts of the lamina shown in panel A with $\Delta^{33}\text{S}$ values (in pink) and $\delta^{34}\text{S}$ values (in blue).

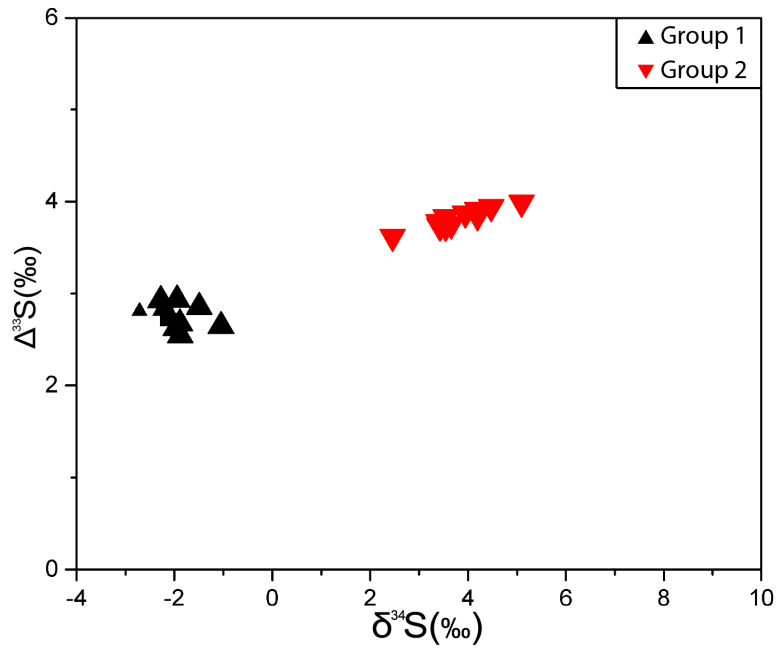


Figure 25. $\Delta^{33}\text{S}$ - $\delta^{34}\text{S}$ diagram shows the bimodal distribution of $\Delta^{33}\text{S}$ and $\delta^{34}\text{S}$ values of pyrite in the lamina (see text for detailed discussion). Error bars are all smaller than symbols.

6. Discussion

6.1. Pyrite morphology and zonation pattern of pyrite nodules

The pyrite nodules studied here are ellipsoidal in shape (Figures 8, 10 and 11), which is usually interpreted as originally being formed during early diagenesis (e.g. Farquhar et al., 2013, Marin-Carbonne et al., 2014, Fischer et al., 2014). As described above, all the studied nodules display a zonation pattern, which is best shown in Nodule 1 (Figures 8, 10 and 11). As a direct expression of the zonation pattern, major and trace elements show strong cross-section variations. For example, in Nodule 1, Zone I has higher Total% than Zone II (Figure 13D), which shows the darkest color and the lowest Total%. The relatively low Total% (~94%, compared with 99.7-100.1% of the standard) in Zone II may be attributed to the existence of mineral or fluid inclusions. Zone III shows rapid increase in Total% from approximately 94% from the contact with Zone II to about 98% to the contact with Zone IV (Figure 13D). Trace-elements concentrations (Ni and Cu) also display different features in different zones. For example, Ni concentrations in Nodule 1 show a sharp decrease from Zone I to Zone II, a steady increase back in Zone III, and a sharp decrease to mostly below detection limit in Zone IV (Figure 13G). Cu concentrations in Nodule 1 show much vaguer zonation pattern than Ni concentrations: in general, zones I-III contain similar Cu (0.04% to 0.06%) with slightly higher values in Zone II, but Zone IV contains undetectable Cu (Figure 13J).

The variations in major and trace elements in nodules 2 and 3 are not as prominent as in Nodule 1. Nodule 2 barely shows cross-section variations in major and trace elements, which may be attributed at least partly to the fact that the analyzed points

are accidentally mainly located in Zone I (Figure 13B). The analyzed points in Nodule 3 are mainly along the boundary between Zone I and Zone II. The zigzag cross-section variation pattern of Total% may imply that the measured points jump back and forth between Zone I and Zone II in this nodule (Figure 13C). There is a slight increase trend in Total% toward the rim of Nodule 3, implying some analyzed points may cover Zone III, which is consistent with what is shown in the BSE image (Figure 13C).

Strong variations of sulfur isotopic compositions across the nodules are also observed, suggesting distinct sulfur isotopic signatures in different zones. For example, in Nodule 1, Zone I has relatively high $\delta^{34}\text{S}$ values (0 to 2.0‰) and relatively low $\Delta^{33}\text{S}$ values (0.5‰ to 2.0‰); compared with Zone I, Zone II has much lower $\delta^{34}\text{S}$ values (~ -1.5‰) but similar $\Delta^{33}\text{S}$ values; Zone III shows a steady decrease in $\delta^{34}\text{S}$ value from 0.7‰ to -2.5‰ coupled with a steady increase in $\Delta^{33}\text{S}$ value from 1.2‰ to 2.2‰; Zone IV has the lowest $\delta^{34}\text{S}$ values (~-2.5‰) and the highest $\Delta^{33}\text{S}$ values (2.1‰ to 2.6‰; Figure 21; see section 6.3 for detailed discussion on sulfur isotopic variations in the nodules). Thus, both the elemental and sulfur isotopic data are consistent with the BSE zonation patterns.

Compared with Nodule 1, nodules 2 and 3 do not have a Zone IV, which could be owing to two possible scenarios: (1) during nodule formation stage, after the growth of Zone III, nodules 2 and 3 were isolated from the pyrite-formation environment and stopped growing while Nodule 1 continued to grow its Zone IV; or (2) nodules 2 and 3 also grew four zones like Nodule 1, but their Zone IV (and even part of Zone III) was dissolved by post-depositional processes (e.g., by metamorphic fluid), leaving only three zones preserved to date. The second scenario is more consistent with the elemental and isotopic data (see discussion below).

Based on the comparison of nodule structure and elemental geochemistry, we suggest that the origin of all three nodules is similar. Among the three nodules, Nodule 1 preserves the most comprehensive growth history. The distinct zonation pattern of the nodules suggests that fluid chemistry and environment were evolving during the formation of these nodules.

6.2. Elemental and sulfur isotopic signatures of metamorphic fluid and metamorphic effects on pyrite nodules

The shale samples from the Joy Lake sequence contain abundant secondary quartz veins, which are clear indication of occurrence of secondary hydrothermal fluids, most likely related to the regional metamorphic event. To assess the influence of the metamorphic fluid on the diagenetic pyrite nodules, we need to first characterize the isotopic and elemental signatures of the metamorphic fluid. For this purpose, we examined the sulfur isotopic compositions and Ni and Cu concentrations of the fine grained (40 to 80 μm) subhedral pyrite disseminated in the quartz veins, which are considered to co-precipitate with quartz from the metamorphic fluid and thus should record the elemental and isotopic signatures of the metamorphic fluid. We further examined the sulfur isotopic compositions and Ni and Cu concentrations of the lamina pyrite grains (co-existing with quartz), which may record some metamorphic fluid information as well.

The subhedral pyrite grains show a strong positive trend on the $\Delta^{33}\text{S}-\delta^{34}\text{S}$ diagram (Figures 26A), which can be explained by a two-endmember mixing model. The first endmember is characterized by sulfur isotopic composition similar to those of the nodule rim, suggesting pyrite nodules contributed sulfur to the secondary subhedral pyrite grains

likely through dissolution. This is consistent with the missing of Zone IV in the nearby nodules. The other endmember, which should be the metamorphic fluid, is characterized by high $\delta^{34}\text{S}$ ($> 7.7\%$) and high $\Delta^{33}\text{S}$ ($> 4.8\%$) values. The subhedral pyrites, which presumably precipitated from the metamorphic fluid, do not show a constant value but more scattered along a mixing trend, indicating the sulfur isotopic compositions of the metamorphic fluid was strongly locally controlled, depending on the relative contribution from local wall-rock pyrite (e.g., the nodules).

Sulfur isotopic data of the lamina pyrite occur as two very distinct groups (Figure 26A). The tightened Group 1 data are almost identical to those of the nodule rims, whereas the Group 2 data are close to those of the subhedral pyrite and similarly show a linear trend (Figure 26A). This suggests that the pyrite in the lamina cannot originate solely from the metamorphic fluid, but more likely a mixture of pre-existing diagenetic pyrite and overgrown pyrite from metamorphic fluid. The linear trend of Group 2 data on the $\Delta^{33}\text{S}$ - $\delta^{34}\text{S}$ diagram can also be explained by a two-endmember mixing model: the endmember with relatively low $\delta^{34}\text{S}$ and $\Delta^{33}\text{S}$ values is consistent with Group 1 pyrite of diagenetic origin; the other endmember, characterized by relatively high $\delta^{34}\text{S}$ ($> 5.1\%$) and $\Delta^{33}\text{S}$ ($> 4.0\%$) values, is presumably metamorphic fluid. Similar to those of the subhedral pyrite, the Group 2 data show a mixing trend rather than a constant value. This can be caused by two possibilities: (1) as the subhedral pyrite indicated, the isotopic signature of local metamorphic fluid is heterogeneous due to varying mass contribution from diagenetic pyrite in wall rocks, and/or (2) the SIMS beam size is too large to be focused on a pure overgrowth zone (if it is less than 15 μm) and thus analytical spots incorporate a mixture of the overgrown pyrite and diagenetic pyrite at various mass ratios.

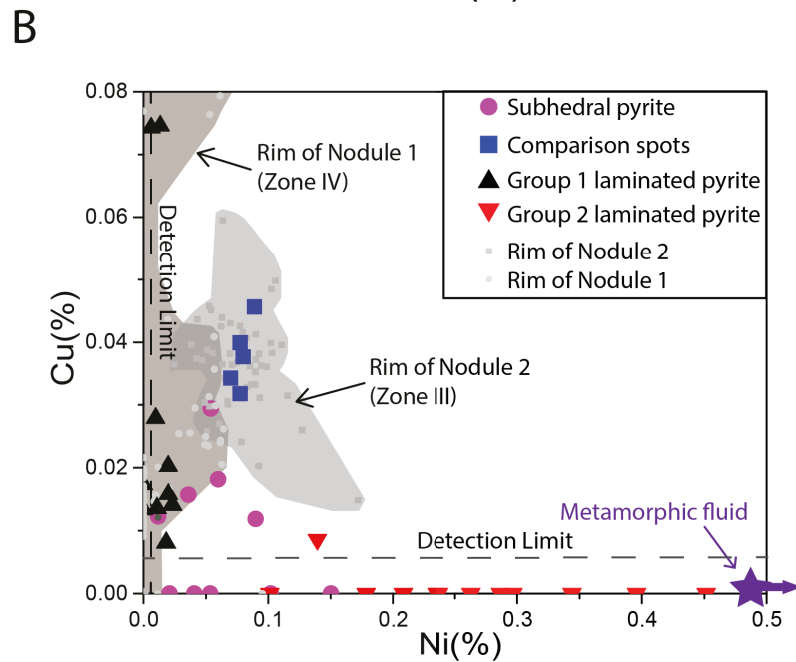
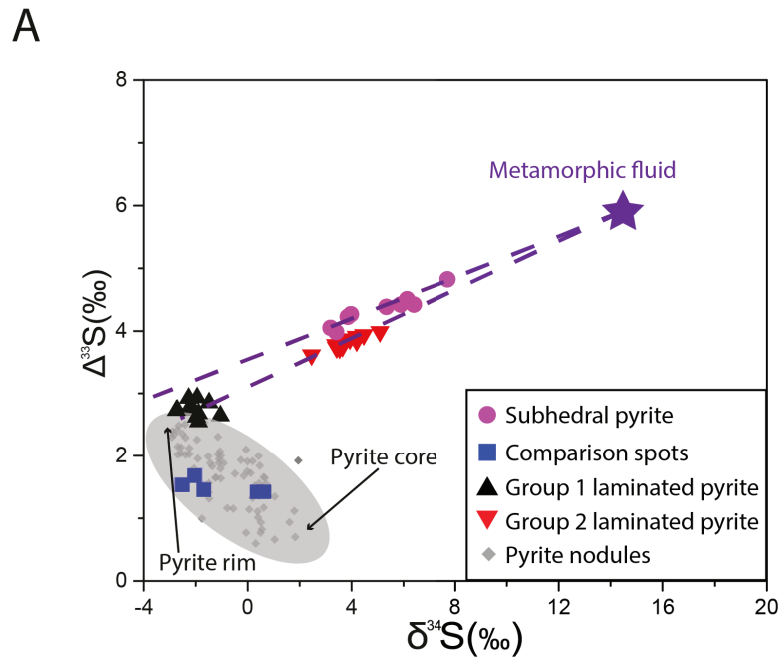


Figure 26. Sulfur isotopic compositions (A) and trace element concentrations (B) of subhedral pyrite, comparison spots and lamina pyrite. See text for detailed explanation.

If we assume that the metamorphic fluid related to the subhedral pyrite and the

Group 2 pyrite in the lamina had the same source, the crossing point of the two mixing line should give the sulfur isotopic signature of the metamorphic fluid, which is 15.2‰ for $\delta^{34}\text{S}$ value and 5.9‰ for $\Delta^{33}\text{S}$ value (Figure 26A). Similar highly positive $\delta^{34}\text{S}$ and $\Delta^{33}\text{S}$ values have been observed in sedimentary rocks older than 2.7 Ga (e.g. Bottomley et al., 1992, Kakegawa et al., 2000, Phillipot et al., 2007, 2012). The sulfide with such high sulfur isotopic ratios can be easily transferred from the rocks to the metamorphic fluid by water-mineral interaction along the fluid flow pathways.

Consistent with sulfur isotope results, Ni and Cu concentrations of subhedral pyrite and Group 2 lamina pyrite can also be explained by mixing between metamorphic fluid and diagenetic pyrite. As shown in Figure 26B, Cu and Ni concentrations of subhedral pyrite grains fall between those of the rim of pyrite Nodule 1 (corresponding to Zone IV) with low Ni% and high Cu% values, and another endmember with high Ni concentration but nearly no Cu, which presumably represents the metamorphic fluid. This mixing model requires significant mass contribution from Zone IV to the subhedral pyrite. This is again consistent with the observation that Zone IV is missing in nodules 2 and 3, probably due to dissolution by the metamorphic fluid. Group 2 pyrite grains in the lamina show very low Cu concentrations (9 out of 10 analyzed spots are below detection limit) but very high Ni concentrations, which suggest that there is little contribution from the Group 1 pyrite (Figure 26B). This is contradictory to the sulfur isotope results, which suggest Group 2 pyrite should have more diagenetic pyrite contribution than subhedral pyrite (Figure 26A). In this case, we believe that the trace-element signatures are better than sulfur isotopic compositions in indicating the relative contribution from the two sources. This is because the spatial resolution of EPMA analysis is much smaller than

that of SIMS analysis ($\sim 1\text{-}2\ \mu\text{m}$ vs. $\sim 15\ \mu\text{m}$). Given the highly heterogeneous distribution of diagenetic and metamorphic pyrite (inferred from both trace elements and sulfur isotopic data; see discussion above) in the lamina, the higher-spatial resolution EPMA analysis has a better chance to pinpoint the two different types of pyrite in the lamina; whereas the relatively lower-spatial resolution SIMS analysis has greater chance to cross over both overgrown pyrite and diagenetic pyrite; the latter, however, may be large enough and can be identified by SIMS analysis as seen by the tight cluster of Group 1 data. Accordingly, the sulfur isotopic data of the Group 2 lamina pyrite may represent a mixture of overgrown pyrite and diagenetic pyrite rather than only overgrown pyrite. This can result in the observation that the sulfur isotopic data of Group 2 pyrite sit closer to those of the diagenetic pyrite. The large variation in Ni concentration of Group 2 pyrite in the lamina may reflect a kinetic assimilation of Ni from the metamorphic fluid in a (semi-) closed system with respect to Ni, possibly due to the disconnection or slow mass exchange between the small amount of metamorphic fluid infiltrated into the small fracture developed along the existing pyrite lamina and the large reservoir of metamorphic fluid along other better developed fractures.

To further evaluate the effect of metamorphism on the sulfur isotope composition of pyrite nodules, we examined several comparison spots in the rim of pyrite Nodule 2 located $\sim 30\ \mu\text{m}$ from the pyrite nodule-quartz boundary and $150\text{-}300\ \mu\text{m}$ from the closest subhedral grains (see Figures 14, 15, 22, 23 26A). Although these rim areas are considered to be most susceptible to the metamorphic alteration, the 5 measurements gave very uniform $\Delta^{33}\text{S}$ values (1.4‰ to 1.7‰) and relatively low $\delta^{34}\text{S}$ values (from -2.6‰ to 0.5‰), which are significantly different from those of subhedral pyrite grains in

the quartz veins and the deduced metamorphic fluid endmember (Figure 26A). This observation suggests that, except for possible dissolution of outer parts of the pyrite nodules, there has been no notable isotopic exchange between the metamorphic fluid and the residual pyrite nodule bodies even at length scales of less than 50 μm . This conclusion is further supported by the correlation between $\Delta^{33}\text{S}$ and $\delta^{34}\text{S}$ values from all the studied pyrite nodule bodies (Figure 26A), which display a negative trend (see next section for explanation) from the cores to the rims of the three pyrite nodules. If there were any isotopic exchange between the metamorphic fluid and residual pyrite nodules, one would expect the $\delta^{34}\text{S}$ and $\Delta^{33}\text{S}$ of the pyrite nodule rims to have been shifted toward the fluid endmember along a positive mixing trend (Figure 26A), which is not observed.

6.3. The 2.7Ga sulfur cycle recorded in pyrite nodules

Because the shift in the sulfur isotope compositions of pyrite nodules by metamorphism is negligible, the multiple sulfur isotopic records in the pyrite nodules can be utilized to infer the sulfur cycle at 2.7 Ga. The three studied nodules are considered to be formed from similar environment, with Nodule 1 recording the most comprehensive growth history. Thus, we put all three isotopic profiles together for the discussion below.

The $\delta^{34}\text{S}$ range of the pyrite nodules is from -2.8‰ to +2.0‰, overlapping previously reported $\delta^{34}\text{S}$ range (-2.3‰ to +11.1‰; Ripley and Nicol, 1981) obtained by bulk analysis of pyrite grains in samples from the same region. Based on the negative $\delta^{34}\text{S}$ values, Ripley and Nicol (1981) proposed that sulfate-reducing bacteria were mainly responsible for the formation of these pyrite grains. However, our *in-situ* high-resolution analysis shows that all pyrite nodules have positive $\Delta^{33}\text{S}$ values, which indisputably indicate that elemental sulfur was an important sulfur source in the Joy Lake pyrite

nodules and the contribution of sulfate was overestimated in previous studies. In addition, the pyrite nodules show a negative $\Delta^{33}\text{S}$ - $\delta^{34}\text{S}$ trend (slope = -0.28; Figure 27) with increase in $\Delta^{33}\text{S}$ value and decrease in $\delta^{34}\text{S}$ value from the cores to the rims. This trend indicates progressively enhanced addition of elemental sulfur-derived material (with a negative $\delta^{34}\text{S}$ value less than -3‰ and $\Delta^{33}\text{S}$ value larger than 3‰) into a sulfate-derived material (with $\delta^{34}\text{S}$ values of 4-8‰ and typical seawater $\Delta^{33}\text{S}$ value of -1‰ to -2‰) during the growth of the nodules (Figure 27). The sulfur sources and possibly associated biological processes during the formation of pyrite nodules are further discussed below under the context of the Archean sulfur cycle.

Firstly, our data are very difficult to be explained by the results of >220 nm SO_2 photolysis, which produces sulfate with negative $\delta^{34}\text{S}$ and $\Delta^{33}\text{S}$ values and elemental sulfur with positive $\delta^{34}\text{S}$ and $\Delta^{33}\text{S}$ values (Figure 27A). This is because the >220 nm SO_2 photolysis would give $\delta^{34}\text{S}$ value larger than 20‰ for elemental sulfur to reach a $\Delta^{33}\text{S}$ value of larger than 2.5‰ and negative $\delta^{34}\text{S}$ value of -6‰ for sulfate with $\Delta^{33}\text{S}$ value of -1‰ (Figure 27A); these $\delta^{34}\text{S}$ values, particularly the very positive $\delta^{34}\text{S}$ values of elemental sulfur, are difficult to shift to a value of less than -3‰ with any mechanism proposed to have operated in the 2.7 Ga oceans. Similar difficulties also apply if we use Ono's model (Ono et al., 2003) or ARA (Figure 27A) to explain our data. If we assume that the two sulfur endmembers were derived from sulfate and elemental sulfur reservoirs in Ono's endmembers or the ARA (Figure 27), a strong ^{34}S -discriminating process has to be invoked besides the commonly seen BSR process. Previous studies have suggested two mechanisms that could produce sulfide with negative $\delta^{34}\text{S}$ values from elemental sulfur: (1) oxidation of elemental sulfur (S_8) into sulfate followed by sulfate reduction

(Kaufman et al., 2007); and (2) bacterial elemental sulfur disproportionation (BESD, Philippot et al., 2007). The first mechanism was proposed by Kaufman et al. (2007) from the study of 2.5Ga Mount McRae shales in Hamersley Basin in northwest Australia, which have positive $\Delta^{33}\text{S}$ and negative $\delta^{34}\text{S}$ values. The oxidation of elemental sulfur requires an oxic environment, which is likely the case for the 2.5 Ga Mount McRae shale (Kaufman et al., 2007) as evidenced by several other geochemical proxies, including trace elements and C and N isotopes (Anbar et al., 2007; Garvin et al., 2009). However, this mechanism cannot be applied to our 2.7 Ga samples because of a lack of evidence for the existence of an oxic environment at that time. The second mechanism, BESD, does not require an oxic environment. The sulfide product from BESD can be depleted in ^{34}S by up to 8‰ (Canfield and Thamdrup, 1994; Canfield and Raiswell, 1999), which can account for the sulfur endmember with $\delta^{34}\text{S} < -3\text{‰}$ and $\Delta^{33}\text{S} > +2.5\text{‰}$ (Figure 27B). However, besides the requirement of a more complicated microbial ecosystem, this model ignores the sulfate that is co-produced by BESD. Based on mass balance, with the production of every 3 molar sulfides, BESD should also produce 1 molar sulfate with ^{34}S -enrichment for a magnitude of 3 times more than the magnitude of ^{34}S -depletion in the sulfide product. But this sulfate has to be arbitrarily discarded in the model; otherwise it would result in a $\Delta^{33}\text{S}$ - $\delta^{34}\text{S}$ distribution pattern different from the observed one.

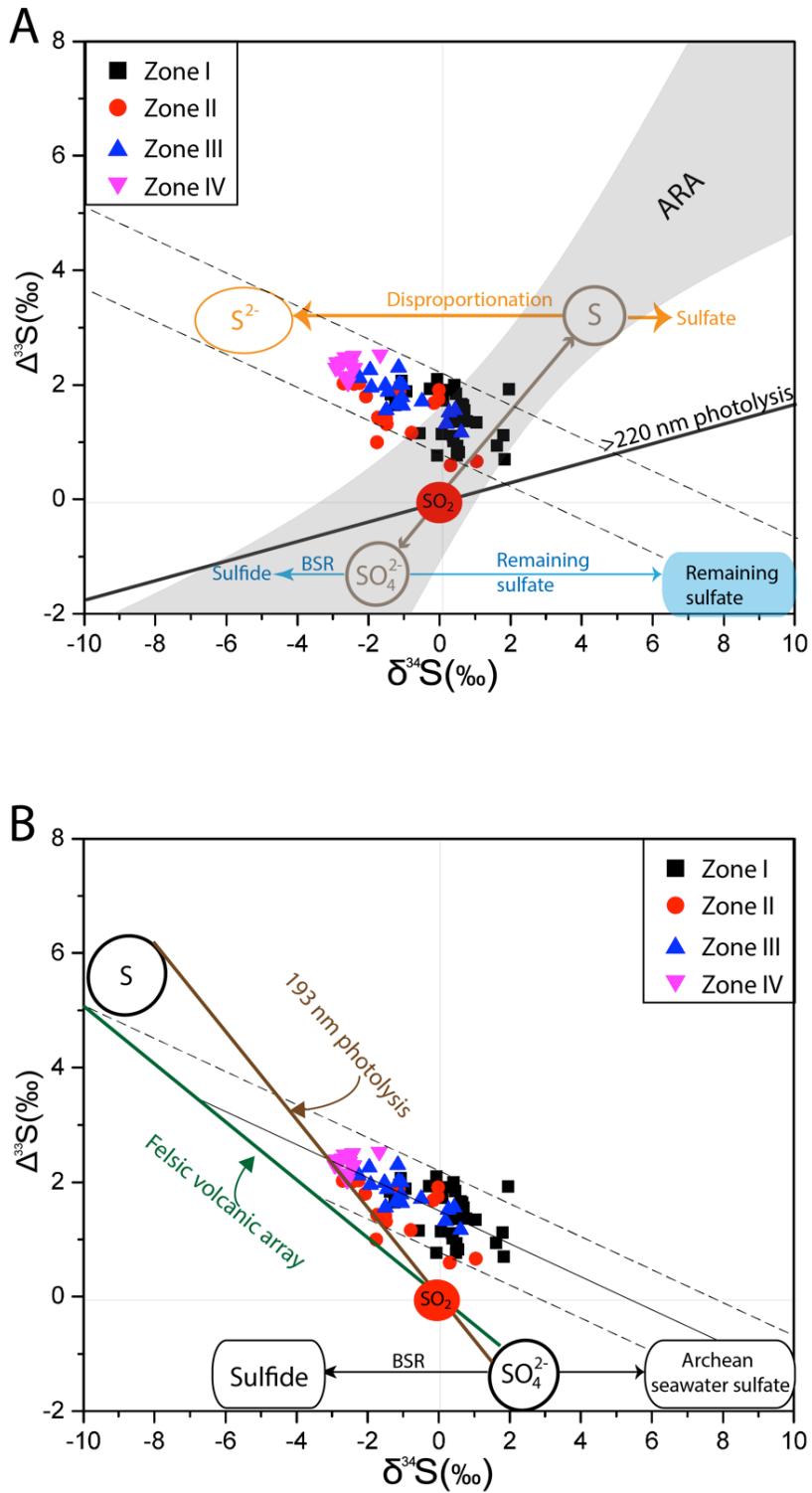


Figure 27. Sulfur isotope mixing model for pyrite nodules and comparison with (A) the Archean Reference Array (Thomassot et al., 2015) and the Ono's conceptual model (Ono et al., 2003), and (B) the 193 nm photolytic results (Farquhar et al., 2001) and the "felsic volcanic array" (Pilippot et al., 2012). See text for detailed discussion.

The best way to explain our data is to link the sulfate and elemental sulfur sources to the rarely observed 193 nm photolysis or the felsic volcanic array, both of which display similar negative trends on the $\Delta^{33}\text{S}-\delta^{34}\text{S}$ diagram (Figure 27B). Compared with the results of the 193 nm photolytic array (Farquhar et al., 2001) and the felsic volcanic array (Philippot et al., 2012), our data display gentler $\Delta^{33}\text{S}/\delta^{34}\text{S}$ slope (-0.28) and sit slightly above these two arrays (Figure 27B). These features can be easily explained by mixing of elemental sulfur from these arrays with a modified sulfate reservoir that has slightly higher $\delta^{34}\text{S}$ values, which could be derived by low-extent removal of the sulfate via BSR (Figure 27B). In this scenario, one does not need to invoke a strongly ^{34}S -discriminating pathway for the incorporation of elemental sulfur into pyrite. Therefore, the microbial system (if there was any) during diagenesis should be dominated by the non- ^{34}S -discriminating elemental sulfur-reducing bacteria.

To date, no efficient index has been suggested to distinguish between the 193 nm photolysis array and the felsic volcanic array. However, if there is any difference in the photolytic mechanism between these two, we prefer that the elemental sulfur source in our case was genetically closer to the case of felsic volcanic array because 2.7Ga is well known to be a major time for continent growth (e.g., Condie et al., 2009) and extensive volcanic rocks have also been observed in the area (Figure 5).

It is worth noting here that, despite the overwhelming positive $\Delta^{33}\text{S}$ values, which indicate the major role of elemental sulfur, and the complicated origin (photochemical, biological, etc.) of the elemental sulfur-derived material recorded in our pyrite nodule samples, our data do not completely exclude the occurrence of sulfate-reducing bacteria during the formation of the pyrite nodules. In fact, the mixing trend on the $\Delta^{33}\text{S}-\delta^{34}\text{S}$

diagram does point to a sulfate-derived endmember, which composes 55% to 65% of the sulfur in the nodule cores but decreased to approximately 0% to 35% in the nodule rims if we assume the elemental sulfur were derived from the “felsic volcanic array”, or about 45% to 50% in the nodule cores and 0 to 10% in the nodule rims if we assume the elemental sulfur was derived from the 193 nm photolytic array (Figure 27B). This suggests that the sulfate-reducing bacteria were an important component in the microbial ecosystem, at least in the early stage of the pyrite formation. The steady increase in $\Delta^{33}\text{S}$ value from the cores to the rims of pyrite nodules indicates that the relative BSR contribution progressively diminished during the time period of pyrite growth. This change may reflect either suppression of sulfate-reducing bacteria, which could be due to decreasing seawater sulfate availability following gradual burial isolation of the system from seawater, or increase in activity of elemental sulfur-reducing bacteria, or both.

7. Conclusion

To examine the effect of metamorphism of the sulfur isotope composition of sedimentary pyrite and unravel the primary signature recorded in diagenetic pyrite, we carried out *in-situ* SIMS analysis for multiple sulfur isotopes and EPMA analysis for major and trace elements on pyrite nodules and secondary pyrite grains associated with metamorphic fluid-related quartz veins in the 2.7 Ga shales from the Joy Lake Sequence, Superior Province. The compositions of secondary pyrite grains suggest the metamorphic fluid contained little Cu but high Ni and had highly positive $\Delta^{33}\text{S}$ and $\delta^{34}\text{S}$ values, likely derived from leaching of sulfur-bearing minerals in previous Archean supracrustal rocks. However, none of these fluid features were incorporated in the diagenetic pyrite nodules, indicating little isotopic shift on the diagenetic pyrite nodules.

The pyrite nodules show a negative trend on the $\Delta^{33}\text{S}$ - $\delta^{34}\text{S}$ diagram with decrease in $\delta^{34}\text{S}$ and increase in $\Delta^{33}\text{S}$ over the growth of the pyrite nodules from the core to the rim. This negative trend can be explained by a mixing of sulfur derived from both sulfate and elemental sulfur produced from a SO_2 photolytic reaction different to the one commonly seen in most of the Archean geological record. The SO_2 photolytic reaction is close to either the experimental results of SO_2 photolysis at 193 nm or the “felsic volcanic array” generated under condition of intensive volcanic emission during volcanically active period. The modeling implies that the microbial system during the formation of the pyrite nodules shifted from one dominated by sulfate-reducing bacteria at the early stage to one dominated by elemental sulfur-reducing bacteria at the late stage of the pyrite formation.

Bibliography

- Anbar, A.D., Duan, Y., Lyons, T.W., Arnold, G.L., Kendall, B., Creaser, R.A., Kaufman, A.J., Gordon, G.W., Scott, C., Garvin, J., 2007. A whiff of oxygen before the great oxidation event? *Science* 317, 1903-1906.
- Bao, H., Rumble, D., Lowe, D.R., 2007. The five stable isotope compositions of Fig Tree barites: Implications on sulfur cycle in ca. 3.2 Ga oceans. *Geochimica et Cosmochimica Acta* 71, 4868-4879.
- Bauer, R.L., 1985. Correlation of early recumbent and younger upright folding across the boundary between an Archean gneiss belt and greenstone terrane, northeastern Minnesota. *Geology* 13, 657-660.
- Bauer, R.L., 1986. Multiple folding and pluton emplacement in Archean migmatites of the southern Vermilion granitic complex, northeastern Minnesota. *Canadian Journal of Earth Sciences* 23, 1753-1764.
- Benning, L.G., Wilkin, R.T., Barnes, H., 2000. Reaction pathways in the Fe-S system below 100 C. *Chemical Geology* 167, 25-51.
- Benninghoven, A., Rudenauer, F., Werner, H.W., 1987. Secondary ion mass spectrometry: basic concepts, instrumental aspects, applications and trends.
- Berkley, J., Himmelberg, G., 1978. Cumulus mineralogy and petrology of the Deer Lake complex, Itasca County, Minnesota. Minnesota Geological Survey Report of Investigations, 18.
- Berner, R.A., 1970. Sedimentary pyrite formation. *American Journal of Science* 268, 1-23.
- Boerboom, T.J., Zartman, R.E., 1993. Geology, geochemistry, and geochronology of the central Giants Range batholith, northeastern Minnesota. *Canadian Journal of Earth Sciences* 30, 2510-2522.
- Bontognali, T.R., Sessions, A.L., Allwood, A.C., Fischer, W.W., Grotzinger, J.P., Summons, R.E., Eiler, J.M., 2012. Sulfur isotopes of organic matter preserved in 3.45-billion-year-old stromatolites reveal microbial metabolism. *Proceedings of the National Academy of Sciences* 109, 15146-15151.
- Bottomley, D. J., Veizer, J., Nielsen, H., & Moczydlowska, M., 1992. Isotopic composition of disseminated sulfur in Precambrian sedimentary rocks. *Geochimica et Cosmochimica Acta*, 56(8), 3311-3322.

- Buchan, K.L., Halls, H.C., Mortensen, J.K., 1996. Paleomagnetism, U-Pb geochronology, and geochemistry of Marathon dykes, Superior Province, and comparison with the Fort Frances swarm. *Canadian Journal of Earth Sciences* 33, 1583-1595.
- Butler, I.B., Böttcher, M.E., Rickard, D., Oldroyd, A., 2004. Sulfur isotope partitioning during experimental formation of pyrite via the polysulfide and hydrogen sulfide pathways: implications for the interpretation of sedimentary and hydrothermal pyrite isotope records. *Earth and Planetary Science Letters* 228, 495-509.
- Canfield, D.E., 2001. Isotope fractionation by natural populations of sulfate-reducing bacteria. *Geochimica et Cosmochimica Acta* 65, 1117-1124.
- Canfield, D.E., Raiswell, R., 1991. Pyrite formation and fossil preservation. *Taphonomy: releasing the data locked in the fossil record* 9, 337-387.
- Canfield, D.E., Raiswell, R., 1999. The evolution of the sulfur cycle. *American Journal of Science* 299, 697-723.
- Canfield, D.E., Thamdrup, B., 1994. The production of ³⁴S-depleted sulfide during bacterial disproportionation of elemental sulfur. *Science* 266, 1973-1975.
- Canfield, D.E., Thamdrup, B., Fleischer, S., 1998. Isotope fractionation and sulfur metabolism by pure and enrichment cultures of elemental sulfur - disproportionating bacteria. *Limnology and Oceanography* 43, 253-264.
- Card, K., 1990. A review of the Superior Province of the Canadian Shield, a product of Archean accretion. *Precambrian Research* 48, 99-156.
- Condie, K.C., 1998. Episodic continental growth and supercontinents: a mantle avalanche connection? *Earth and Planetary Science Letters* 163, 97-108.
- Condie, K.C., Belousova, E., Griffin, W., Sircombe, K.N., 2009. Granitoid events in space and time: constraints from igneous and detrital zircon age spectra. *Gondwana Research* 15, 228-242.
- Corfu, F., Stott, G., 1998. Shebandowan greenstone belt, western Superior Province: U-Pb ages, tectonic implications, and correlations. *Geological Society of America Bulletin* 110, 1467-1484.
- Deditius, A.P., Utsunomiya, S., Renock, D., Ewing, R.C., Ramana, C.V., Becker, U., Kesler, S.E., 2008. A proposed new type of arsenian pyrite: composition, nanostructure and geological significance. *Geochimica et Cosmochimica Acta* 72, 2919-2933.
- Ding, T., Valkiers, S., Kipphardt, H., De Bievre, P., Taylor, P., Gonfiantini, R., Krouse,

- R., 2001. Calibrated sulfur isotope abundance ratios of three IAEA sulfur isotope reference materials and V-CDT with a reassessment of the atomic weight of sulfur. *Geochimica et Cosmochimica Acta* 65, 2433-2437.
- Domagal-Goldman, S.D., Kasting, J.F., Johnston, D.T., Farquhar, J., 2008. Organic haze, glaciations and multiple sulfur isotopes in the Mid-Archean Era. *Earth and Planetary Science Letters* 269, 29-40.
- Farquhar, J., Bao, H., Thiemens, M., 2000. Atmospheric influence of Earth's earliest sulfur cycle. *Science* 289, 756-758.
- Farquhar, J., Cliff, J., Zerkle, A.L., Kamyshny, A., Poulton, S.W., Claire, M., Adams, D., Harms, B., 2013. Pathways for Neoproterozoic pyrite formation constrained by mass-independent sulfur isotopes. *Proceedings of the National Academy of Sciences* 110, 17638-17643.
- Farquhar, J., Johnston, D.T., Wing, B.A., Habicht, K.S., Canfield, D.E., Airieau, S., Thiemens, M.H., 2003. Multiple sulphur isotopic interpretations of biosynthetic pathways: implications for biological signatures in the sulphur isotope record. *Geobiology* 1, 27-36.
- Farquhar, J., Peters, M., Johnston, D.T., Strauss, H., Masterson, A., Wiechert, U., Kaufman, A.J., 2007. Isotopic evidence for Mesoarchaeoan anoxia and changing atmospheric sulphur chemistry. *Nature* 449, 706-709.
- Farquhar, J., Savarino, J., Airieau, S., Thiemens, M.H., 2001. Observation of wavelength - sensitive mass - independent sulfur isotope effects during SO₂ photolysis: Implications for the early atmosphere. *Journal of Geophysical Research: Planets* (1991–2012) 106, 32829-32839.
- Farquhar, J., Wing, B.A., 2003. Multiple sulfur isotopes and the evolution of the atmosphere. *Earth and Planetary Science Letters* 213, 1-13.
- Farquhar, J., Wu, N., Canfield, D.E., Oduro, H., 2010. Connections between sulfur cycle evolution, sulfur isotopes, sediments, and base metal sulfide deposits. *Economic Geology* 105, 509-533.
- Fischer, W.W., Fike, D.A., Johnson, J.E., Raub, T.D., Guan, Y., Kirschvink, J.L., Eiler, J.M., 2014. SQUID-SIMS is a useful approach to uncover primary signals in the Archean sulfur cycle. *Proceedings of the National Academy of Sciences* 111, 5468-5473.
- Fleet, M.E., Mumin, A.H., 1997. Gold-bearing arsenian pyrite and marcasite and arsenopyrite from Carlin Trend gold deposits and laboratory synthesis. *American Mineralogist* 82, 182-193.

- Garvin, J., Buick, R., Anbar, A.D., Arnold, G.L., Kaufman, A.J., 2009. Isotopic evidence for an aerobic nitrogen cycle in the latest Archean. *Science* 323, 1045-1048.
- Goldhaber, M., Kaplan, I., 1974. The sulfur cycle: 569-655. *The Sea* 5.
- Gregory, D.D., Large, R.R., Halpin, J.A., Steadman, J.A., Hickman, A.H., Ireland, T.R., Holden, P., 2015. The chemical conditions of the late Archean Hamersley basin inferred from whole rock and pyrite geochemistry with $\Delta 33\text{ S}$ and $\delta 34\text{ S}$ isotope analysis. *Geochimica et Cosmochimica Acta* 149, 223-250.
- Grosch, E.G., McLoughlin, N., 2013. Paleoarchean sulfur cycle and biogeochemical surface conditions on the early Earth, Barberton, South Africa. *Earth and Planetary Science Letters* 377, 142-154.
- Guo, Q., Strauss, H., Kaufman, A.J., Schröder, S., Gutzmer, J., Wing, B., Baker, M.A., Bekker, A., Jin, Q., Kim, S.-T., 2009. Reconstructing Earth's surface oxidation across the Archean-Proterozoic transition. *Geology* 37, 399-402.
- Jamieson, J., Wing, B., Farquhar, J., Hannington, M., 2013. Neoarchean seawater sulphate concentrations from sulphur isotopes in massive sulphide ore. *Nature Geoscience* 6, 61-64.
- Jirsa, M., Southwick, D., Boerboom, T., 1992. Structural evolution of Archean rocks in the western Wawa subprovince, Minnesota: refolding of precleavage nappes during D2 transpression. *Canadian Journal of Earth Sciences* 29, 2146-2155.
- Jirsa, M.A., 1990. M-068 Bedrock geologic map of northeastern Itasca County, Minnesota.
- Johnston, D.T., 2011. Multiple sulfur isotopes and the evolution of Earth's surface sulfur cycle. *Earth-Science Reviews* 106, 161-183.
- Kakegawa, T., Kasahara, Y., Hayashi, K. I., & Ohmoto, H., 2000. Sulfur and carbon isotope analyses of the 2.7 Ga Jeerinah Formation, Fortescue Group, Australia. *Geochemical Journal*, 34(2), 121-133.
- Kamber, B., Whitehouse, M., 2007. Micro - scale sulphur isotope evidence for sulphur cycling in the late Archean shallow ocean. *Geobiology* 5, 5-17.
- Kamineni, D.C., 1983. Sulfur-isotope geochemistry of fracture-filling gypsum in an Archean granite near Atikokan, Ontario, Canada. *Chemical Geology* 39, 263-272.
- Kaufman, A.J., Johnston, D.T., Farquhar, J., Masterson, A.L., Lyons, T.W., Bates, S., Anbar, A.D., Arnold, G.L., Garvin, J., Buick, R., 2007. Late Archean biospheric oxygenation and atmospheric evolution. *Science* 317, 1900-1903.

- Kurzweil, F., Claire, M., Thomazo, C., Peters, M., Hannington, M., Strauss, H., 2013. Atmospheric sulfur rearrangement 2.7 billion years ago: Evidence for oxygenic photosynthesis. *Earth and Planetary Science Letters* 366, 17-26.
- Love, L., Amstutz, G., 1966. Review of microscopic pyrite. *Fortschr. Mineral* 43, 273-309.
- Luther III, G.W., 1991. Sulfur and iodine speciation in the water column of the Black Sea, *Black Sea Oceanography*. Springer, pp. 187-204.
- Lyons, T.W., 1997. Sulfur isotopic trends and pathways of iron sulfide formation in upper Holocene sediments of the anoxic Black Sea. *Geochimica et Cosmochimica Acta* 61, 3367-3382.
- Marin-Carbonne, J., Rollion-Bard, C., Bekker, A., Rouxel, O., Agangi, A., Cavalazzi, B., Wohlgemuth-Ueberwasser, C.C., Hofmann, A., McKeegan, K.D., 2014. Coupled Fe and S isotope variations in pyrite nodules from Archean shale. *Earth and Planetary Science Letters* 392, 67-79.
- McKibben, M., Rye, R., Eldridge, C., Bethke, P., 1994. Sulfur isotope geochemistry of the Creede Formation and implications for hydrothermal vein mineralization, *Geol. Soc. Amer. Abstr.*, pp. A-399.
- Mojzsis, S., Coath, C., Greenwood, J., McKeegan, K., Harrison, T., 2003. Mass-independent isotope effects in Archean (2.5 to 3.8 Ga) sedimentary sulfides determined by ion microprobe analysis. *Geochimica et Cosmochimica Acta* 67, 1635-1658.
- Morse, J.W., Millero, F.J., Cornwell, J.C., Rickard, D., 1987. The chemistry of the hydrogen sulfide and iron sulfide systems in natural waters. *Earth-Science Reviews* 24, 1-42.
- Oduro, H., Harms, B., Sintim, H.O., Kaufman, A.J., Cody, G., Farquhar, J., 2011. Evidence of magnetic isotope effects during thermochemical sulfate reduction. *Proceedings of the National Academy of Sciences* 108, 17635-17638.
- Ono, S., Beukes, N.J., Rumble, D., 2009a. Origin of two distinct multiple-sulfur isotope compositions of pyrite in the 2.5 Ga Klein Naute Formation, Griqualand West Basin, South Africa. *Precambrian Research* 169, 48-57.
- Ono, S., Eigenbrode, J.L., Pavlov, A.A., Kharecha, P., Rumble III, D., Kasting, J.F., Freeman, K.H., 2003. New insights into Archean sulfur cycle from mass-independent sulfur isotope records from the Hamersley Basin, Australia. *Earth and Planetary Science Letters* 213, 15-30.
- Ono, S., Kaufman, A.J., Farquhar, J., Sumner, D.Y., Beukes, N.J., 2009b. Lithofacies

- control on multiple-sulfur isotope records and Neoproterozoic sulfur cycles. *Precambrian Research* 169, 58-67.
- Ono, S., Wing, B., Johnston, D., Farquhar, J., Rumble, D., 2006. Mass-dependent fractionation of quadruple stable sulfur isotope system as a new tracer of sulfur biogeochemical cycles. *Geochimica et Cosmochimica Acta* 70, 2238-2252.
- Passier, H.F., Middelburg, J.J., de Lange, G.J., Böttcher, M.E., 1997. Pyrite contents, microtextures, and sulfur isotopes in relation to formation of the youngest eastern Mediterranean sapropel. *Geology* 25, 519-522.
- Pavlov, A., Kasting, J., 2002. Mass-independent fractionation of sulfur isotopes in Archean sediments: strong evidence for an anoxic Archean atmosphere. *Astrobiology* 2, 27-41.
- Peevler, J., Fayek, M., Misra, K.C., Riciputi, L.R., 2003. Sulfur isotope microanalysis of sphalerite by SIMS: constraints on the genesis of Mississippi valley-type mineralization, from the Mascot-Jefferson City district, East Tennessee. *Journal of Geochemical Exploration* 80, 277-296.
- Percival, J., Sanborn-Barrie, M., Skulski, T., Stott, G., Helmstaedt, H., White, D., 2006. Tectonic evolution of the western Superior Province from NATMAP and Lithoprobe studies. *Canadian Journal of Earth Sciences* 43, 1085-1117.
- Philippot, P., Van Zuilen, M., Lepot, K., Thomazo, C., Farquhar, J., Van Kranendonk, M.J., 2007. Early Archaean microorganisms preferred elemental sulfur, not sulfate. *Science* 317, 1534-1537.
- Philippot, P., van Zuilen, M., Rollion-Bard, C., 2012. Variations in atmospheric sulphur chemistry on early Earth linked to volcanic activity. *Nature Geoscience* 5, 668-674.
- Raiswell, R., 1982. Pyrite texture, isotopic composition and the availability of iron. *American Journal of Science* 282, 1244-1263.
- Raiswell, R., 1997. A geochemical framework for the application of stable sulphur isotopes to fossil pyritization. *Journal of the Geological Society* 154, 343-356.
- Raiswell, R., Berner, R.A., 1985. Pyrite formation in euxinic and semi-euxinic sediments. *American Journal of Science* 285, 710-724.
- Reich, M., Deditius, A., Chryssoulis, S., Li, J.-W., Ma, C.-Q., Parada, M.A., Barra, F., Mittermayr, F., 2013. Pyrite as a record of hydrothermal fluid evolution in a porphyry copper system: A SIMS/EPMA trace element study. *Geochimica et Cosmochimica Acta* 104, 42-62.
- Rickard, D., 1997. Kinetics of pyrite formation by the H₂S oxidation of iron (II)

monosulfide in aqueous solutions between 25 and 125 C: the rate equation. *Geochimica et Cosmochimica Acta* 61, 115-134.

Rickard, D., 2012. *Sulfidic sediments and sedimentary rocks*. Newnes.

Rickard, D., Luther, G.W., 1997. Kinetics of pyrite formation by the H₂S oxidation of iron (II) monosulfide in aqueous solutions between 25 and 125 C: the mechanism. *Geochimica et Cosmochimica Acta* 61, 135-147.

Rickard, D.T., 1975. Kinetics and mechanism of pyrite formation at low temperatures. *American Journal of Science* 275, 636-652.

Ripley, E., 1983. Sulfide mineralogy and sulfur isotope geochemistry of layered sills in the Deer Lake Complex, Minnesota. *Mineralium Deposita* 18, 3-15.

Ripley, E.M., 1979. Sulfide petrology of basal chilled margins in layered sills of the Archean Deer Lake Complex, Minnesota. *Contributions to Mineralogy and Petrology* 69, 345-354.

Ripley, E.M., Nicol, D.L., 1981. Sulfur isotopic studies of Archean slate and graywacke from northern Minnesota: evidence for the existence of sulfate reducing bacteria. *Geochimica et Cosmochimica Acta* 45, 839-846.

Ripley, E.M., Rao, B., Berkley, J.L., 1982. Mineralogical and chemical variations within layered sills of the Deer Lake Complex, Minnesota. *Contributions to Mineralogy and Petrology* 80, 230-239.

Roberts, A.P., Turner, G.M., 1993. Diagenetic formation of ferrimagnetic iron sulphide minerals in rapidly deposited marine sediments, South Island, New Zealand. *Earth and Planetary Science Letters* 115, 257-273.

Roerdink, D.L., Mason, P.R., Farquhar, J., Reimer, T., 2012. Multiple sulfur isotopes in Paleoproterozoic barites identify an important role for microbial sulfate reduction in the early marine environment. *Earth and Planetary Science Letters* 331, 177-186.

Schoonen, M., Barnes, H., 1991. Reactions forming pyrite and marcasite from solution: II. Via FeS precursors below 100 C. *Geochimica et Cosmochimica Acta* 55, 1505-1514.

Severson, M., Jirsa, M., 2006. M-165 Bedrock geology of the Deer Lake Complex, Itasca County, Minnesota.

Shen, Y., Farquhar, J., Masterson, A., Kaufman, A.J., Buick, R., 2009. Evaluating the role of microbial sulfate reduction in the early Archean using quadruple isotope systematics. *Earth and Planetary Science Letters* 279, 383-391.

- Sim, M.S., Bosak, T., Ono, S., 2011. Large sulfur isotope fractionation does not require disproportionation. *Science* 333, 74-77.
- Smith, J., 2000. Isotopic fractionations accompanying sulfur hydrolysis. *Geochemical Journal* 34, 95-99.
- Southwick, D., Day, W., 1983. Geology and petrology of Proterozoic mafic dikes, north-central Minnesota and western Ontario. *Canadian Journal of Earth Sciences* 20, 622-638.
- Suits, N.S., Wilkin, R.T., 1998. Pyrite formation in the water column and sediments of a meromictic lake. *Geology* 26, 1099-1102.
- Sweeney, R., Kaplan, I., 1973. Pyrite framboid formation; laboratory synthesis and marine sediments. *Economic Geology* 68, 618-634.
- Thomassot, E., Cartigny, P., Harris, J., Lorand, J., Rollion-Bard, C., Chaussidon, M., 2009. Metasomatic diamond growth: A multi-isotope study (13 C, 15 N, 33 S, 34 S) of sulphide inclusions and their host diamonds from Jwaneng (Botswana). *Earth and Planetary Science Letters* 282, 79-90.
- Thomassot, E., O'Neil, J., Francis, D., Cartigny, P., Wing, B.A., 2015. Atmospheric record in the Hadean Eon from multiple sulfur isotope measurements in Nuvvuagittuq Greenstone Belt (Nunavik, Quebec). *Proceedings of the National Academy of Sciences* 112, 707-712.
- Thomazo, C., Ader, M., Farquhar, J., Philippot, P., 2009a. Methanotrophs regulated atmospheric sulfur isotope anomalies during the Mesoarchean (Tumbiana Formation, Western Australia). *Earth and Planetary Science Letters* 279, 65-75.
- Thomazo, C., Nisbet, E.G., Grassineau, N.V., Peters, M., Strauss, H., 2013. Multiple sulfur and carbon isotope composition of sediments from the Belingwe Greenstone Belt (Zimbabwe): A biogenic methane regulation on mass independent fractionation of sulfur during the Neoproterozoic? *Geochimica et Cosmochimica Acta* 121, 120-138.
- Thomazo, C., Pinti, D.L., Busigny, V., Ader, M., Hashizume, K., Philippot, P., 2009b. Biological activity and the Earth's surface evolution: Insights from carbon, sulfur, nitrogen and iron stable isotopes in the rock record. *Comptes Rendus Palevol* 8, 665-678.
- Ueno, Y., Ono, S., Rumble, D., Maruyama, S., 2008. Quadruple sulfur isotope analysis of ca. 3.5 Ga Dresser Formation: New evidence for microbial sulfate reduction in the early Archean. *Geochimica et Cosmochimica Acta* 72, 5675-5691.
- Van Zuilen, M., Philippot, P., Whitehouse, M., Lepland, A., 2014. Sulfur isotope mass-

- independent fractionation in impact deposits of the 3.2 billion-year-old Mapepe Formation, Barberton Greenstone Belt, South Africa. *Geochimica et Cosmochimica Acta* 142, 429-441.
- Vickerman, J.C., Reed, N., Brown, A., 1989. *Secondary Ion Mass Spectroscopy: Principles and Applications (Retroactive Coverage)*. Oxford University Press, 1989, 341.
- Wacey, D., Kilburn, M.R., Saunders, M., Cliff, J., Brasier, M.D., 2011. Microfossils of sulphur-metabolizing cells in 3.4-billion-year-old rocks of Western Australia. *Nature Geoscience* 4, 698-702.
- Wacey, D., Noffke, N., Cliff, J., Barley, M.E., Farquhar, J., 2015. Micro-scale quadruple sulfur isotope analysis of pyrite from the ~ 3480Ma Dresser Formation: New insights into sulfur cycling on the early Earth. *Precambrian Research* 258, 24-35.
- Wang, Q., Morse, J.W., 1996. Pyrite formation under conditions approximating those in anoxic sediments I. Pathway and morphology. *Marine Chemistry* 52, 99-121.
- Watanabe, Y., Farquhar, J., Ohmoto, H., 2009. Anomalous fractionations of sulfur isotopes during thermochemical sulfate reduction. *Science* 324, 370-373.
- Watanabe, Y., Naraoka, H., Wronkiewicz, D.J., Condie, K.C., Ohmoto, H., 1997. Carbon, nitrogen, and sulfur geochemistry of Archean and Proterozoic shales from the Kaapvaal Craton, South Africa. *Geochimica et Cosmochimica Acta* 61, 3441-3459.
- Wilkin, R., Barnes, H., 1997. Formation processes of framboidal pyrite. *Geochimica et Cosmochimica Acta* 61, 323-339.
- Wilkin, R., Barnes, H., Brantley, S., 1996. The size distribution of framboidal pyrite in modern sediments: an indicator of redox conditions. *Geochimica et Cosmochimica Acta* 60, 3897-3912.
- Williams, P., 1985. Secondary ion mass spectrometry. *Annual Review of Materials Science* 15, 517-548.
- Yang, G., Hannah, J., Zimmerman, A., Stein, H., Bekker, A., 2009. Re-Os depositional age for Archean carbonaceous slates from the southwestern Superior Province: challenges and insights. *Earth and Planetary Science Letters* 280, 83-92.
- Zhelezinskaia, I., Kaufman, A.J., Farquhar, J., Cliff, J., 2014. Large sulfur isotope fractionations associated with Neoproterozoic microbial sulfate reduction. *Science* 346, 742-744.

Appendices

Table 1 Element concentrations of pyrite from shale in the Deer Lake Greenstone belt, Minnesota, USA

Sample	Fe (%)	Ni (%)	S (%)	Cu (%)	Total (%)	S/Fe
Nodule 1-XS-1	45.27	0.009	52.80	0.015	98.10	2.03
Nodule 1-XS-2	45.38	0.012	52.86	0.012	98.26	2.03
Nodule 1-XS-3	45.24	BDL	52.85	0.077	98.17	2.04
Nodule 1-XS-4	45.26	0.012	52.96	0.020	98.25	2.04
Nodule 1-XS-5	45.27	BDL	52.99	0.011	98.28	2.04
Nodule 1-XS-6	45.21	BDL	53.04	0.010	98.26	2.04
Nodule 1-XS-7	45.25	BDL	53.13	0.013	98.39	2.05
Nodule 1-XS-8	45.18	BDL	53.05	0.011	98.25	2.05
Nodule 1-XS-9	45.11	BDL	52.98	0.015	98.12	2.05
Nodule 1-XS-10	45.20	0.010	52.94	0.016	98.17	2.04
Nodule 1-XS-11	45.29	BDL	52.97	0.006	98.27	2.04
Nodule 1-XS-12	45.28	BDL	53.03	0.011	98.32	2.04
Nodule 1-XS-13	45.13	BDL	52.92	0.010	98.07	2.04
Nodule 1-XS-14	45.19	BDL	53.05	0.011	98.26	2.05
Nodule 1-XS-15	45.02	0.006	52.94	BDL	97.97	2.05
Nodule 1-XS-16	45.18	BDL	53.13	0.012	98.33	2.05
Nodule 1-XS-17	45.21	BDL	53.08	0.011	98.30	2.05
Nodule 1-XS-18	45.06	BDL	53.00	0.013	98.07	2.05
Nodule 1-XS-19	45.07	BDL	53.01	0.011	98.09	2.05
Nodule 1-XS-20	45.24	BDL	53.08	0.010	98.33	2.04
Nodule 1-XS-21	45.02	BDL	52.77	0.008	97.81	2.04
Nodule 1-XS-22	44.30	0.095	51.83	0.007	96.23	2.04
Nodule 1-XS-23	45.09	BDL	53.04	0.008	98.14	2.05
Nodule 1-XS-24	45.11	BDL	52.86	0.017	97.99	2.04
Nodule 1-XS-25	45.10	BDL	52.95	0.014	98.07	2.05
Nodule 1-XS-26	45.04	BDL	52.80	0.014	97.85	2.04
Nodule 1-XS-27	45.11	BDL	52.91	0.008	98.03	2.04
Nodule 1-XS-28	45.06	BDL	52.66	0.010	97.73	2.04
Nodule 1-XS-29	44.82	0.050	52.54	0.025	97.44	2.04
Nodule 1-XS-30	44.72	0.029	52.55	0.020	97.32	2.05
Nodule 1-XS-31	44.77	0.057	52.41	0.026	97.26	2.04
Nodule 1-XS-32	44.84	0.056	52.63	0.021	97.55	2.04
Nodule 1-XS-33	44.73	0.045	52.49	0.008	97.27	2.04
Nodule 1-XS-34	44.72	0.058	52.53	0.024	97.34	2.05
Nodule 1-XS-35	44.85	0.064	52.53	0.025	97.47	2.04

Sample	Fe (%)	Ni (%)	S (%)	Cu (%)	Total (%)	S/Fe
Nodule 1-XS-36	45.15	BDL	52.62	0.017	97.79	2.03
Nodule 1-XS-37	44.80	BDL	52.32	0.025	97.15	2.03
Nodule 1-XS-38	44.81	0.073	52.30	0.031	97.21	2.03
Nodule 1-XS-39	44.88	0.087	52.59	0.024	97.57	2.04
Nodule 1-XS-40	45.04	0.085	52.88	0.014	98.01	2.05
Nodule 1-XS-41	45.07	0.007	52.91	0.016	98.00	2.05
Nodule 1-XS-42	45.16	BDL	53.10	0.015	98.28	2.05
Nodule 1-XS-43	45.07	BDL	53.13	0.019	98.22	2.05
Nodule 1-XS-44	45.09	BDL	52.92	BDL	98.01	2.04
Nodule 1-XS-45	44.77	0.073	52.47	0.022	97.33	2.04
Nodule 1-XS-46	44.99	BDL	52.81	0.011	97.82	2.04
Nodule 1-XS-47	45.04	BDL	52.93	0.011	97.99	2.05
Nodule 1-XS-48	44.93	0.007	52.81	0.014	97.76	2.05
Nodule 1-XS-49	45.01	0.006	52.89	0.010	97.91	2.05
Nodule 1-XS-50	45.06	BDL	52.78	0.012	97.85	2.04
Nodule 1-XS-51	45.06	0.010	52.97	0.009	98.05	2.05
Nodule 1-XS-52	45.03	BDL	52.78	0.010	97.82	2.04
Nodule 1-XS-53	44.99	BDL	52.86	0.010	97.86	2.05
Nodule 1-XS-54	44.95	BDL	52.89	0.010	97.86	2.05
Nodule 1-XS-55	44.28	0.295	52.20	BDL	96.77	2.05
Nodule 1-XS-56	44.64	0.056	52.73	0.011	97.43	2.06
Nodule 1-XS-57	45.08	0.006	52.87	0.017	97.97	2.04
Nodule 1-XS-58	45.14	0.014	53.09	0.018	98.26	2.05
Nodule 1-XS-59	45.13	0.007	52.87	0.017	98.03	2.04
Nodule 1-XS-60	45.03	0.007	52.96	0.011	98.01	2.05
Nodule 1-XS-61	45.16	0.006	52.90	0.019	98.09	2.04
Nodule 1-XS-62	45.17	BDL	53.04	0.011	98.22	2.05
Nodule 1-XS-63	44.76	0.069	52.45	0.027	97.30	2.04
Nodule 1-XS-64	45.07	0.088	52.81	0.022	97.99	2.04
Nodule 1-XS-65	45.06	0.066	52.86	0.023	98.01	2.04
Nodule 1-XS-66	45.06	0.103	52.90	0.013	98.08	2.05
Nodule 1-XS-67	44.92	0.138	52.61	0.018	97.68	2.04
Nodule 1-XS-68	44.86	0.061	52.64	0.022	97.58	2.04
Nodule 1-XS-69	45.27	BDL	53.14	0.018	98.43	2.04
Nodule 1-XS-70	45.22	0.049	52.81	0.018	98.10	2.03
Nodule 1-XS-71	44.97	0.027	52.83	0.014	97.83	2.05
Nodule 1-XS-72	45.03	BDL	53.01	0.009	98.06	2.05
Nodule 1-XS-73	44.98	0.079	52.63	0.033	97.72	2.04
Nodule 1-XS-74	44.98	0.103	52.74	0.109	97.93	2.04
Nodule 1-XS-75	45.23	0.044	52.98	0.029	98.28	2.04
Nodule 1-XS-76	45.20	BDL	53.05	0.016	98.27	2.04

Sample	Fe (%)	Ni (%)	S (%)	Cu (%)	Total (%)	S/Fe
Nodule 1-XS-77	44.90	0.081	52.83	0.073	97.88	2.05
Nodule 1-XS-78	44.95	0.086	52.81	0.025	97.87	2.05
Nodule 1-XS-79	44.73	0.098	52.63	0.272	97.73	2.05
Nodule 1-XS-80	44.87	0.035	52.58	0.026	97.52	2.04
Nodule 1-XS-81	44.91	0.079	52.55	0.020	97.57	2.04
Nodule 1-XS-82	45.26	0.101	53.20	0.010	98.57	2.05
Nodule 1-XS-83	44.07	0.529	51.37	BDL	95.97	2.03
Nodule 1-XS-84	18.33	0.068	21.33	0.018	39.75	2.03
Nodule 1-XS-85	45.03	0.070	52.74	0.014	97.85	2.04
Nodule 1-XS-86	39.55	0.148	45.56	0.018	85.27	2.01
Nodule 1-XS-87	45.10	0.141	52.70	0.169	98.12	2.04
Nodule 1-XS-88	45.05	0.067	52.58	0.035	97.73	2.03
Nodule 1-XS-89	45.21	0.087	52.79	0.023	98.11	2.03
Nodule 1-XS-90	45.16	0.105	52.92	0.028	98.22	2.04
Nodule 1-XS-91	44.45	0.132	51.90	0.019	96.49	2.03
Nodule 1-XS-92	45.08	0.107	52.68	0.025	97.89	2.04
Nodule 1-XS-93	45.16	0.092	52.86	0.022	98.14	2.04
Nodule 1-XS-94	45.12	0.075	52.68	0.035	97.90	2.03
Nodule 1-XS-95	45.20	0.132	52.92	0.028	98.28	2.04
Nodule 1-XS-96	44.85	0.078	52.38	0.029	97.34	2.03
Nodule 1-XS-97	45.09	0.133	52.80	0.025	98.05	2.04
Nodule 1-XS-98	45.23	0.162	52.90	0.010	98.30	2.04
Nodule 1-XS-99	44.97	0.109	52.46	0.093	97.64	2.03
Nodule 1-XS-100	44.75	0.065	52.42	0.037	97.27	2.04
Nodule 1-XS-101	42.73	0.195	49.78	1.389	94.10	2.03
Nodule 1-XS-102	44.62	0.062	52.04	0.046	96.77	2.03
Nodule 1-XS-103	45.23	0.129	52.81	0.010	98.18	2.03
Nodule 1-XS-104	45.07	0.115	52.46	0.032	97.68	2.03
Nodule 1-XS-105	44.98	0.104	52.24	0.027	97.35	2.02
Nodule 1-XS-106	44.85	0.093	52.15	0.039	97.14	2.03
Nodule 1-XS-107	43.38	0.203	50.80	0.019	94.40	2.04
Nodule 1-XS-108	44.98	0.118	52.62	0.019	97.74	2.04
Nodule 1-XS-109	45.00	0.123	52.78	0.021	97.92	2.04
Nodule 1-XS-110	44.92	0.066	52.59	0.036	97.61	2.04
Nodule 1-XS-111	44.87	0.105	52.56	0.031	97.56	2.04
Nodule 1-XS-112	44.94	0.123	52.67	0.030	97.76	2.04
Nodule 1-XS-113	44.51	0.080	52.00	0.051	96.64	2.04
Nodule 1-XS-114	44.90	0.125	52.76	0.025	97.81	2.05
Nodule 1-XS-115	44.76	0.087	52.53	0.036	97.41	2.04
Nodule 1-XS-116	44.73	0.140	52.44	0.026	97.34	2.04
Nodule 1-XS-117	44.41	0.129	51.75	0.046	96.34	2.03

Sample	Fe (%)	Ni (%)	S (%)	Cu (%)	Total (%)	S/Fe
Nodule 1-XS-118	44.17	0.039	52.14	0.029	96.38	2.06
Nodule 1-XS-119	44.28	0.100	52.18	0.030	96.60	2.05
Nodule 1-XS-120	44.68	0.135	52.56	0.047	97.43	2.05
Nodule 1-XS-121	44.50	0.073	52.34	0.018	96.94	2.05
Nodule 1-XS-122	44.58	0.115	52.65	0.030	97.37	2.06
Nodule 1-XS-123	44.62	0.062	52.04	0.046	96.77	2.03
Nodule 1-XS-124	44.44	0.120	52.33	0.029	96.92	2.05
Nodule 1-XS-125	44.36	0.091	52.39	0.023	96.86	2.06
Nodule 1-XS-126	44.28	0.081	52.22	0.024	96.60	2.05
Nodule 1-XS-127	44.33	0.062	52.05	0.034	96.48	2.05
Nodule 1-XS-128	44.10	0.122	52.17	0.023	96.41	2.06
Nodule 1-XS-129	44.26	0.168	52.42	0.168	97.01	2.06
Nodule 1-XS-130	43.57	0.082	51.23	0.030	94.90	2.05
Nodule 1-XS-131	43.89	0.063	51.60	0.036	95.58	2.05
Nodule 1-XS-132	43.95	0.097	51.76	0.112	95.93	2.05
Nodule 1-XS-133	43.56	0.091	51.60	0.050	95.30	2.06
Nodule 1-XS-134	44.10	0.128	52.23	0.038	96.49	2.06
Nodule 1-XS-135	43.41	0.098	51.35	0.056	94.92	2.06
Nodule 1-XS-136	43.59	0.054	51.75	0.047	95.44	2.07
Nodule 1-XS-137	43.31	0.038	51.40	0.030	94.78	2.07
Nodule 1-XS-138	43.24	0.042	50.98	0.068	94.32	2.05
Nodule 1-XS-139	43.65	0.086	51.68	0.033	95.45	2.06
Nodule 1-XS-140	43.26	0.047	51.14	0.046	94.50	2.06
Nodule 1-XS-141	43.73	0.108	51.84	0.026	95.71	2.07
Nodule 1-XS-142	43.38	0.074	51.23	0.044	94.73	2.06
Nodule 1-XS-143	42.90	0.140	50.84	0.548	94.42	2.06
Nodule 1-XS-144	43.75	0.096	51.58	0.045	95.46	2.05
Nodule 1-XS-145	43.94	0.045	51.84	0.025	95.85	2.06
Nodule 1-XS-146	43.76	0.118	51.74	0.030	95.65	2.06
Nodule 1-XS-147	44.10	0.141	51.79	0.057	96.09	2.05
Nodule 1-XS-148	40.87	0.116	48.10	0.308	89.39	2.05
Nodule 1-XS-149	33.35	0.134	40.14	0.019	73.64	2.10
Nodule 1-XS-150	44.20	0.076	51.95	0.027	96.25	2.05
Nodule 1-XS-151	44.26	0.061	52.02	0.034	96.37	2.05
Nodule 1-XS-152	44.51	0.094	52.02	0.034	96.65	2.04
Nodule 1-XS-153	44.38	0.124	52.21	0.020	96.73	2.05
Nodule 1-XS-154	5.61	0.030	7.05	0.032	12.77	2.19
Nodule 1-XS-155	5.67	0.027	7.24	0.047	12.99	2.22
Nodule 1-XS-156	44.39	0.143	52.08	0.013	96.63	2.04
Nodule 1-XS-157	44.42	0.210	52.40	0.020	97.05	2.05
Nodule 1-XS-158	15.95	0.025	19.19	0.019	35.18	2.10

Sample	Fe (%)	Ni (%)	S (%)	Cu (%)	Total (%)	S/Fe
Nodule 1-XS-159	44.54	0.143	52.52	0.016	97.22	2.05
Nodule 1-XS-160	43.83	0.011	49.23	0.096	93.16	1.96
Nodule 1-XS-161	44.69	0.108	52.49	0.029	97.31	2.05
Nodule 1-XS-162	44.50	0.117	52.30	0.045	96.96	2.05
Nodule 1-XS-163	0.74	BDL	0.24	0.026	1.01	0.57
Nodule 1-XS-164	44.45	0.167	52.33	0.035	96.98	2.05
Nodule 1-XS-165	44.79	0.139	52.82	0.018	97.77	2.05
Nodule 1-XS-166	43.94	0.045	51.84	0.025	95.85	2.06
Nodule 1-XS-167	44.07	0.099	51.46	0.049	95.68	2.03
Nodule 1-XS-168	44.58	0.156	52.62	0.015	97.36	2.06
Nodule 1-XS-169	43.83	0.070	51.60	0.027	95.53	2.05
Nodule 1-XS-170	44.38	0.153	52.22	0.071	96.82	2.05
Nodule 1-XS-171	44.50	0.092	52.02	0.032	96.64	2.04
Nodule 1-XS-172	44.22	0.061	51.73	0.037	96.05	2.04
Nodule 1-XS-173	44.75	0.071	52.60	0.167	97.60	2.05
Nodule 1-XS-174	43.91	0.216	51.35	1.462	96.94	2.04
Nodule 1-XS-175	44.61	0.140	52.15	0.018	96.92	2.04
Nodule 1-XS-176	44.55	0.120	52.27	0.029	96.96	2.04
Nodule 1-XS-177	44.78	0.130	52.74	0.024	97.67	2.05
Nodule 1-XS-178	44.66	0.160	52.71	0.015	97.55	2.06
Nodule 1-XS-179	44.57	0.137	52.81	0.023	97.55	2.06
Nodule 1-XS-180	44.72	0.163	52.58	0.027	97.49	2.05
Nodule 1-XS-181	44.57	0.168	52.31	0.043	97.09	2.04
Nodule 1-XS-182	44.75	0.155	52.42	0.021	97.35	2.04
Nodule 1-XS-183	44.69	0.079	52.18	0.038	96.98	2.03
Nodule 1-XS-184	44.85	0.121	52.50	0.022	97.50	2.04
Nodule 1-XS-185	43.57	0.068	52.74	0.036	96.41	2.11
Nodule 1-XS-186	44.28	0.133	52.05	0.033	96.50	2.05
Nodule 1-XS-187	44.48	0.155	52.25	0.067	96.96	2.05
Nodule 1-XS-188	44.22	0.071	51.67	0.043	96.01	2.04
Nodule 1-XS-189	44.55	0.139	52.23	0.242	97.16	2.04
Nodule 1-XS-190	44.57	0.144	52.54	0.029	97.28	2.05
Nodule 1-XS-191	44.10	0.080	51.83	0.033	96.04	2.05
Nodule 1-XS-192	39.74	0.118	47.42	0.037	87.32	2.08
Nodule 1-XS-193	44.25	0.093	52.08	0.029	96.46	2.05
Nodule 1-XS-194	43.34	0.161	50.74	0.043	94.28	2.04
Nodule 1-XS-195	44.62	0.220	52.19	0.099	97.13	2.04
Nodule 1-XS-196	43.80	0.076	51.43	0.027	95.33	2.05
Nodule 1-XS-197	44.45	0.146	52.27	0.192	97.06	2.05
Nodule 1-XS-198	43.82	0.076	51.77	0.036	95.70	2.06
Nodule 1-XS-199	4.32	0.035	5.50	0.028	10.02	2.22

Sample	Fe (%)	Ni (%)	S (%)	Cu (%)	Total (%)	S/Fe
Nodule 1-XS-200	42.21	0.169	48.77	0.048	91.20	2.01
Nodule 1-XS-201	44.59	0.182	52.44	0.026	97.24	2.05
Nodule 1-XS-202	44.77	0.115	52.53	0.052	97.47	2.04
Nodule 1-XS-203	44.51	0.147	52.41	0.026	97.10	2.05
Nodule 1-XS-204	43.70	0.080	50.90	0.060	94.74	2.03
Nodule 1-XS-205	44.24	0.104	52.10	0.033	96.48	2.05
Nodule 1-XS-206	44.46	0.117	52.13	0.033	96.74	2.04
Nodule 1-XS-207	24.02	0.207	27.85	0.007	52.08	2.02
Nodule 1-XS-208	42.19	0.118	49.23	0.023	91.56	2.03
Nodule 1-XS-209	44.22	0.071	51.67	0.043	96.01	2.04
Nodule 1-XS-210	44.06	0.095	51.75	0.030	95.94	2.05
Nodule 1-XS-211	44.68	0.227	52.61	0.008	97.52	2.05
Nodule 1-XS-212	44.35	0.062	51.96	0.029	96.40	2.04
Nodule 1-XS-213	43.99	0.193	52.06	0.272	96.51	2.06
Nodule 1-XS-214	37.95	0.102	45.47	0.150	83.67	2.09
Nodule 1-XS-215	43.79	0.079	51.68	0.044	95.59	2.06
Nodule 1-XS-216	43.58	0.108	51.32	0.035	95.04	2.05
Nodule 1-XS-217	43.57	0.060	51.42	0.070	95.11	2.06
Nodule 1-XS-218	43.73	0.060	51.42	0.041	95.24	2.05
Nodule 1-XS-219	43.75	0.030	51.39	0.021	95.19	2.05
Nodule 1-XS-220	44.38	0.088	51.94	0.027	96.44	2.04
Nodule 1-XS-221	43.33	0.063	50.94	0.065	94.39	2.05
Nodule 1-XS-222	44.10	0.095	51.39	0.035	95.61	2.03
Nodule 1-XS-223	43.23	0.080	50.71	0.037	94.06	2.04
Nodule 1-XS-224	42.96	0.046	50.65	0.050	93.71	2.05
Nodule 1-XS-225	43.85	0.066	51.47	0.038	95.42	2.04
Nodule 1-XS-226	43.58	0.062	51.29	0.047	94.99	2.05
Nodule 1-XS-227	43.51	0.051	51.24	0.035	94.84	2.05
Nodule 1-XS-228	42.90	0.059	50.77	0.155	93.88	2.06
Nodule 1-XS-229	43.83	0.097	51.77	0.028	95.73	2.06
Nodule 1-XS-230	43.86	0.094	51.69	0.041	95.69	2.05
Nodule 1-XS-231	43.49	0.061	51.22	0.048	94.82	2.05
Nodule 1-XS-232	43.19	0.037	51.15	0.040	94.42	2.06
Nodule 1-XS-233	43.48	0.076	51.16	0.049	94.77	2.05
Nodule 1-XS-234	43.87	0.095	51.57	0.026	95.56	2.05
Nodule 1-XS-235	43.87	0.095	51.65	0.024	95.64	2.05
Nodule 1-XS-236	44.06	0.102	51.72	0.106	95.99	2.04
Nodule 1-XS-237	43.59	0.046	51.36	0.062	95.06	2.05
Nodule 1-XS-238	42.65	0.064	49.86	0.031	92.61	2.04
Nodule 1-XS-239	43.30	0.086	50.12	0.063	93.57	2.02
Nodule 1-XS-240	43.65	0.086	51.02	0.028	94.79	2.04

Sample	Fe (%)	Ni (%)	S (%)	Cu (%)	Total (%)	S/Fe
Nodule 1-XS-241	44.08	0.058	51.64	0.027	95.81	2.04
Nodule 1-XS-242	43.59	0.082	50.95	0.044	94.66	2.04
Nodule 1-XS-243	43.37	0.069	51.37	0.026	94.84	2.06
Nodule 1-XS-244	43.31	0.089	50.79	0.029	94.22	2.04
Nodule 1-XS-245	43.38	0.097	51.00	0.036	94.51	2.05
Nodule 1-XS-246	39.24	0.064	46.16	0.334	85.80	2.05
Nodule 1-XS-247	43.82	0.119	50.86	0.022	94.82	2.02
Nodule 1-XS-248	42.30	0.121	49.60	0.028	92.05	2.04
Nodule 1-XS-249	44.30	0.129	51.93	0.033	96.40	2.04
Nodule 1-XS-250	44.62	0.107	52.43	0.022	97.18	2.05
Nodule 1-XS-251	44.71	0.077	52.35	0.025	97.16	2.04
Nodule 1-XS-252	44.28	0.078	52.14	0.036	96.53	2.05
Nodule 1-XS-253	44.32	0.077	52.18	0.019	96.59	2.05
Nodule 1-XS-254	44.76	0.101	52.48	0.029	97.37	2.04
Nodule 1-XS-255	44.65	0.128	52.25	0.024	97.06	2.04
Nodule 1-XS-256	43.97	0.065	51.67	0.042	95.75	2.05
Nodule 1-XS-257	44.68	0.072	52.44	0.034	97.23	2.04
Nodule 1-XS-258	44.35	0.085	52.16	0.027	96.63	2.05
Nodule 1-XS-259	42.96	0.036	50.69	0.028	93.71	2.06
Nodule 1-XS-260	44.45	0.158	52.54	0.028	97.18	2.06
Nodule 1-XS-261	44.15	0.048	51.95	0.046	96.19	2.05
Nodule 1-XS-262	44.29	0.048	52.16	0.029	96.52	2.05
Nodule 1-XS-263	44.48	0.043	51.98	0.025	96.53	2.04
Nodule 1-XS-264	44.71	0.061	52.37	0.027	97.17	2.04
Nodule 1-XS-265	44.93	0.095	52.65	0.025	97.70	2.04
Nodule 1-XS-266	44.73	0.068	52.43	0.032	97.26	2.04
Nodule 1-XS-267	44.95	0.117	52.85	0.027	97.94	2.05
Nodule 1-XS-268	44.63	0.040	52.47	0.036	97.18	2.05
Nodule 1-XS-269	44.97	0.100	52.55	0.030	97.65	2.04
Nodule 1-XS-270	45.07	0.092	52.77	0.030	97.97	2.04
Nodule 1-XS-271	44.74	0.044	52.39	0.024	97.20	2.04
Nodule 1-XS-272	44.86	0.080	52.56	0.042	97.54	2.04
Nodule 1-XS-273	44.95	0.083	52.59	0.161	97.78	2.04
Nodule 1-XS-274	45.10	0.085	52.88	0.026	98.09	2.04
Nodule 1-XS-275	44.97	0.074	53.00	0.027	98.08	2.05
Nodule 1-XS-276	44.98	0.090	53.53	0.018	98.62	2.07
Nodule 1-XS-277	44.89	0.072	52.72	0.028	97.70	2.05
Nodule 1-XS-278	45.15	0.082	52.98	0.025	98.23	2.04
Nodule 1-XS-279	45.03	0.074	52.74	0.030	97.87	2.04
Nodule 1-XS-280	45.19	0.072	52.82	0.028	98.12	2.04
Nodule 1-XS-281	44.97	0.040	52.67	0.040	97.72	2.04

Sample	Fe (%)	Ni (%)	S (%)	Cu (%)	Total (%)	S/Fe
Nodule 1-XS-282	45.40	0.011	52.94	0.014	98.37	2.03
Nodule 1-XS-283	44.57	0.057	52.16	0.026	96.81	2.04
Nodule 1-XS-284	45.46	0.012	52.94	0.014	98.43	2.03
Nodule 1-XS-285	45.45	0.034	53.07	0.027	98.58	2.03
Nodule 1-XS-286	45.01	0.015	52.60	0.034	97.65	2.04
Nodule 1-XS-287	44.64	0.021	52.29	0.478	97.43	2.04
Nodule 1-XS-288	44.60	0.105	52.08	1.576	98.36	2.03
Nodule 1-XS-289	45.13	0.070	52.79	0.028	98.03	2.04
Nodule 1-XS-290	45.03	0.061	52.69	0.079	97.86	2.04
Nodule 1-XS-291	45.49	BDL	53.17	0.019	98.68	2.04
Nodule 1-XS-292	45.45	BDL	53.09	0.015	98.56	2.03
Nodule 1-XS-293	45.22	BDL	52.95	0.022	98.20	2.04
Nodule 1-XS-294	45.11	0.056	52.73	0.041	97.93	2.04
Nodule 1-XS-295	45.08	0.062	52.73	0.024	97.90	2.04
Nodule 1-XS-296	45.07	0.037	52.86	0.026	97.99	2.04
Nodule 1-XS-297	45.13	0.063	52.75	0.020	97.96	2.04
Nodule 1-XS-298	45.05	0.064	52.73	0.026	97.87	2.04
Nodule 1-XS-299	45.22	BDL	52.88	0.013	98.12	2.04
Nodule 1-XS-300	45.10	BDL	52.79	BDL	97.89	2.04
Nodule 1-XS-301	45.19	BDL	53.01	0.016	98.22	2.04
Nodule 1-XS-302	45.21	BDL	53.03	0.020	98.26	2.04
Nodule 1-XS-303	45.30	BDL	53.11	0.018	98.44	2.04
Nodule 1-XS-304	45.26	BDL	53.02	0.011	98.29	2.04
Nodule 1-XS-305	45.37	BDL	53.19	0.014	98.58	2.04
Nodule 1-XS-306	45.22	BDL	53.05	0.017	98.29	2.04
Nodule 1-XS-307	44.98	0.052	52.61	0.204	97.85	2.04
Nodule 1-XS-308	45.11	0.053	52.67	0.076	97.91	2.03
Nodule 1-XS-309	45.24	0.020	52.86	0.017	98.14	2.04
Nodule 1-XS-310	45.27	0.049	52.96	0.024	98.31	2.04
Nodule 1-XS-311	45.27	0.058	52.98	0.030	98.34	2.04
Nodule 1-XS-312	45.26	0.061	53.12	0.024	98.47	2.04
Nodule 1-XS-313	45.30	0.053	53.11	0.031	98.50	2.04
Nodule 1-XS-314	45.38	0.057	52.91	0.036	98.39	2.03
Nodule 1-XS-315	45.23	0.041	52.83	0.030	98.13	2.03
Nodule 1-XS-316	45.21	0.052	52.82	0.023	98.11	2.04
Nodule 1-XS-317	45.31	0.019	52.90	0.044	98.27	2.03
Nodule 1-XS-318	45.47	BDL	53.09	0.011	98.58	2.03
Nodule 1-XS-319	45.55	BDL	53.21	0.012	98.77	2.04
Nodule 1-XS-320	45.63	BDL	53.28	0.019	98.94	2.03
Nodule 1-XS-321	45.51	BDL	53.26	0.015	98.78	2.04
Nodule 1-XS-322	45.52	BDL	53.14	BDL	98.66	2.03

Sample	Fe (%)	Ni (%)	S (%)	Cu (%)	Total (%)	S/Fe
Nodule 1-XS-323	45.46	BDL	53.33	0.010	98.79	2.04
Nodule 1-XS-324	45.48	BDL	53.22	0.012	98.71	2.04
Nodule 1-XS-325	45.48	BDL	53.23	0.017	98.74	2.04
Nodule 1-XS-326	45.46	BDL	53.18	0.013	98.65	2.04
Nodule 1-XS-327	45.35	0.009	53.18	0.014	98.55	2.04
Nodule 1-XS-328	45.41	BDL	53.27	0.009	98.69	2.04
Nodule 1-XS-329	45.29	BDL	53.17	0.016	98.47	2.05
Nodule 1-XS-330	45.48	BDL	53.16	0.009	98.65	2.04
Nodule 1-XS-331	45.39	0.009	53.25	0.015	98.66	2.04
Nodule 1-XS-332	45.44	BDL	53.15	0.011	98.61	2.04
Nodule 1-XS-333	45.37	BDL	53.14	BDL	98.52	2.04
Nodule 1-XS-334	45.41	BDL	53.16	0.007	98.59	2.04
Nodule 1-XS-335	45.38	BDL	53.14	BDL	98.53	2.04
Nodule 1-XS-336	44.95	0.028	52.70	0.025	97.71	2.04
Nodule 1-XS-337	44.86	0.011	52.73	0.006	97.61	2.05
Nodule 1-XS-338	45.21	BDL	53.16	BDL	98.38	2.05
Nodule 1-XS-339	45.20	BDL	53.17	0.020	98.39	2.05
Nodule 1-XS-340	45.16	BDL	53.18	0.014	98.36	2.05
Nodule 2-XSA-1	44.47	0.077	50.41	0.037	95.00	1.97
Nodule 2-XSA-2	44.31	0.043	51.54	0.037	95.93	2.03
Nodule 2-XSA-3	44.73	0.090	51.67	0.041	96.53	2.01
Nodule 2-XSA-4	44.81	0.127	51.77	0.026	96.74	2.01
Nodule 2-XSA-5	44.02	0.078	51.64	0.024	95.77	2.04
Nodule 2-XSA-6	45.18	0.172	52.54	0.015	97.91	2.03
Nodule 2-XSA-7	44.62	0.090	51.90	0.033	96.64	2.03
Nodule 2-XSA-8	44.66	0.102	51.78	0.048	96.60	2.02
Nodule 2-XSA-9	44.35	0.073	51.78	0.034	96.24	2.03
Nodule 2-XSA-10	44.77	0.093	52.18	0.031	97.08	2.03
Nodule 2-XSA-11	44.47	0.083	51.89	0.041	96.48	2.03
Nodule 2-XSA-12	43.55	0.052	51.08	0.081	94.76	2.04
Nodule 2-XSA-13	44.18	0.106	51.53	0.050	95.86	2.03
Nodule 2-XSB-1	44.27	0.067	52.18	0.031	96.54	2.05
Nodule 2-XSB-2	44.05	0.083	51.92	0.033	96.09	2.05
Nodule 2-XSB-3	44.57	0.090	52.34	0.035	97.04	2.05
Nodule 2-XSB-4	44.11	0.053	51.79	0.030	95.98	2.05
Nodule 2-XSB-5	43.61	0.025	51.48	0.036	95.16	2.06
Nodule 2-XSB-6	43.48	0.038	52.07	0.040	95.63	2.09
Nodule 2-XSB-7	44.22	0.068	52.00	0.030	96.32	2.05
Nodule 2-XSB-8	44.20	0.070	51.62	0.043	95.93	2.03
Nodule 2-XSB-9	44.07	0.071	51.73	0.036	95.91	2.04
Nodule 2-XSB-10	44.15	0.064	51.93	0.034	96.18	2.05

Sample	Fe (%)	Ni (%)	S (%)	Cu (%)	Total (%)	S/Fe
Nodule 2-XSB-11	43.96	0.055	51.81	0.038	95.86	2.05
Nodule 2-XSB-12	43.79	0.043	51.51	0.044	95.39	2.05
Nodule 2-XSB-13	44.36	0.093	52.01	0.038	96.50	2.04
Nodule 2-XSB-14	43.54	0.051	51.44	0.026	95.06	2.06
Nodule 2-XSB-15	43.88	0.063	51.60	0.044	95.59	2.05
Nodule 2-XSB-16	44.09	0.051	51.68	0.039	95.86	2.04
Nodule 2-XSB-17	43.87	0.094	51.42	0.036	95.42	2.04
Nodule 2-XSB-18	43.98	0.079	51.57	0.042	95.68	2.04
Nodule 2-XSB-19	44.45	0.063	51.90	0.036	96.45	2.03
Nodule 2-XSB-20	44.14	0.049	51.76	0.030	95.98	2.04
Nodule 2-XSB-21	44.53	0.075	52.07	0.037	96.72	2.04
Nodule 2-XSB-22	44.32	0.078	51.74	0.040	96.17	2.03
Nodule 2-XSB-23	44.02	0.053	51.25	0.046	95.37	2.03
Nodule 2-XSB-24	44.60	0.088	52.45	0.033	97.17	2.05
Nodule 2-XSB-25	44.57	0.057	52.46	0.036	97.12	2.05
Nodule 2-XSB-26	44.79	0.067	52.53	0.031	97.42	2.04
Nodule 2-XSB-27	44.53	0.067	51.97	0.041	96.60	2.03
Nodule 2-XSB-28	44.21	0.061	50.47	0.054	94.79	1.99
Nodule 2-XSB-29	44.63	0.028	52.24	0.026	96.92	2.04
Nodule 2-XSB-30	44.83	0.117	52.50	0.031	97.48	2.04
Nodule 2-XSB-31	43.88	0.048	51.57	0.028	95.52	2.05
Nodule 2-XSB-32	44.09	0.096	51.64	0.027	95.85	2.04
Nodule 2-XSB-33	43.98	0.083	51.21	0.040	95.32	2.03
Nodule 2-XSC-1	44.09	0.063	51.68	0.040	95.86	2.04
Nodule 2-XSC-2	43.99	0.066	51.88	0.036	95.97	2.05
Nodule 2-XSC-3	44.08	0.071	51.80	0.036	95.98	2.05
Nodule 2-XSC-4	44.27	0.118	52.04	0.016	96.44	2.05
Nodule 2-XSC-5	44.21	0.049	51.95	0.027	96.23	2.05
Nodule 2-XSC-6	44.08	0.127	52.36	0.018	96.58	2.07
Nodule 2-XSC-7	43.89	0.054	51.63	0.039	95.61	2.05
Nodule 2-XSC-8	44.40	0.074	52.23	0.025	96.73	2.05
Nodule 2-XSC-9	44.53	0.097	52.20	0.029	96.85	2.04
Nodule 2-XSC-10	43.95	0.050	51.61	0.035	95.65	2.05
Nodule 2-XSC-11	44.00	0.070	51.99	0.029	96.10	2.06
Nodule 2-XSC-12	44.42	0.124	52.18	0.033	96.76	2.05
Nodule 2-XSC-13	44.17	0.104	52.15	0.019	96.44	2.06
Nodule 2-XSC-14	2.97	BDL	0.48	0.135	3.58	0.28
Nodule 2-XSC-15	43.71	0.047	51.67	0.026	95.46	2.06
Nodule 2-XSC-16	0.67	BDL	0.38	BDL	1.07	0.99
Nodule 2-XSC-17	0.34	BDL	0.05	0.006	0.45	0.26
Nodule 2-XSC-18	0.28	BDL	0.03	0.007	0.32	0.19

Sample	Fe (%)	Ni (%)	S (%)	Cu (%)	Total (%)	S/Fe
Nodule 2-XSC-19	0.26	BDL	0.06	BDL	0.33	0.40
Nodule 2-XSC-20	42.07	0.080	48.08	0.015	90.24	1.99
Nodule 2-XSC-21	43.66	0.044	51.13	0.035	94.88	2.04
Nodule 2-XSC-22	44.38	0.075	52.31	0.031	96.80	2.05
Nodule 2-XSC-23	44.07	0.021	52.09	0.018	96.19	2.06
Nodule 2-XSC-24	44.22	0.052	52.13	0.022	96.42	2.05
Nodule 2-XSC-25	42.41	0.070	49.76	0.025	92.27	2.04
Nodule 2-XSC-26	43.23	0.075	50.82	0.030	94.16	2.05
Nodule 2-XSC-27	43.73	0.042	51.44	0.062	95.27	2.05
Nodule 2-XSC-28	42.89	0.046	50.36	0.163	93.47	2.05
Nodule 2-XSC-29	44.29	0.027	52.27	0.029	96.62	2.06
Nodule 2-XSC-30	44.33	0.064	52.45	0.036	96.88	2.06
Nodule 2-XSC-31	44.19	0.027	52.92	0.029	97.16	2.09
Nodule 2-XSC-32	41.15	0.063	49.28	0.106	90.60	2.09
Nodule 2-XSC-33	42.73	0.087	50.67	0.035	93.53	2.07
Nodule 2-XSC-34	43.75	0.069	51.34	0.055	95.21	2.04
Nodule 2-XSC-35	44.39	0.074	53.11	0.037	97.61	2.08
Nodule 2-XSC-36	44.13	0.078	52.03	0.025	96.26	2.05
Nodule 2-XSC-37	44.00	0.041	51.89	0.025	95.95	2.05
Nodule 2-XSC-38	43.39	0.072	51.73	0.026	95.22	2.08
Nodule 2-XSC-39	44.09	0.077	51.53	0.082	95.78	2.04
Nodule 2-XSC-40	44.13	0.084	52.82	0.037	97.06	2.09
Nodule 2-XSC-41	43.56	0.045	51.45	0.039	95.09	2.06
Nodule 2-XSC-42	43.47	0.067	51.57	0.025	95.13	2.07
Nodule 2-XSC-43	44.34	0.092	52.10	0.028	96.55	2.05
Nodule 2-XSC-44	44.09	0.069	51.76	0.040	95.95	2.05
Nodule 2-XSC-45	44.04	0.071	51.94	0.029	96.08	2.05
Nodule 2-XSC-46	43.87	0.038	51.69	0.031	95.62	2.05
Nodule 2-XSC-47	44.40	0.075	52.15	0.027	96.65	2.05
Nodule 2-XSC-48	44.15	0.075	52.01	0.035	96.27	2.05
Nodule 2-XSC-49	44.25	0.098	52.37	0.026	96.74	2.06
Nodule 2-XSC-50	44.13	0.076	52.22	0.044	96.47	2.06
Nodule 2-XSC-51	43.83	0.069	51.59	0.038	95.52	2.05
Nodule 2-XSC-52	43.85	0.072	51.63	0.044	95.60	2.05
Nodule 2-XSC-53	43.88	0.077	51.82	0.036	95.82	2.06
Nodule 2-XSC-54	44.19	0.145	52.17	0.016	96.53	2.06
Nodule 2-XSC-55	9.75	0.013	12.36	BDL	22.12	2.21
Nodule 2-XSC-56	43.55	0.113	51.17	0.023	94.86	2.05
Nodule 2-XSC-57	43.99	0.074	51.82	0.033	95.92	2.05
Nodule 2-XSC-58	43.84	0.093	51.72	0.034	95.69	2.06
Nodule 2-XSC-59	43.75	0.090	52.29	0.038	96.16	2.08

Sample	Fe (%)	Ni (%)	S (%)	Cu (%)	Total (%)	S/Fe
Nodule 2-XSC-60	43.99	0.117	51.79	0.019	95.92	2.05
Nodule 2-XSC-61	43.76	0.089	51.46	0.039	95.35	2.05
Nodule 2-XSC-62	44.00	0.096	51.93	0.027	96.06	2.06
Nodule 2-XSC-63	43.46	0.068	50.98	0.051	94.56	2.04
Nodule 2-XSC-64	43.92	0.037	51.86	0.023	95.84	2.06
Nodule 2-XSC-65	44.31	0.108	52.03	0.024	96.47	2.05
Nodule 2-XSC-66	44.37	0.105	52.33	0.033	96.85	2.05
Nodule 2-XSC-67	44.38	0.092	52.33	0.026	96.83	2.05
Nodule 2-XSC-68	43.40	0.067	51.45	0.106	95.03	2.07
Nodule 2-XSC-69	43.80	0.061	51.56	0.037	95.45	2.05
Nodule 2-XSC-70	44.20	0.086	52.13	0.037	96.45	2.05
Nodule 2-XSC-71	43.92	0.061	51.68	0.033	95.69	2.05
Nodule 2-XSC-72	43.49	0.086	51.28	0.036	94.89	2.05
Nodule 2-XSC-73	44.06	0.084	51.79	0.032	95.96	2.05
Nodule 2-XSC-74	44.08	0.014	51.79	0.021	95.90	2.05
Nodule 2-XSC-75	44.14	0.093	51.82	0.030	96.09	2.05
Nodule 2-XSC-76	43.02	0.069	50.83	0.034	93.96	2.06
Nodule 2-XSC-77	43.43	0.086	51.47	0.035	95.02	2.06
Nodule 2-XSC-78	44.21	0.040	51.98	0.030	96.26	2.05
Nodule 2-XSC-79	43.59	0.071	50.95	0.113	94.72	2.04
Nodule 2-XSC-80	44.32	0.101	52.08	0.028	96.53	2.05
Nodule 2-XSC-81	44.27	0.071	52.15	0.043	96.53	2.05
Nodule 2-XSC-82	44.20	0.057	51.92	0.035	96.22	2.05
Nodule 2-XSC-83	43.53	0.062	51.03	0.040	94.66	2.04
Nodule 2-XSC-84	43.46	0.070	50.96	0.011	94.50	2.04
Nodule 2-XSC-85	44.08	0.089	51.75	0.031	95.95	2.05
Nodule 2-XSC-86	44.34	0.104	52.03	0.026	96.50	2.04
Nodule 2-XSC-87	43.57	0.086	51.15	0.040	94.85	2.05
Nodule 2-XSC-88	43.98	0.028	52.44	0.024	96.47	2.08
Nodule 2-XSC-89	0.87	BDL	0.79	0.007	1.75	1.58
Nodule 2-XSC-90	43.71	0.085	51.50	0.031	95.32	2.05
Nodule 2-XSC-91	43.70	0.088	51.94	0.032	95.76	2.07
Nodule 2-XSC-92	44.48	0.133	52.11	0.036	96.76	2.04
Nodule 2-XSC-93	44.41	0.082	51.63	0.045	96.16	2.03
Nodule 2-XSC-94	44.61	0.146	52.22	0.032	97.01	2.04
Nodule 2-XSC-95	43.98	0.110	51.57	0.033	95.69	2.04
Nodule 2-XSC-96	44.18	0.081	51.84	0.052	96.15	2.04
Nodule 2-XSC-97	43.56	0.064	50.85	0.042	94.52	2.03
Nodule 2-XSC-98	44.16	0.054	51.65	0.036	95.91	2.04
Nodule 2-XSC-99	44.11	0.037	51.82	0.030	96.00	2.05
Nodule 2-XSC-100	44.39	0.099	52.00	0.036	96.52	2.04

Sample	Fe (%)	Ni (%)	S (%)	Cu (%)	Total (%)	S/Fe
Nodule 2-XSC-101	44.26	0.087	51.72	0.033	96.10	2.04
Nodule 2-XSC-102	44.34	0.061	51.97	0.027	96.39	2.04
Nodule 2-XSC-103	44.38	0.069	51.85	0.038	96.33	2.04
Nodule 2-XSC-104	44.76	0.102	52.37	0.040	97.27	2.04
Nodule 2-XSC-105	44.23	0.077	51.70	0.043	96.04	2.04
Nodule 2-XSC-106	44.40	0.090	51.83	0.037	96.36	2.03
Nodule 2-XSC-107	44.16	0.103	51.87	0.038	96.18	2.05
Nodule 2-XSC-108	44.12	0.116	52.16	0.032	96.43	2.06
Nodule 2-XSC-109	44.21	0.054	51.65	0.045	95.95	2.04
Nodule 2-XSC-110	43.77	0.062	51.11	0.043	94.98	2.03
Nodule 2-XSC-111	44.11	0.085	51.85	0.036	96.08	2.05
Nodule 2-XSC-112	44.11	0.081	51.70	0.038	95.92	2.04
Nodule 2-XSC-113	44.48	0.111	52.16	0.040	96.79	2.04
Nodule 2-XSC-114	43.67	0.092	51.52	0.020	95.29	2.06
Nodule 2-XSC-115	43.52	0.047	51.13	0.037	94.74	2.05
Nodule 2-XSC-116	43.45	0.064	51.05	0.059	94.63	2.05
Nodule 3-XS-1	43.81	0.020	51.04	0.173	95.04	2.03
Nodule 3-XS-2	44.61	0.064	52.14	0.064	96.88	2.04
Nodule 3-XS-3	44.59	0.066	51.74	0.039	96.44	2.02
Nodule 3-XS-4	44.71	0.070	51.96	0.201	96.94	2.02
Nodule 3-XS-5	44.53	0.077	52.07	0.037	96.72	2.04
Nodule 3-XS-6	44.64	0.074	51.90	0.050	96.67	2.03
Nodule 3-XS-7	44.56	0.084	52.15	0.042	96.84	2.04
Nodule 3-XS-8	44.56	0.040	51.65	0.049	96.30	2.02
Nodule 3-XS-9	44.71	0.062	52.11	0.037	96.93	2.03
Nodule 3-XS-10	44.81	0.073	52.21	0.173	97.27	2.03
Nodule 3-XS-11	44.80	0.091	52.21	0.038	97.14	2.03
Nodule 3-XS-12	44.49	0.063	51.91	0.043	96.51	2.03
Nodule 3-XS-13	45.02	0.082	52.42	0.028	97.55	2.03
Nodule 3-XS-14	43.72	0.043	51.06	0.043	94.86	2.03
Nodule 3-XS-15	43.69	0.050	51.05	0.130	94.91	2.04
Nodule 3-XS-16	44.46	0.061	51.82	0.047	96.39	2.03
Nodule 3-XS-17	44.32	0.052	51.75	0.048	96.17	2.03
Nodule 3-XS-18	43.13	0.056	50.47	0.089	93.74	2.04
Nodule 3-XS-19	44.18	0.026	51.75	0.035	96.00	2.04
Nodule 3-XS-20	43.71	0.050	51.17	0.033	94.96	2.04
Nodule 3-XS-21	43.42	0.080	50.86	0.041	94.41	2.04
Nodule 3-XS-22	43.76	0.062	51.22	0.064	95.11	2.04
Nodule 3-XS-23	34.50	0.051	41.19	0.034	75.77	2.08
Nodule 3-XS-24	43.89	0.057	51.38	0.041	95.37	2.04
Nodule 3-XS-25	44.39	0.075	51.78	0.037	96.28	2.03

Sample	Fe (%)	Ni (%)	S (%)	Cu (%)	Total (%)	S/Fe
Nodule 3-XS-26	43.82	0.062	51.26	0.050	95.20	2.04
Nodule 3-XS-27	44.30	0.065	51.92	0.039	96.32	2.04
Nodule 3-XS-28	44.81	0.034	52.16	0.023	97.03	2.03
Nodule 3-XS-29	44.13	0.047	51.61	0.051	95.84	2.04
Nodule 3-XS-30	44.42	0.047	51.78	0.044	96.29	2.03
Nodule 3-XS-31	44.32	0.063	51.85	0.045	96.27	2.04
Nodule 3-XS-32	44.05	0.072	51.73	0.039	95.89	2.05
Nodule 3-XS-33	44.45	0.059	51.95	0.048	96.51	2.04
Nodule 3-XS-34	39.84	0.068	46.07	0.053	86.04	2.01
Nodule 3-XS-35	44.10	0.028	51.77	0.035	95.93	2.05
Nodule 3-XS-36	43.34	0.033	50.99	0.042	94.41	2.05
Nodule 3-XS-37	44.48	0.053	51.68	0.050	96.26	2.02
Nodule 3-XS-38	44.69	0.017	52.04	0.019	96.77	2.03
Nodule 3-XS-39	44.91	0.081	52.14	0.032	97.16	2.02
Nodule 3-XS-40	44.46	0.054	52.03	0.040	96.58	2.04
Nodule 3-XS-41	43.52	0.038	50.34	0.030	93.93	2.02
Nodule 3-XS-42	44.41	0.060	51.76	0.048	96.28	2.03
Nodule 3-XS-43	40.29	0.076	46.77	0.039	87.18	2.02
Nodule 3-XS-44	44.90	0.006	52.34	0.016	97.26	2.03
Nodule 3-XS-45	44.87	0.018	52.33	0.016	97.23	2.03
Nodule 3-XS-46	31.45	0.050	37.45	0.068	69.01	2.07
Nodule 3-XS-47	44.41	0.034	51.59	0.033	96.07	2.02
Nodule 3-XS-48	44.65	0.057	51.98	0.040	96.73	2.03
Nodule 3-XS-49	44.27	0.050	51.47	0.045	95.84	2.03
Nodule 3-XS-50	43.17	0.045	50.32	0.042	93.57	2.03
Nodule 3-XS-51	43.98	0.053	51.52	0.034	95.59	2.04
Nodule 3-XS-52	43.91	0.039	51.75	0.025	95.72	2.05
Nodule 3-XS-53	44.31	0.075	51.73	0.037	96.15	2.03
Nodule 3-XS-54	44.49	0.056	51.85	0.044	96.44	2.03
Nodule 3-XS-55	44.36	0.040	51.94	0.041	96.38	2.04
Nodule 3-XS-56	42.32	0.057	49.34	0.039	91.75	2.03
Nodule 3-XS-57	43.04	0.060	50.21	0.037	93.35	2.03
Nodule 3-XS-58	43.23	0.038	50.40	0.032	93.70	2.03
Nodule 3-XS-59	44.41	0.038	51.77	0.038	96.26	2.03
Nodule 3-XS-60	43.82	0.073	51.01	0.035	94.93	2.03
Nodule 3-XS-61	44.61	0.069	52.12	0.042	96.84	2.04
Nodule 3-XS-62	44.85	0.015	53.07	0.020	97.95	2.06
Nodule 3-XS-63	44.65	0.061	52.15	0.038	96.90	2.03
Nodule 3-XS-64	44.16	0.050	51.94	0.044	96.20	2.05
Nodule 3-XS-65	43.42	0.041	50.71	0.025	94.19	2.03
Nodule 3-XS-66	44.71	0.082	52.22	0.037	97.05	2.03

Sample	Fe (%)	Ni (%)	S (%)	Cu (%)	Total (%)	S/Fe
Nodule 3-XS-67	44.56	0.020	51.76	0.031	96.37	2.02
Nodule 3-XS-68	44.45	0.066	52.02	0.038	96.57	2.04
Nodule 3-XS-69	44.43	0.064	52.04	0.046	96.58	2.04
Nodule 3-XS-70	44.65	0.071	52.08	0.041	96.84	2.03
Nodule 3-XS-71	43.89	0.070	51.41	0.049	95.42	2.04
Nodule 3-XS-72	44.74	0.061	52.01	0.041	96.84	2.03
Nodule 3-XS-73	44.52	0.042	51.84	0.039	96.44	2.03
Nodule 3-XS-74	44.18	0.057	51.38	0.054	95.68	2.03
Nodule 3-XS-75	44.20	0.043	50.90	0.049	95.19	2.01
Nodule 3-XS-76	43.73	0.059	51.31	0.035	95.13	2.04
Nodule 3-XS-77	44.36	0.069	51.59	0.042	96.06	2.03
Nodule 3-XS-78	44.61	0.065	52.00	0.046	96.72	2.03
Nodule 3-XS-79	44.67	0.080	52.07	0.043	96.87	2.03
Nodule 3-XS-80	44.83	0.094	51.88	0.043	96.84	2.02
Nodule 3-XS-81	44.71	0.080	52.05	0.049	96.89	2.03
Nodule 3-XS-82	43.74	0.074	51.32	0.046	95.18	2.04
Nodule 3-XS-83	44.03	0.045	51.56	0.046	95.69	2.04
Nodule 3-XS-84	43.92	0.038	51.67	0.028	95.66	2.05
Nodule 3-XS-85	43.70	0.047	51.30	0.068	95.12	2.05
Nodule 3-XS-86	44.14	0.059	51.98	0.041	96.21	2.05
Nodule 3-XS-87	44.43	0.085	52.07	0.048	96.63	2.04
Nodule 3-XS-88	44.01	0.069	51.45	0.038	95.57	2.04
Nodule 3-XS-89	42.61	0.072	50.33	0.046	93.06	2.06
Nodule 3-XS-90	44.11	0.072	51.54	0.050	95.77	2.04
Nodule 3-XS-91	44.17	0.070	51.37	0.102	95.71	2.03
Nodule 3-XS-92	41.42	0.105	47.88	0.142	89.54	2.01
Nodule 3-XS-93	38.21	0.097	44.42	0.049	82.77	2.03
Nodule 3-XS-94	43.92	0.081	51.16	0.030	95.19	2.03
Nodule 3-XS-95	43.65	0.076	50.68	0.429	94.84	2.02
Nodule 3-XS-96	43.80	0.078	51.05	0.059	95.00	2.03
Nodule 3-XS-97	44.39	0.072	51.93	0.033	96.43	2.04
Nodule 3-XS-98	44.68	0.050	52.07	0.036	96.83	2.03
Nodule 3-XS-99	44.77	0.067	51.99	0.037	96.87	2.02
Nodule 3-XS-100	43.98	0.049	50.77	0.042	94.84	2.01
Nodule 3-XS-101	40.25	0.036	46.78	0.043	87.11	2.02
Nodule 3-XS-102	44.79	0.053	52.42	0.034	97.30	2.04
Nodule 3-XS-103	44.31	0.038	51.73	0.027	96.10	2.03
Nodule 3-XS-104	45.00	0.081	52.48	0.025	97.59	2.03
Nodule 3-XS-105	42.68	0.093	49.24	0.028	92.04	2.01
Nodule 3-XS-106	44.35	0.074	51.75	0.037	96.21	2.03
Nodule 3-XS-107	0.53	BDL	0.28	BDL	0.81	0.92

Sample	Fe (%)	Ni (%)	S (%)	Cu (%)	Total (%)	S/Fe
Nodule 3-XS-108	44.63	0.086	52.84	0.047	97.61	2.06
Nodule 3-XS-109	44.48	0.038	51.74	0.047	96.31	2.03
Nodule 3-XS-110	44.72	0.097	52.18	0.031	97.03	2.03
Nodule 3-XS-111	43.83	0.070	51.45	0.108	95.45	2.04
Nodule 3-XS-112	42.79	0.060	50.42	0.038	93.31	2.05
Nodule 3-XS-113	44.16	0.086	51.44	0.045	95.72	2.03
Nodule 3-XS-114	44.39	0.066	51.87	0.048	96.37	2.04
Nodule 3-XS-115	44.24	0.116	51.57	0.031	95.96	2.03
Nodule 3-XS-116	44.17	0.068	51.70	0.050	95.99	2.04
Nodule 3-XS-117	44.81	0.108	52.50	0.036	97.45	2.04
Nodule 3-XS-118	43.97	0.072	51.49	0.047	95.58	2.04
Nodule 3-XS-119	44.32	0.078	51.30	0.065	95.77	2.02
Nodule 3-XS-120	28.70	0.110	33.16	0.042	62.02	2.01
Nodule 3-XS-121	44.54	0.092	51.84	0.039	96.51	2.03
Nodule 3-XS-122	44.40	0.059	51.72	0.050	96.22	2.03
Nodule 3-XS-123	44.30	0.067	51.86	0.049	96.27	2.04
Nodule 3-XS-124	44.82	0.164	52.45	0.029	97.47	2.04
Nodule 3-XS-125	44.58	0.103	51.04	0.053	95.78	1.99
Nodule 3-XS-126	30.52	0.077	31.58	0.061	62.24	1.80
Nodule 3-XS-127	44.62	0.113	52.20	0.045	96.98	2.04
Nodule 3-XS-128	44.89	0.120	52.60	0.030	97.64	2.04
Nodule 3-XS-129	44.23	0.127	51.58	0.040	95.98	2.03
Nodule 3-XS-130	41.27	0.083	48.95	0.016	90.31	2.07
Nodule 3-XS-131	44.61	0.097	51.91	0.038	96.66	2.03
Nodule 3-XS-132	44.22	0.082	51.52	0.052	95.88	2.03
Nodule 3-XS-133	44.65	0.114	51.77	0.075	96.61	2.02
Nodule 3-XS-134	44.53	0.102	51.86	0.081	96.56	2.03
Nodule 3-XS-135	44.57	0.088	51.64	0.064	96.36	2.02
Nodule 3-XS-136	44.18	0.057	51.67	0.042	95.95	2.04
Nodule 3-XS-137	44.74	0.103	52.32	0.038	97.20	2.04
Nodule 3-XS-138	44.87	0.093	52.47	0.039	97.48	2.04
Nodule 3-XS-139	45.08	0.049	52.56	0.018	97.71	2.03
Nodule 3-XS-140	44.77	0.084	52.05	0.038	96.94	2.03
Nodule 3-XS-141	44.88	0.100	52.38	0.036	97.40	2.03
Nodule 3-XS-142	45.00	0.101	52.56	0.036	97.70	2.03
Nodule 2-rim-1	45.40	0.102	53.01	BDL	98.52	2.03
Nodule 2-rim-2	44.18	0.078	51.25	0.032	95.54	2.02
Nodule 2-rim-3	45.58	0.012	52.81	0.012	98.41	2.02
Nodule 2-rim-4	44.36	0.070	51.70	0.034	96.17	2.03
Nodule 2-rim-5	45.03	0.021	52.70	BDL	97.75	2.04
Nodule 2-rim-6	44.15	0.080	51.49	0.038	95.75	2.03

Sample	Fe (%)	Ni (%)	S (%)	Cu (%)	Total (%)	S/Fe
Nodule 2-rim-7	44.29	0.078	51.48	0.040	95.90	2.02
Nodule 2-rim-8	45.21	0.054	52.47	BDL	97.73	2.02
Nodule 2-rim-9	44.79	0.041	52.81	BDL	97.65	2.05
Nodule 2-rim-10	44.25	0.089	51.63	0.046	96.02	2.03
Nodule 3-rim-1	45.55	0.150	52.97	BDL	98.67	2.03
Nodule 3-rim-2	45.80	0.054	53.20	0.029	99.08	2.02
Nodule 3-rim-3	44.85	0.090	52.20	0.012	97.15	2.03
Nodule 3-rim-4	45.19	0.036	52.27	0.016	97.51	2.01
Nodule 3-rim-5	45.28	0.060	52.23	0.018	97.59	2.01
Lamina pyrite-1	45.77	0.006	51.42	0.074	97.27	1.96
Lamina pyrite-2	45.27	0.101	52.86	BDL	98.23	2.03
Lamina pyrite-3	45.45	0.013	51.27	0.075	96.81	1.97
Lamina pyrite-4	45.58	0.010	53.08	0.028	98.70	2.03
Lamina pyrite-5	44.85	0.020	52.19	0.020	97.08	2.03
Lamina pyrite-6	45.28	0.208	52.98	BDL	98.46	2.04
Lamina pyrite-7	45.23	0.139	52.34	0.009	97.72	2.02
Lamina pyrite-8	44.61	0.287	52.29	BDL	97.18	2.04
Lamina pyrite-9	44.69	0.452	53.41	BDL	98.55	2.08
Lamina pyrite-10	44.17	0.178	51.84	BDL	96.19	2.04
Lamina pyrite-11	45.13	0.018	53.21	0.008	98.36	2.05
Lamina pyrite-12	44.45	0.396	52.52	BDL	97.36	2.06
Lamina pyrite-13	45.63	0.020	53.17	0.016	98.84	2.03
Lamina pyrite-14	45.51	0.236	52.98	BDL	98.72	2.03
Lamina pyrite-15	45.57	0.023	53.32	0.014	98.93	2.04
Lamina pyrite-16	45.63	BDL	53.23	0.013	98.88	2.03
Lamina pyrite-17	45.53	0.011	53.35	0.014	98.90	2.04
Lamina pyrite-19	44.31	0.344	52.66	BDL	97.31	2.07
Lamina pyrite-20	45.34	BDL	53.29	0.017	98.64	2.05
Lamina pyrite-21	45.00	0.263	53.03	BDL	98.29	2.05
Lamina pyrite-22	44.91	0.237	53.11	BDL	98.26	2.06
Lamina pyrite-23	45.04	0.297	53.23	BDL	98.57	2.06
C_U FeS2 std	46.12	BDL	53.53	BDL	99.66	2.02
C_U FeS2 std	46.06	BDL	53.63	BDL	99.69	2.03
C_U FeS2 std	46.04	BDL	53.60	BDL	99.65	2.03
C_U FeS2 std	46.14	BDL	53.58	BDL	99.72	2.02
C_U FeS2 std2	46.29	BDL	53.66	BDL	99.96	2.02
C_U FeS2 std2	46.41	BDL	53.68	BDL	100.10	2.01
C_U FeS2 std2	46.38	BDL	53.72	BDL	100.10	2.02
C_U FeS2 std2	46.19	BDL	53.67	BDL	99.86	2.02

*BDL denotes concentrations are below detection limit

Table 2 Multiple sulfur data of pyrite from shale in the Deer Lake Greenstone belt, Minnesota, USA

Sample	$\delta^{33}\text{S}$ (VCDT)	2σ (‰)	$\delta^{34}\text{S}$ (VCDT)	2σ (‰)	$\Delta^{33}\text{S}$	2σ (‰)
Nodule 1-XS-1	1.26	0.14	-2.42	0.13	2.50	0.19
Nodule 1-XS-2	0.88	0.13	-2.84	0.11	2.34	0.17
Nodule 1-XS-3	1.01	0.14	-2.71	0.11	2.41	0.18
Nodule 1-XS-4	0.80	0.15	-2.91	0.11	2.30	0.18
Nodule 1-XS-5	1.06	0.13	-2.39	0.12	2.29	0.17
Nodule 1-XS-6	0.77	0.15	-2.68	0.11	2.15	0.19
Nodule 1-XS-7	0.72	0.13	-2.57	0.12	2.04	0.18
Nodule 1-XS-8	1.47	0.13	-1.04	0.12	2.00	0.18
Nodule 1-XS-9	1.47	0.14	-0.49	0.15	1.72	0.21
Nodule 1-XS-10	1.79	0.13	0.44	0.13	1.56	0.18
Nodule 1-XS-11	1.49	0.13	0.61	0.12	1.17	0.18
Nodule 1-XS-12	0.79	0.17	-1.50	0.18	1.56	0.25
Nodule 1-XS-13	0.64	0.13	-1.49	0.12	1.41	0.17
Nodule 1-XS-14	1.20	0.14	1.04	0.15	0.66	0.20
Nodule 1-XS-15	1.62	0.15	0.31	0.15	1.46	0.21
Nodule 1-XS-16	1.77	0.14	1.61	0.13	0.94	0.19
Nodule 1-XS-17	2.93	0.15	1.95	0.15	1.93	0.21
Nodule 1-XS-18	1.64	0.13	1.83	0.15	0.70	0.20
Nodule 1-XS-19	2.05	0.14	1.80	0.13	1.12	0.19
Nodule 1-XS-20	1.61	0.14	-0.15	0.15	1.68	0.20
Nodule 1-XS-21	0.09	0.12	-1.76	0.15	1.00	0.19
Nodule 1-XS-22	1.42	0.12	0.19	0.15	1.33	0.19
Nodule 1-XS-23	1.66	0.14	0.27	0.13	1.52	0.19
Nodule 1-XS-24	1.25	0.14	-1.05	0.13	1.79	0.19
Nodule 1-XS-25	0.81	0.13	-2.57	0.13	2.14	0.18
Nodule 1-XS-26	1.06	0.14	-2.51	0.12	2.35	0.18
Nodule 1-XS-27	0.91	0.13	-2.89	0.12	2.39	0.18
Nodule 1-XS-28	1.67	0.14	-1.67	0.13	2.53	0.19
Nodule 1-XS-29	1.12	0.12	-2.66	0.13	2.49	0.17
Nodule 2-XS-1	0.97	0.16	-1.92	0.18	1.96	0.24
Nodule 2-XS-2	1.25	0.12	-1.95	0.13	2.26	0.18
Nodule 2-XS-3	1.03	0.16	-1.22	0.14	1.66	0.21
Nodule 2-XS-4	1.14	0.14	-1.44	0.14	1.88	0.19
Nodule 2-XS-5	1.74	0.14	-0.02	0.18	1.75	0.23
Nodule 2-XS-6	1.90	0.13	-0.01	0.16	1.91	0.21
Nodule 2-XS-7	2.09	0.15	0.46	0.16	1.84	0.21
Nodule 2-XS-8	1.52	0.19	-1.07	0.22	2.07	0.29

Sample	$\delta^{33}\text{S}$ (VCDT)	2 σ (‰)	$\delta^{34}\text{S}$ (VCDT)	2 σ (‰)	$\Delta^{33}\text{S}$	2 σ (‰)
Nodule 2-XS-9	1.01	0.15	-1.24	0.20	1.65	0.25
Nodule 2-XS-10	1.78	0.16	0.11	0.18	1.73	0.24
Nodule 2-XS-11	1.13	0.14	-1.36	0.24	1.83	0.28
Nodule 2-XS-12	1.39	0.15	-1.10	0.18	1.95	0.24
Nodule 2-XS-13	2.01	0.13	0.18	0.15	1.91	0.20
Nodule 2-XS-14	1.98	0.12	0.66	0.15	1.64	0.20
Nodule 2-XS-15	1.31	0.14	0.38	0.16	1.11	0.21
Nodule 2-XS-16	1.88	0.16	1.04	0.17	1.35	0.23
Nodule 2-XS-17	0.87	0.17	-0.55	0.25	1.15	0.30
Nodule 2-XS-18	1.22	0.13	0.39	0.16	1.02	0.21
Nodule 2-XS-19	1.92	0.14	0.70	0.15	1.55	0.20
Nodule 2-XS-20	2.07	0.13	-0.07	0.15	2.10	0.20
Nodule 2-XS-21	1.76	0.13	0.76	0.15	1.36	0.20
Nodule 2-XS-22	1.73	0.15	0.54	0.18	1.45	0.24
Nodule 2-XS-23	0.74	0.16	-0.06	0.23	0.77	0.28
Nodule 2-XS-24	1.98	0.12	0.62	0.15	1.66	0.20
Nodule 2-XS-25	1.31	0.16	-1.12	0.18	1.88	0.24
Nodule 2-XS-26	0.55	0.14	-1.48	0.16	1.32	0.21
Nodule 3-XS-1	0.79	0.12	-2.39	0.14	2.02	0.18
Nodule 3-XS-2	0.87	0.12	-2.25	0.13	2.03	0.18
Nodule 3-XS-3	0.74	0.16	-2.06	0.14	1.80	0.21
Nodule 3-XS-4	0.63	0.15	-2.69	0.15	2.02	0.21
Nodule 3-XS-5	0.54	0.12	-1.73	0.14	1.43	0.18
Nodule 3-XS-6	0.76	0.13	-0.78	0.16	1.16	0.20
Nodule 3-XS-7	1.80	0.14	-0.26	0.17	1.93	0.22
Nodule 3-XS-8	2.22	0.15	0.42	0.15	2.00	0.21
Nodule 3-XS-9	1.41	0.14	-0.93	0.16	1.89	0.22
Nodule 3-XS-10	1.18	0.15	0.06	0.22	1.14	0.27
Nodule 3-XS-11	1.11	0.15	0.55	0.13	0.83	0.20
Nodule 3-XS-12	1.59	0.13	0.44	0.14	1.36	0.19
Nodule 3-XS-13	0.75	0.13	0.31	0.13	0.60	0.19
Nodule 3-XS-14	1.19	0.14	0.50	0.16	0.94	0.22
Nodule 3-XS-15	1.02	0.15	0.49	0.15	0.77	0.21
Nodule 3-XS-16	1.71	0.14	-1.15	0.15	2.30	0.20
Nodule 3-XS-17	1.10	0.14	-1.04	0.15	1.64	0.20
Nodule 3-XS-18	1.44	0.14	-1.13	0.14	2.02	0.19
Nodule 3-XS-19	0.96	0.13	-2.25	0.14	2.12	0.19
Nodule 3-XS-20	1.21	0.13	-1.52	0.13	1.99	0.18

Sample	$\delta^{33}\text{S}$ (VCDT)	2σ (‰)	$\delta^{34}\text{S}$ (VCDT)	2σ (‰)	$\Delta^{33}\text{S}$	2σ (‰)
Nodule 2-RIM-1	6.34	0.14	3.99	0.13	4.27	0.19
Nodule 2-RIM-2	1.64	0.13	0.42	0.17	1.42	0.21
Nodule 2-RIM-3	8.82	0.13	7.71	0.13	4.82	0.18
Nodule 2-RIM-4	1.75	0.14	0.62	0.18	1.43	0.23
Nodule 2-RIM-5	7.74	0.16	6.41	0.13	4.42	0.21
Nodule 2-RIM-6	0.61	0.14	-1.67	0.14	1.47	0.20
Nodule 2-RIM-7	0.65	0.14	-2.01	0.15	1.69	0.20
Nodule 2-RIM-8	7.47	0.14	5.90	0.13	4.42	0.18
Nodule 2-RIM-9	5.75	0.14	3.41	0.12	3.98	0.18
Nodule 2-RIM-10	0.22	0.17	-2.56	0.24	1.53	0.29
Nodule 3-RIM-1	7.69	0.12	6.15	0.12	4.51	0.17
Nodule 3-RIM-2	7.16	0.13	5.35	0.10	4.38	0.17
Nodule 3-RIM-3	5.71	0.14	3.19	0.12	4.05	0.18
Nodule 3-RIM-5	6.22	0.15	3.86	0.12	4.22	0.19
Lamina pyrite-1	2.11	0.13	-1.05	0.11	2.65	0.16
Lamina pyrite-2	5.51	0.13	3.43	0.12	3.73	0.18
Lamina pyrite-3	1.58	0.12	-1.88	0.11	2.54	0.17
Lamina pyrite-4	1.70	0.13	-1.89	0.12	2.67	0.18
Lamina pyrite-5	1.55	0.14	-2.29	0.14	2.73	0.20
Lamina pyrite-6	4.89	0.16	2.46	0.16	3.62	0.22
Lamina pyrite-7	5.65	0.13	3.66	0.12	3.75	0.17
Lamina pyrite-8	6.63	0.13	5.09	0.13	3.99	0.18
Lamina pyrite-9	5.51	0.13	3.42	0.12	3.73	0.18
Lamina pyrite-10	5.54	0.14	3.40	0.12	3.78	0.18
Lamina pyrite-11	1.66	0.13	-2.13	0.16	2.76	0.20
Lamina pyrite-12	5.56	0.15	3.54	0.12	3.72	0.19
Lamina pyrite-13	1.61	0.13	-1.97	0.12	2.62	0.17
Lamina pyrite-14	5.67	0.13	3.55	0.12	3.83	0.18
Lamina pyrite-15	2.09	0.14	-1.49	0.15	2.85	0.20
Lamina pyrite-16	1.93	0.14	-1.95	0.12	2.93	0.18
Lamina pyrite-17	1.75	0.15	-2.28	0.12	2.93	0.19
Lamina pyrite-19	6.26	0.15	4.48	0.14	3.94	0.20
Lamina pyrite-20	1.34	0.13	-2.71	0.12	2.74	0.17
Lamina pyrite-21	6.01	0.12	4.20	0.12	3.84	0.17
Lamina pyrite-22	5.91	0.12	3.94	0.11	3.87	0.17
Lamina pyrite-23	6.08	0.15	4.19	0.12	3.91	0.19